Translational Imaging of Pulmonary Gas-Exchange Using Hyperpolarized ^{129}Xe Magnetic Resonance Imaging

by

Suryanarayanan Sivaram Kaushik

Department of Biomedical Engineering
Duke University

Date:________________________
Approved:

____
Bastiaan Driehuys, Supervisor

____
G. Allan Johnson

____
Kathy Nightingale

____
W. Michael Foster

____
H. Page McAdams

Dissertation submitted in partial fulfillment of
the requirements for the degree of Doctor
of Philosophy in the Department of
Biomedical Engineering in the Graduate School
of Duke University

2014

ABSTRACT

Translational Imaging of Pulmonary Gas-Exchange Using Hyperpolarized ^{129}Xe Magnetic Resonance Imaging

by

Suryanarayanan Sivaram Kaushik

Department of Biomedical Engineering
Duke University

Date:_______________________
Approved:

____
Bastiaan Driehuys, Supervisor

____
G. Allan Johnson

____
Kathy Nightingale

____
W. Michael Foster

____
H. Page McAdams

An abstract of a dissertation submitted in partial
fulfillment of the requirements for the degree
of Doctor of Philosophy in the Department of
Biomedical Engineering in the Graduate School of
Duke University

2014

Abstract

Pulmonary diseases are becoming a large and unsustainable economic burden in the US. For example, chronic obstructive pulmonary disease (COPD) is now the third leading cause of death in the US, and the hospitalization costs for asthma are on the order of $29 Billion. Despite these staggering numbers, the diagnosis and treatment of pulmonary diseases still rely on pulmonary function tests, which are notoriously insensitive to subtle changes in lung function and pathology of the small airways. This insensitivity has further stymied the development of new therapies to treat pulmonary diseases. To this end, it is being increasingly recognized that overcoming these barriers requires creating imaging biomarkers of pulmonary function. Specifically, imaging the lung using hyperpolarized (HP) gas MRI provides a non-invasive means to assess pulmonary function 3-dimensionally in a single breath.

The work presented in this thesis began just as the field of HP gas MRI was making the transition from the supply-limited ^{3}He gas, which produced exquisite images, to ^{129}Xe, which offered infinite supply, but posed significant imaging challenges. However, once we had demonstrated that ^{129}Xe ventilation MRI could be optimized to obtain the kind of image quality that was historically seen with ^{3}He, we began evaluating additional contrast mechanisms that are unique to ^{129}Xe MRI. The aim was to extend the imaging

capabilities beyond simple ventilation to provide a more comprehensive picture of pulmonary function. This thesis is thus centered on extending hyperpolarized (HP) ^{129}Xe MRI to probe the most fundamental function of the lung – gas-exchange.

Efficient gas-exchange requires the diffusive transfer of gases across the alveolar-capillary barrier as dictated by Fick's first law. To this end, the first factor controlling gas-exchange is the alveolar surface area, which can be assessed by exploiting the diffusivity of ^{129}Xe *within* the airspaces. In the case of emphysema, which often accompanies COPD, the associated destruction of lung tissue reduces the alveolar surface area for gas exchange. Subsequently, this increases the distance that xenon can diffuse *within* the alveolus. Thus, by using diffusion-weighted imaging of the gas-phase of ^{129}Xe, one can extract its 'apparent diffusion coefficient' (ADC) that is sensitive to the alveolar surface area. Developing this contrast mechanism and applying it in COPD patients is the focus of **chapter 3**.

However, the bulk of my thesis is devoted to exploiting perhaps the most interesting properties of xenon MRI – its solubility and tissue-specific frequency shifts. When inhaled, the bulk of HP ^{129}Xe stays in the alveolar spaces, but its moderate solubility in the pulmonary tissues causes a small fraction of this xenon to diffuse into the pulmonary barrier tissues and plasma, and further into the red blood cells (RBC). When xenon enters either of these compartments, it experiences a unique shift in its resonance frequency that allows it to be separately detected from xenon remaining in the gas-phase. These additional unique resonances are collectively called the dissolved-phase of xenon and are comprised of a barrier resonance, shifted by 198 ppm, and an RBC resonance shifted by 217 ppm from the gas-phase. Since xenon follows the same pathway to the RBCs as oxygen does, imaging ^{129}Xe in the dissolved phase offers a potentially ideal non-invasive probe to study pulmonary gas exchange.

As this thesis work began, direct, single-breath imaging of the dissolved-phase of ^{129}Xe was just starting to be attempted. However, technical challenges of imaging this tiny signal had limited dissolved-phase imaging from being established on a reliable and reproducible footing. Additionally, as the gas-phase provides the source magnetization for the dissolved-phase ^{129}Xe signal, it was realized that making dissolved phase MRI truly quantitative would require acquiring both the gas and dissolved-phase distributions in a single breath. **Chapters 4** and **5** focus on these topics, and detail the changes to 3D radial acquisition strategies needed to acquire both the gas and dissolved-phase images in a single breath.

Once 3D images of ^{129}Xe gas transfer were realized on a reliable footing, the next challenge was to obtain independent measurements of the ^{129}Xe transfer to the barrier and RBCs. We approached this problem by first using non-spatially localized ^{129}Xe spectroscopy to characterize gas exchange on a global basis. The principle behind this approach lay in the fact that the application of an RF pulse to ^{129}Xe in the RBCs depletes its magnetization. However, as the resonances of xenon are in dynamic exchange, this depleted magnetization is replenished by the xenon with fresh magnetization diffusing in from the airspaces. While this replenishment is rapid in a healthy lung, where the barrier thickness is < 1μm, this recovery can be significantly delayed if the thickness increases by even a few microns. This hypothesis was tested by acquiring dissolved-phase ^{129}Xe spectra in healthy volunteers and subjects with idiopathic pulmonary fibrosis (IPF). The degree of RBC signal recovery was quantified using the ratio of the RBC and barrier resonances, which was found to be reduced by a factor of more than 3 in IPF. This work, which is discussed in **chapter 6**, demonstrated that ^{129}Xe gas-transfer spectroscopy can detect diffusion-limitation even on a whole-lung basis.

By combining the insights from 3D dissolved-phase imaging and the spectroscopic separation of ^{129}Xe in RBC and barrier, this work culminated in demonstrating a method to acquire 3D images of all three ^{129}Xe resonances in a single breath. This is the focus of **chapter 7** of this thesis, which details the implementation of a 1-point Dixon acquisition strategy to create independent images of the ^{129}Xe in barrier and RBCs. The efficacy of these ^{129}Xe-RBC images was evaluated in patients with IPF, and compared to healthy volunteers these images exhibited significantly greater gas-transfer defects.

In short, this thesis work has taken the first technical steps to demonstrate that HP ^{129}Xe MRI can provide a non-invasive, ionizing radiation free method to probe ventilation, microstructural changes and most importantly, gas-exchange. The imaging tools provided by HP ^{129}Xe MRI see applications in studying a wide range of pulmonary diseases from COPD to pulmonary vascular diseases. Broadly, ^{129}Xe MRI has the potential to serve as a sensitive and comprehensive tool in therapeutic clinical trials to evaluate longitudinal changes in regional lung function, and further help generate viable therapies that may reduce the bane of pulmonary diseases.

Dedicated to my Parents,

S. Suryanarayanan

Lakshmi Suryanarayanan

Contents

List of Tables

List of Figures

Acknowledgements

This thesis would not have been possible without the support, guidance, and inspired vision of my advisor Bastiaan Driehuys, and to him, I owe a debt of gratitude. I would also like to thank Zackary Cleveland, who in addition to my advisor, has had a big influence in my years in graduate school, and continues to be a good mentor and friend. For inspiring me daily, I would like to thank team hyperpolarized – Matthew Freeman, Scott Robertson, Rohan Virgincar, and Mu He. I have a special note of thanks for Gary Cofer, for helping me with EPIC, RF coils, and improving my taste in beer. I would also like to thank everyone else at the Center for In Vivo Microscopy for the wonderful resources and people that make coming into work an absolute delight. I thank the BME department, and especially my committee members – G. Allan Johnson, Kathy Nightingale, Michael Foster, and Page McAdams. Lastly, I would like to thank my parents, who have and always will be my pillars of strength.

1. Significance and Motivation

My thesis work is centered on the development of inhaled hyperpolarized ^{129}Xe MRI as a method to detect, characterize, and monitor pulmonary disease and its response to therapy. In this chapter I will lay out the case for why the study and treatment of pulmonary disease is in urgent need of imaging biomarkers, the current landscape of imaging biomarkers in pulmonary disease, and why hyperpolarized ^{129}Xe MRI has specific advantages over these other approaches. Although we expect hyperpolarized ^{129}Xe MRI to have an impact across a broad range of pulmonary conditions, my specific research is focused on applications to chronic obstructive pulmonary disease (COPD) and interstitial lung diseases (ILD). Hence, these conditions and their specific imaging needs will be highlighted in this introduction.

Lung diseases are currently a global healthcare concern and in the United States, remain the 4th leading cause of death (1). While most other diseases (cancer, stroke, cardiovascular disease) have experienced decreasing rates of death, that of lung disease has continued unabated (2). For example, asthma affects 300 million people worldwide, and its prevalence is expected to increase by 50 million per decade (3). Chronic obstructive pulmonary disease affects roughly 14 million people in the United States alone, with a staggering cost of hospitalization exceeding $29 billion (2). As discussed in (4), the current rise of pulmonary disease is economically unsustainable, and COPD is predicted to be the 3rd leading cause of death by 2020 (5).

A key bottleneck in the diagnosis and treatment of pulmonary disease is the absence of sensitive and specific biomarkers to measure disease burden and progression. The current 'gold standard' in the diagnosis and management of COPD is the pulmonary function test (PFT). This test obtains multiple metrics describing pulmonary function through breathing maneuvers performed using a spirometer. The metrics of pulmonary function provided by the PFTs have been used to assess response to therapy and have also been used to phenotype COPD (4). However, as subjects with COPD present varied symptoms and have a combination of multiple disease processes, quantifying these changes with a global PFT metric has been shown to be inadequate (6). Furthermore, current clinical standards require that PFT metrics such as the forced expiratory volume in 1 second (FEV_1) change by at least 20% to be considered a significant change in disease status (6). Changes in PFT metrics have also shown a poor correlation to patient survival (7). As a result, although there have been multiple clinical trials attempting to understand and better treat pulmonary diseases using changes in PFT metrics as an endpoint, this insensitivity has resulted in limited progress made in creating viable treatment options (6). Hence, the heterogeneous mechanisms of pulmonary diseases and function create an urgent need to look beyond PFTs for biomarkers that allow quantitative evaluation of lung function regionally.

Early detection of lung diseases will be aided by imaging modalities that are sensitive to subtle changes in lung structure and function. Regional information obtained through imaging could help us understand the functioning of the healthy lung and also analyze the extent and severity of different disease phenotypes. To this end, a large contribution to the radiologic evaluation of the lung has been made by thin-section computed tomography (CT) (8-10). The improvement in detector technology afforded CT its exquisite resolution and due to its inherently quantitative nature, CT has provided a framework to classify different phenotypes of COPD (11). Despite its current ubiquity, the application of CT in the longitudinal evaluation of subjects with lung diseases is limited by the associated radiation dose (12). Apart from structural changes, the key in understanding changes with disease is in imaging changes in pulmonary function. In spite of its capabilities in imaging perfusion (13), with its associated radiation dose, CT is further limited in its capacity primarily as a structural imaging modality.

While the primary function of the lung is to exchange gases with the alveolar capillary blood stream, information of this gas-exchange has been inferred primarily through ventilation and perfusion imaging. These processes have been studied using dual energy CT using xenon and iodine as ventilation and perfusion contrast agents (14), and radionuclide imaging modalities such as positron emission tomography (PET) (15) and single photon emission computed tomography (SPECT) (16). These modalities have shown that even in the healthy lung, ventilation and perfusion is quite heterogeneous. In spite of this heterogeneity, in order to maintain adequate oxygen saturation, perfusion is higher in regions that are well ventilated, resulting in a good matching of the two processes (15). Thus, in a healthy lung, the ratio of ventilation and perfusion, which is used as a metric of gas-exchange, is unity. However with the onset of diseases, the delicate interplay between the structure and function of the lung is disrupted. This results in a poor transfer of oxygen into the bloodstream and consequently, causes a reduction in the ventilation-perfusion ratio (17). However, imaging lung function using these modalities is limited by the associated radiation dose contributed by the radiotracer, and this further limits the use of radionuclide imaging modalities in the longitudinal assessment of subjects with disease.

As an alternative to radiation based imaging approaches, magnetic resonance imaging (MRI) offers an ionizing radiation free, non-invasive modality to study lung structure and function. Although imaging the lung using MRI remains challenging because of its low proton density and susceptibility losses caused by air-tissue interfaces, recent technological advancements have made MRI of the lung feasible. The advent of multi-channel receiver coils, and ultra-short echo time (UTE) sequences, have helped overcome the low magnetization and rapid T_2* of the parenchyma to image the pulmonary microstructure (18). While these radiation-free images had a lower resolution than the CT, the images showed similar information. As for ventilation,^{1}H images acquired while the subject inhales 100% O_2 can be used to indirectly map specific ventilation in the lung (19). While a novel technique, it has a complicated experimental procedure, and is plagued with images that have a rather poor contrast-noise-ratio and more importantly, to minimize blurring induced by heart motion, is limited to a single slice in the right lung. Pulmonary perfusion imaging however, is on a more stable footing, and has been well developed with and without the use of external contrast agents (20,21). Among these techniques, dynamic contrast enhanced (DCE) studies use an external bolus of a Gadolinium based agent to study the time varying enhancement of the pulmonary vasculature (20) and extract quantitative metrics of perfusion. As an alternative, arterial spin labeling (ASL) MRI has enabled imaging lung perfusion without the need for an exogenous contrast agent (22). While capillary perfusion is of prime importance to indirectly study gas-exchange in the lung, ASL and DCE MRI are also sensitive to perfusion in the larger vasculature (23). Furthermore, to minimize blurring caused by the motion of the heart, ASL perfusion images are also limited to a single slice in the right lung (19,21).

To overcome the shortcomings of traditional ^{1}H based MRI, hyperpolarized (HP) noble gases have emerged over the last decade, as an external gaseous contrast agent for ventilation imaging (24,25). Over the formative years, ventilation based imaging studies have used HP ^{3}He as its high polarization and high diffusivity lent itself to multiple methods of imaging the lung. While typical helium imaging was completed in a single breath hold to yield static ventilation images, high helium polarizations afforded the ability to map ventilation dynamically (26). These dynamic methods have also been used to study fractional ventilation (27). While helium cannot be used to study regional perfusion, it has been extensively used to map regional oxygen partial pressure (28). This method is an indirect and cumbersome approach to study the matching of regional ventilation and perfusion. Beyond ventilation imaging, HP ^{3}He can also measure the regional apparent diffusion coefficient (ADC) (29,30). With the use of ^{3}He ADC in the small animal models of emphysema, considerable progress has been made in understanding the disease progression, and this led to studies that have used HP ^{3}He to non-invasively phenotype the alveolar degradation seen in COPD based diseases (31). ^{3}He ADC has also been shown to be extremely reproducible and has been used to study the impact of second-hand smoke on healthy volunteers (32), gradients caused by subject posture (33), and age-related changes in alveolar size (34). While helium MRI had a promising future, the reallocation of ^{3}He has led to a dwindling of the helium stockpile from about 235,000 liters in 2001 to 50,000 liters in 2010. Consequently, the price of helium has risen from

100 – 200$/liter to as high as 2000$/liter, making pulmonary research with this gas unaffordable (35).

As a result of the helium shortage, the hyperpolarized community looked toward ^{129}Xe to serve as a viable replacement. Compared to helium, working with xenon is significantly harder as a) *xenon has a lower gyromagnetic ratio (11.77 MHz/T vs. 32.4 MHz/T)* and b) *the polarization achievable with xenon is lower (10 – 15% vs. 40%)*. Both of these factors result in almost 27-fold lower xenon signal intensity. On the plus side, ^{129}Xe is naturally available in the atmosphere, and as a result, significantly cheaper (~30$/liter, natural abundance). In spite of these challenges, we have shown the utility of ^{129}Xe in static-ventilation studies by quantifying the ventilation defects seen in healthy volunteers and subjects with COPD (36). Apart from pure ventilation studies, we have also implemented ^{129}Xe diffusion-weighted imaging (37). This is a significant achievement as the lower gyromagnetic ratio required longer diffusion weighting gradients to achieve adequate diffusion weighting, which increased the minimum achievable echo time. This resulted in greater T_2* weighting, which lowered the signal intensity further. In spite of these limiting factors, high quality apparent diffusion coefficient maps were generated, which were sensitive enough to detect changes in the alveolar microstructure in healthy volunteers, age-matched controls and subjects with COPD. The results of this study will be discussed in detail in **chapter 3**.

As COPD and asthma largely affect the airways and parenchyma, they can be well assessed using ventilation and ADC imaging. On the other hand, interstitial lung diseases (ILD) are diseases that impact the alveolar interstitium and primarily affect pulmonary gas-exchange. These diseases are particularly deadly, and are in dire need of therapeutic attention and sensitive biomarkers. Among these, idiopathic pulmonary fibrosis (IPF), which is a common type of ILD, has a prevalence rate for men over the age of 75 years, of ~175 per 100,000 (38). In spite of the low prevalence, the problem however, is that existing treatment options for the disease are merely palliative and result in a mean survival from diagnosis of only about 4 years (39). The current gold standards in the diagnosis of IPF involve ionizing radiation as a part of a CT scan, or worse, an invasive open lung biopsy (40). Additionally, the current endpoints for therapeutic clinical trials use rather insensitive PFT metrics such as the Forced Vital Capacity (FVC), and the 6-min walk test, both of which have been shown to be only reasonable predictors of patient mortality (41). These insensitive endpoints require at least a 20% change in FVC, or a 10% change in DL_{CO} to warrant significant change in disease status. Furthermore, subjects with IPF have extensive interstitial inflammation and fibrosis that limits the diffusion of gases across the capillary blood-gas barrier. As this disease primarily impacts gas-exchange, traditional ventilation imaging showed qualitatively normal lungs, and hence had limited use in quantifying the extent of fibrosis. As a result, while there are multiple clinical trials underway to test potential therapies for IPF (42), what is truly lacking are sensitive tools to test the effectiveness of these therapies, and predict early changes in lung function. Interestingly, it is possible to get such gas-exchange biomarkers using properties that are unique to hyperpolarized ^{129}Xe.

In addition to its presence in the alveolar air spaces which yields ventilation and diffusion weighted images, the appeal in using ^{129}Xe truly stems from its moderate solubility in the pulmonary tissues, and the capillary blood stream (Ostwald solubility in blood at 37°C = 0.0939, and barrier tissue = 0.271 (43)). When in either of these compartments, ^{129}Xe experiences large distinct chemical shifts – barrier tissue/plasma (~3.5kHz, 198 ppm) and red blood cells (RBC, 3.83kHz, 217 ppm). These two additional resonances are together termed as the 'dissolved-phase' of ^{129}Xe and the characteristics of these resonances (width, frequency, amplitude) are sensitive to the structural and functional features of the lung. As the pathway taken by xenon to reach the RBCs is identical to that of oxygen, in addition to studying ventilation and microstructural changes, xenon can be used as an ideal surrogate for the study of the diffusive gas-exchange. A representative dissolved-phase spectrum is shown in **figure 1**.

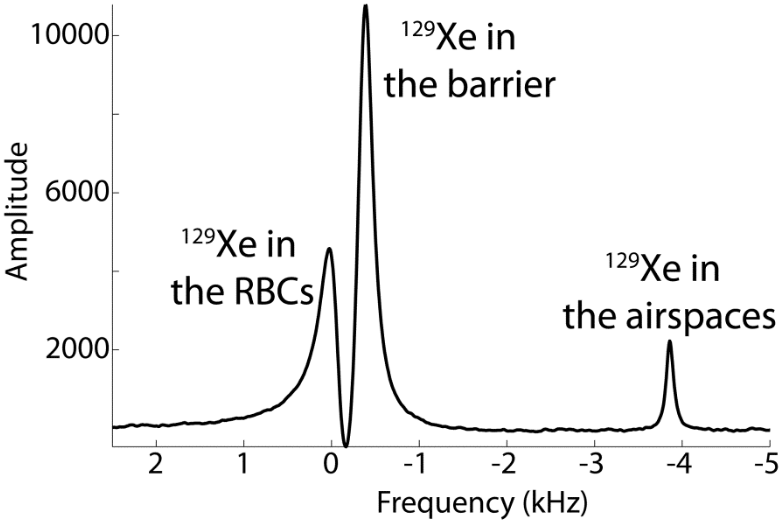

Figure 1: Spectrum showing the different resonances of xenon in the lung. ^{129}Xe in the barrier is separated from the gas-phase xenon by ~3.5 kHz (198 ppm), and the RBC resonance is further removed at 3.8 kHz (217 ppm).

My thesis is centered on exploiting this dissolved-phase to obtain global and regional information about gas-exchange in the lung. Given the low magnetization of the xenon in the dissolved-phase compartments (~2% of the gas-phase) and rapid relaxation rate (~2ms (44)), initial efforts to image this dissolved-phase distribution employed indirect approaches. As the xenon resonances are in dynamic exchange with one another, pulsing on the dissolved-phase would partially depolarize the gas-phase resonance. This phenomenon was used to indirectly map the dissolved-phase distribution. However, this xenon transfer contrast, or XTC, was extremely limited because of the restrictions imposed on the RF pulses, and the need for multiple images to correct for the T_1 decay of the gas-phase (45). Most importantly, this method lacked the ability to separate the contributions of xenon in the barrier and the RBCs. With improvements in polarization, and using rapid pulse sequences, our group and others have shown the ability to directly image the dissolved-phase (43,46).

Reliable imaging of this dissolved-phase poses a unique set of challenges. a) *The RF pulse needed to excite the dissolved-phase must be selective enough to avoid exciting the significantly larger gas-phase magnetization* b) *Given the rapid* T_2^* *of the dissolved-phase, this RF pulse also needs to be sufficiently short* c) *Quantifying the dissolved-phase signal distribution requires an image of the gas-phase 'source' distribution in the same breath* d) *The flip-angle used for the sequence must be large enough to obtain a sizeable dissolved signal, but small enough to reduce the time needed to replenish this signal. This can be complemented with a short repetition time (TR) such that we adequately sample k-space in a short 15 second breath hold.* While the first two factors may seem trivial, it required overcoming the non-linearity of the RF amplifier, which made the choice of RF pulse length or power non trivial. **Chapter 4** details the steps taken to overcome these challenges, and the development and clinical translation of a 3D radial pulse sequence used to acquire both the gas and the dissolved-phase images in a single breath. This pulse sequence was used quantify the impact of posture on the distribution of gas-exchange, which has been a long standing debate in the pulmonary community. These results are discussed in detail in **chapter 5**.

The dissolved-phase of ^{129}Xe is an extremely sensitive tool to study the structural changes noticed in IPF. In fact, the spectra acquired in an IPF subject showed a reduction in the RBC signal amplitude. This reduction is indicative of reduced gas-exchange, and as a result, extensive diffusion impairment. This gas-exchange impairment was first quantified using global gas-exchange spectroscopy, which is discussed in **chapter 6** and the rationale behind the method is also discussed in **chapter 2**. While this provided a global biomarker of gas-exchange, extending this to regional information would require creating separate images of ^{129}Xe in the RBCs and ^{129}Xe in the barrier tissue. However, as the dissolved-phase signal intensity is only 2% of the gas-phase, and has a very rapid T_2^* of ~2 ms (44), separating the components of the dissolved-phase would require unique acquisition strategies. Driehuys *et al*. (47), used a variant of the Dixon acquisition scheme in rats, to create 2D images of ^{129}Xe in the barrier and the RBC, which we extended to 3D (48). In translating this to the clinic, Qing *et al*. employed an alternate strategy, and implemented the Hierarchical IDEAL algorithm to create images of all three resonances of xenon in a single-breath (49). The downside of this method however, is that it requires two additional echoes to decompose the ^{129}Xe in barrier and the RBCs. While the short T_2^* was overcome using higher ^{129}Xe polarization (~40%), the requirement of additional echoes makes this method rather undesirable. Hence, the focus of **chapter 7** is in detailing the acquisition and processing methods needed for the clinical realization of the 1-

point Dixon approach to acquire 3D, co-registered images of all three resonances of ^{129}Xe in a single breath. This technique has enabled us to separately quantify the perfusion-dependent RBC ^{129}Xe image and interstitial tissue-dependent barrier ^{129}Xe image, and compare the changes in healthy subjects and patients with IPF. The ^{129}Xe-RBC image thus gives us a non-invasive method to study diffusive gas-exchange right at the alveolar capillary regions of the lung.

The focus of my research can be broken down into these ***specific aims***:

I) Demonstrate feasibility of diffusion-weighted imaging using HP ^{129}Xe to visualize pulmonary microstructural changes

As a replacement for the established hyperpolarized ^{3}He, we studied the viability of ^{129}Xe diffusion-weighted imaging in obtaining its apparent diffusion coefficient (ADC). Imaging was carried out in healthy volunteers, age-matched controls and subjects with chronic obstructive pulmonary disease. We hypothesized that ^{129}Xe ADC would be lower in the healthy volunteers and will show an age-related increase in the ADC. Also, age-matched healthy volunteers were expected to have a lower ADC than the subjects with emphysema. The details of this study are presented in ***chapter 3****.*

II) Enable semi-quantitative dissolved-phase imaging by acquiring both the gas and dissolved-phase images in a single-breath

The moderate solubility of ^{129}Xe *yields chemically shifted resonances in the barrier tissue and red blood cells, collectively termed as the dissolved-phase. The dissolved-phase to first order depicts gas-exchange in the lung. While this dissolved-phase can be imaged separately from the xenon in the gas-phase, it requires the simultaneous acquisition of the gas-phase image for its quantitation. As a result, we developed a 3D radial pulse sequence to acquire both images in a single breath. The details behind the radial pulse sequence are presented in* ***chapter 2****, and* ***chapter 4*** *details the modifications to the sequence and its clinical translation. As an application of the technique we studied the impact of posture on the regional distribution of the dissolved-phase (****chapter 5****). We hypothesized that the dissolved-phase signal after correcting for the gas-phase signal contribution would be higher in the dependent lung in both the supine and prone postures.*

III) Use HP ^{129}Xe gas-transfer spectroscopy to establish a global biomarker for gas-transfer impairment

Most interstitial lung diseases cause inflammation of the interstitial tissue, which results in diffusion limitation and consequently, impaired gas-exchange. This chapter uses global dissolved-phase spectra to show that 'perfusion-limited' xenon can be used to measure diffusion limi-

tation in subjects with idiopathic pulmonary fibrosis. Additionally, this chapter lays the groundwork needed to enable independent imaging of xenon in the barrier and the RBCs.

IV) Generate regional biomarkers of gas-transfer by creating separate images of HP ^{129}Xe in the barrier tissue and red blood cells

While the previous aim focused on obtaining global information using gas-transfer spectra to quantify diffusion impairment, by imaging the uptake of ^{129}Xe directly into the alveolar capillary blood stream, we would be truly imaging gas-exchange in the lung, and will be ideally poised to study regional changes induced by pulmonary diseases. This goal has been achieved using a 3D 1-point Dixon acquisition. The theory behind these techniques is presented in ***chapter 2****.* ***Chapter 7*** *details the acquisition methods, phase processing, and results obtained using these techniques in a water-cyclohexane phantom, and the preliminary results in healthy volunteers and subjects with idiopathic pulmonary fibrosis.*

2. Relevant Theory

2.1. Pulmonary Physiology

The topics covered here present an overview of the functions of the lung that are relevant to my thesis. This sub-section has been adapted from the book 'Respiratory Physiology: The Essentials' by John West.

2.1.1. Structure of the Lung

While the lung participates in the metabolism of certain compounds, and aids in the body's defense as a filter for airborne particulate matter, the primary function of the lung is in exchanging gases with the capillary blood stream. The structure of the lung is primed to make this process extremely efficient.

The flow of gases begins at the trachea, which branches out at the carina to form the bronchi that feed into the right and left lung. These main-stem bronchi continue to branch out in a fractal manner and get progressively narrower, to yield a total of 23 generation of airways. The first 16 generations ('conducting zone') do not participate in gas-exchange, and in an adult human, contribute only ~150 ml to the total volume of the lung. However, diseases such as asthma and chronic obstructive pulmonary disease (COPD) can affect these conducting airways, thus affecting the transfer of gases to these gas-exchanging regions. The later generations of airways however ('terminal bronchioles'), have tiny air-sacs or alveoli that participate in gas-exchange. These alveoli, while only about 300 microns in diameter, contribute as total of ~3 L to the total lung volume in a healthy adult, and are rightfully termed the 'respiratory zone' of the lung. These alveoli are separated from the capillary network by the blood-gas barrier. This barrier is composed of three layers – the alveolar epithelium, the interstitium (extra cellular matrix), and the capillary endothelium. In certain regions, the overall thickness of the blood-gas barrier is only about third of a micron. As there are ~500 million alveoli in the lung, with an extremely thin blood-gas barrier (<1 μm), this provides the enormous surface area (50 – 100m^2) needed for efficient gas-exchange. However, this efficiency can be disrupted, as the delicate structure of the alveoli can be impacted by the onset of certain diseases. For example, emphysema, a phenotype of COPD, may cause alveolar degradation which results in a loss in the surface area, thus minimizing gas-transfer. Interstitial lung diseases on the other hand, cause a thickening of the alveolar interstitium, limiting the diffusion of gases across the blood-gas barrier.

The blood flow to the lung begins at the right atrium of the heart which pumps the deoxygenated blood through the pulmonary arteries. The pulmonary arteries track the bronchi and have a branching pattern that mirrors that of the bronchi. These arteries continue to branch and reduce in size until they form a dense network of capillaries. These capillaries have a diameter of about 10 microns which is just large enough to fit one red blood cell. The capillary network forms a fine mesh around walls of the alveoli resulting in an enormous surface area for gas-exchange. This process is so efficient, that in healthy adults at rest, the capillary blood spends only about 0.75 s in the capillary network. However, this gives it sufficient time for it to be fully oxygenated. This network terminates in the pulmonary veins which feed the oxygenated blood back to the left atrium, and then this oxygenated blood gets pumped to the rest of the body by the systemic circulation.

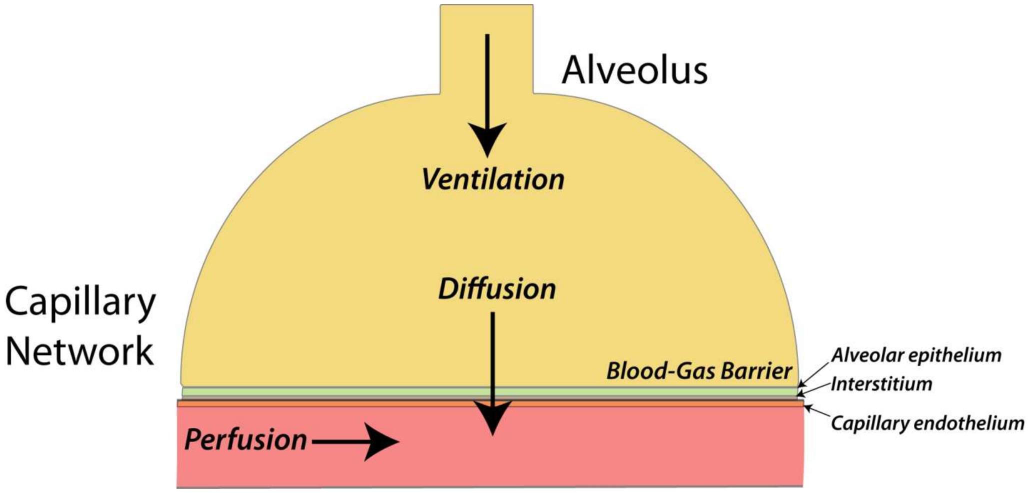

Figure 2: A simplified block diagram showing the three main processes governing gas-exchange in the lung.

2.1.2. Gas-exchange

As shown in **figure 2** above, there are three processes that determine the efficiency of pulmonary gas-exchange: ventilation, perfusion, and diffusive gas-transfer. Failure of any one of these processes will result in improper gas-exchange and ultimately hypoxemia – low oxygen saturation of the blood in the pulmonary arteries.

2.1.2.1. Ventilation & Perfusion

Ventilation (V) and perfusion (Q) are two processes that need to be well 'matched' to ensure an adequate transfer of oxygen to the blood stream. In the field of pulmonary medicine, the ratio of ventilation and perfusion is used as a surrogate marker of regional oxygenation and gas-exchange. Interestingly, this ratio is not homogenous, and speaks to the heterogeneity of both ventilation and perfusion. This is graphically illustrated in **figure 3** below (adapted from (50)). In a healthy lung, both ventilation and perfusion have shown a preferential enhancement in the gravitationally dependent portion of the lung (51,52). This heterogeneity informs us that the lung possesses a large reserve capacity for gas-exchange.

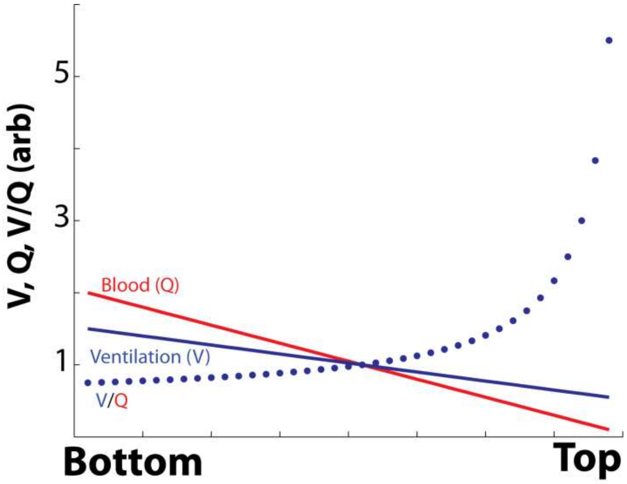

Figure 3: Ventilation and perfusion is heterogeneous, and increases in the gravitationally dependent lung. With the subject upright, we would see greater signal in the bottom of the lung. The V/Q as a result, is also heterogeneous.

The value of V/Q indicates the changes in regional pulmonary function. When perfusion is active in an alveolar unit that is unventilated, this results in a ‘shunt’ and would give a V/Q of 0. Consequently, within this alveolar unit, this may result in an increase in the partial pressure of CO_2 in the blood, and a decrease in its oxygenation. In contrast, a region that is ventilated, and not perfused, will have a V/Q of infinity. This would also result in decreased arterial oxygen saturation. Thus, ensuring efficient gas-exchange will require a well matched ventilation and perfusion, resulting in a mean V/Q of 1. This delicate interplay is disrupted with the onset of diseases that largely affect either of these processes, or the diffusive transfer of gases between them and the mean V/Q is shifted from unity.

2.1.2.2. Diffusion

While ventilation and perfusion have been heavily studied using imaging modalities, diffusion across the blood-gas barrier has not received tremendous attention and is of most relevance to my thesis. In regions that are ventilated and perfused, efficient oxygenation of the blood will require that these processes are connected by diffusive gas-transfer. This means that the alveolar gases pass through the blood-gas barrier through passive diffusion. This process is governed by Fick's first law of diffusion, and the volume of gas taken up by the blood stream (V) can be written as

$$V \alpha \frac{A.D.(P_1 - P_2)}{T} \tag{2.1}$$

where A is the surface area, D is the diffusion coefficient, P_1-P_2 represents the alveolar-capillary partial pressure difference and T is the thickness of the medium. Thus, with their large surface area (50 – 100m^2) and extremely thin barrier, the alveoli promote efficient diffusion of gases. As this gas-exchange is very efficient, the blood spends a short time within the capillary network. In a healthy adult, the heart pumps about 6 L of blood per minute, or about 100 ml per second. The volume of the blood within the capillary network is about 75 ml. Hence, through this back of the envelope calculation, the blood is estimated to spend only about 0.75 sec within the capillary network. Given such a short time frame, the transfer of gases to the capillary blood stream must be almost instantaneous. For example, in a healthy lung, oxygen saturates the capillary blood stream within ~200 ms. However, if the interstitial barrier becomes inflamed, this diffusive transfer of oxygen is impeded, and gets progressively worse with increased thickening.

A number of tracer gases (CO, NO) have been used as surrogates to study the transfer of oxygen in the lung. While oxygen is impacted by both diffusion and perfusion, the bulk transfer of these tracer gases may be primarily controlled by either diffusion or perfusion. For example, the diffusion capacity of the lung for carbon monoxide, or DL_{CO}, is used as a surrogate marker to study global gas-exchange in the lung. Carbon monoxide (CO), has a high affinity for hemoglobin. It quickly interacts with it to form carboxy-hemoglobin. As a result, the alveolar-capillary partial pressure gradient (equation 2.1) for carbon monoxide is always maintained, and as shown in **figure 4A** (red curve), CO never fully saturates the capillary blood stream. The uptake of carbon monoxide, while influenced by perfusion, is dictated by its diffusion across the blood-gas barrier, making it a diffusion-limited gas. On the other hand, nitrous oxide has no affinity for hemoglobin, and when inhaled, its concentration in the capillary blood stream increases very quickly. Consequently, as the blood gets more saturated, the alveolar capillary partial pressure gradient (equation 2.1) is slowly nullified, and the bulk transfer of N_2O stops. Hence the transfer of nitrous oxide is not determined by the diffusion properties of the lung, and further increasing the transfer of N_2O across the barrier into the blood stream would require increasing the perfusion. As a result, nitrous oxide is a perfusion-limited gas (**figure 4A**; adapted from (50)). **Figure 4B** shows that oxygen, depending on the interstitial thickness, can transition from being a perfusion-limited gas, to a diffusion-limited gas. Interestingly, while ^{129}Xe is classically defined as a perfusion-limited gas, **chapter 6** shows that this gas can be used to measure diffusion limitation.

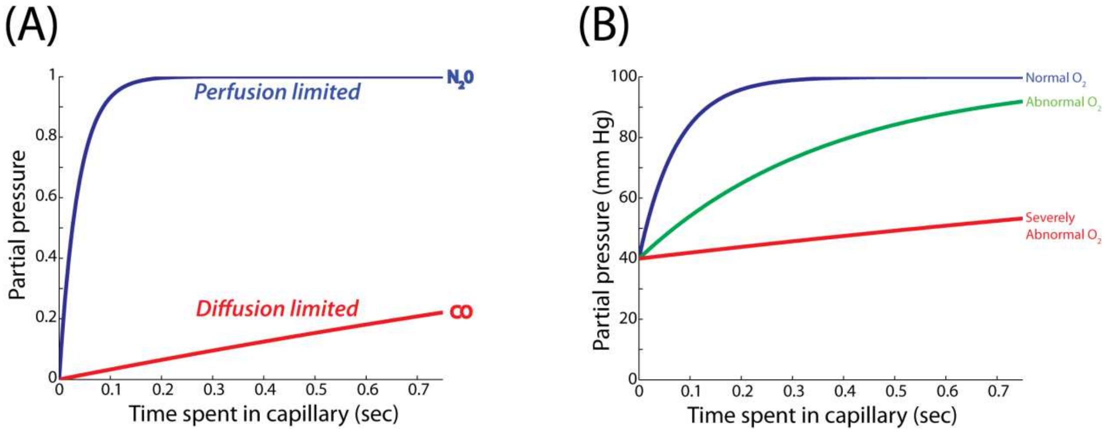

Figure 4: (A) Shows the uptake of CO and N_2O in the lung. The transfer of N_2O is not limited by the diffusion properties of the lung, and is hence perfusion limited. CO on the other hand is limited by the diffusion properties, and never saturates the intersitium. (B) Depending on the interstitial thickness, the uptake of oxygen can either be perfusion or diffusion limited.

As a global metric of gas-exchange, single breath measurements of DL_{CO} have been well established and this is the current clinically accepted gold standard to test for pulmonary diffusion limitation. The measurement is carried out with the subject in an enclosed chamber. Before the measurement begins, the subject is coached to perform a forced exhalation to functional residual capacity. Subsequently, the subject inhales the contents of a gas mixture which consists of 0.3% of CO and a tracer gas (CH_4, Ne, He), and holds their breath for about 10 seconds (53). The additional tracer gases are used to measure the dilution of CO and calculate the alveolar volume (53). After the breath hold, the subjects are instructed to exhale the gases completely and the CO concentration in this exhaled gas is used to determine the DL_{CO}. In order to ensure reproducibility, the measurements are repeated to get an accurate reading. The amount of CO taken up by the blood stream can be estimated using Fick's first law shown in equation 1. In healthy lungs, as the partial pressure for CO in the alveolar blood is infinitesimally small, the partial pressure gradient is primarily determined by the alveolar partial pressure for CO. By rewriting AD/T as D_L in equation 2.1, it can be written as:

$$D_L = \frac{V_{CO}}{Pa_{CO}} \tag{2.2}$$

The DL_{CO} depends not only on the diffusion across the blood-gas barrier, but also on the reaction rate of the gas with the capillary blood stream. Therefore, the net DL_{CO} can be treated as a series of resistances – resistance to cross the blood-gas barrier (D_M) and the rate of reaction with the hemoglobin (θ). The final equation for DL_{CO} can be written as:

$$\frac{1}{DL_{CO}} = \frac{1}{D_M} + \frac{1}{\theta V_C} \tag{2.3}$$

where V_C is the capillary blood volume.

Even though DL_{CO} is the current gold standard, it does have a few drawbacks (53). ***First***, gas-exchange is measured using the bulk transfer of CO in the blood stream. This requires good subject cooperation, and an accurate breath hold set between 9 and 11 seconds. ***Second***, even though DL_{CO} is a measure of gas diffusion at the capillary level, the measurement is made using the exhaled gas-mixture at the mouth. Hence, an accurate measurement of bulk transfer of CO also requires that the exhalation be completed within a fixed time. ***Third***, these measurements are sensitive to the changes in the external temperature, and the associated variability in DL_{CO} can be as high as 7%. ***Lastly***, and most importantly, the measurement of DL_{CO} shows a large variation from site to site, and for a given subject, has been reported to be as much as 50% (54). Hence, there is a need to study gas-exchange using methods that are less restrictive. Moreover, the study of diseases such as idiopathic pulmonary fibrosis would be greatly aided by creating images of diffusive gas-exchange. This regional information would greatly help assess lung function, and additional help longitudinally monitor response to therapy.

2.2. Relevant MR Theory

As the goal of my thesis is extract information about pulmonary function using hyperpolarized gas MRI, this section aims to establish some of the basic theory behind MRI and hyperpolarized gases.

2.2.1. Magnetization

All elementary particles possess an angular momentum or 'spin' and in nuclear magnetic resonance, we are primarily concerned with the proton spin. This angular momentum gives rise to a magnetic moment. This is given by equation 2.4, where J is the angular momentum.

$$\mu = \gamma \vec{j} \tag{2.4}$$

For spin-1/2 systems, such as hydrogen (^{1}H), when in the presence of an external magnetic field, these spins align parallel (spin up) or anti-parallel (spin down), with the direction of this magnetic field. The relative abundance of the number of spins in the spin-up (↑) or spin-down (↓) state is dependent on the strength of the magnetic field (B_0), and the temperature of the system (T). This relative abundance leads to a spin excess and hence, thermal polarization, which imparts a net magnetic moment of the spins. At thermal equilibrium, this thermal polarization given by

$$P_{thermal} = \frac{\gamma h B_0}{2kT} \tag{2.5}$$

where γ is the gyromagnetic ratio, h is Planck's constant and k is Boltzmann's constant.

At body temperatures (37° C) and field strengths of 1.5 T, this polarization, is dominated by the thermal component (kT) shown in equation 2.5 and for protons, results in a low thermal polarization of only about 5 ppm. Although the polarization of a single nucleus is minimal, as there are 110 moles per liter of protons in a gram of tissue, this large 'spin-density' leads to a significantly larger signal source. The sum of the net magnetic moments of all the spins in a given sample, gives rise to the overall thermal magnetization in the sample shown in equation 2.6.

$$M_0 = \frac{\gamma^2 h^2 B_0 \rho_0}{4kT} \tag{2.6}$$

where ρ_0 is the spin density of protons in the sample.

In the lung however, this magnetization is greatly reduced due to the lower spin density of protons. Imaging the lung is further complicated by the air-tissue interfaces that cause the weak signal to decay faster (T_2* between 0.3 – 5ms (18)). This short T2* can be overcome by using short echo times made available by UTE sequences (18). While these sequences also use rapid repetition times (TR), this is limited by the longer T_1 (~1.2 s) of the parenchyma (18). As an alternative, hyperpolarized (HP) noble gases were introduced as external contrast agents to probe the structure and function of the lung. However, the thermal signal that can be obtained using noble gases is much smaller than that of protons owing to its lower gyromagnetic ratio, lower polarization (~1 ppm at 1.5T), and primarily because of its lower spin density (55 moles per liter). As a result, these isotopes are subjected to 'hyperpolarization' to externally induce a much higher magnetic moment to overcome the lower thermal polarization and spin density, by increasing their signal by 5 orders of magnitude.

2.2.2. Spin-Exchange Optical Pumping

Spin exchange optical pumping (SEOP) is the most effective method for polarizing xenon in terms of throughput and absolute polarization. In SEOP, the angular momentum of a photon is imparted unto the lone valence electron of an alkali metal which causes this electron spin to become aligned, and this electron spin is then transferred to the nucleus of the noble gas of interest (55).

The first step in this process imparts a quantum of angular momentum to the valence electron of an alkali metal vapor – *optical pumping*. The alkali metal (in our case, 1 g of rubidium) is contained in a glass cell housed in an oven. Rubidium (Rb) melts at 40° C, and when heated to 150° C provides enough vapor pressure (5ppm of an atmosphere) to absorb ~50% of our broadband (2 nm FWHM) photons at 795 nm. 100 W of this 795-nm light is circularly polarized and illuminates the cell parallel to a uniform magnetic field of 20 G. This wavelength is tuned to the absorption energy of the D1 resonance of the Rb valence electron. Once absorbed, the electron is excited into a higher energy state, and its subsequent collisions with nitrogen quenches it, and it almost instantaneously decays back to ground state. When it does, however, it may fall into either the spin up or the spin down state. But because only the spin down state selectively absorbs our 795 nm photons to conserve angular momentum, the Rb electrons reach high polarizations through a "depopulation" of the spin down state. The cell temperature is set to achieve a balance between an even distribution of absorbed photons and mitigation of deleterious spin-destruction effects. Once the cell is at an adequate temperature, a mix of 1% Xe, 10% N_2 and 89% ^{4}He is flowed through the cell at a rate of ~1.6 SLM. The additional buffer gases (^{4}He, N_2) serve to increase the absorption cross-section of the Rb D1 transition which ensures efficient absorption of the laser light by the rubidium vapor, and to quench the excited state Rb. The nitrogen gas further serves to prevent unwanted, depolarizing fluorescence of excited Rb within the cell by absorbing the excess energy into its rotational and vibrational modes (heat).

The second step in the polarization process is the exchange of angular momentum between the rubidium valence electron and the ^{129}Xe nucleus – *spin exchange*. In the cell, the polarized rubidium interacts with the nuclei of ^{129}Xe atoms through two processes: binary collisions and molecular interactions (van der Waals molecules). During these processes, there is a transfer of angular momentum from the Rb electron to the nucleus of the ^{129}Xe atom, also known as Fermi contact hyperfine interactions. Once polarized, ^{129}Xe travels along with the buffer gases into a pyrex coldfinger immersed in liquid nitrogen (77 K). As xenon freezes at 165 K, it is frozen into the coldfinger, while other gases flow over it. Once frozen, the solid mix is kept in a constant magnetic field (2000 G), to minimize dipole couplings with the quadrupolar ^{131}Xe (55), thereby increasing the T1 of ^{129}Xe to levels that allow extended accumulation times up to an hour. Once the cryogenic accumulation is complete, the xenon is thawed using warm water and evacuated into a perfluoro polymer bag (Tedlar or ALTEF) and sealed, then placed into a 20 gauss magnetic field for storage until use, now polarized to ~10%. **Figure 5** shows a simplified diagram explaining the polarization process.

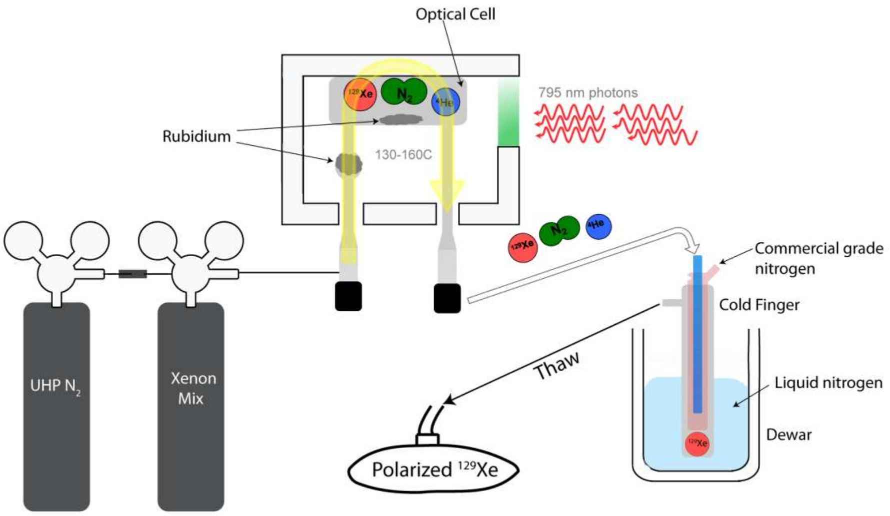

Figure 5: Simplified diagram showing hyperpolarization of ^{129}Xe using spin exchange optical pumping. The optical cell is maintained at a temperature of about 150° C to increase the vapor pressure of rubidium. Circularly polarized laser light tuned to a wavelength of 795 nm is illuminated into the cell to polarize the rubidium vapor. A mix of helium, xenon and nitrogen is then flowed into the optical cell. Collision between the polarized rubidium and ^{129}Xe results in a transfer of the angular momentum from the rubidium valence electron to the ^{129}Xe nucleus, which thus polarizes the ^{129}Xe nucleus.

The polarization is measured using a calibrated polarization measurement station (Model 2881, Polarean Inc, Durham NC). In this station, a 20 G magnetic field is created by two Helmholtz coils and a low flip-angle RF pulse is applied on the polarized ^{129}Xe using a surface coil tuned to the xenon frequency (~24 kHz). Broadly, the polarization of the sample is measured by comparing the signal obtained from the HP gas sample, to its own thermal polarization. A small RF pulse (α_{Xe}) is used to obtain an FID (free induction decay) from the bag of polarized ^{129}Xe. Once the bag has decayed down to its thermal signal, a larger RF pulse (α_T) is used obtained a reference FID. The polarization of the bag of xenon (P_{Xe}) is thus given by

$$P_{Xe} = P_T \frac{S_{Xe}}{S_T} \frac{\sin \alpha_T}{\sin \alpha_{Xe}} \tag{2.7}$$

Where P_T is the thermal polarization, S_{Xe} and S_T are the amplitudes of the FIDs obtained from the polarized and the thermally polarized xenon respectively.

2.2.3. Pulse sequence considerations for HP Gas imaging

HP gas MRI, unlike traditional ^{1}H MRI, is limited by its non-renewable thermal magnetization, and hence requires unique acquisition strategies. Apart from the non-renewable thermal signal, HP gases and more specifically ^{129}Xe have certain characteristics that impose a few restrictions on pulse sequence design (56). ***First***, HP gases have a non-equilibrium magnetization which has a finite lifetime in the lung (T_1). Furthermore, this finite lifetime is lowered by dipole interactions between paramagnetic oxygen and xenon. The ^{129}Xe T_1 is proportional to the regional oxygen concentration in the lung, and for an oxygen concentration range of 9 – 33 amagat, the T_1 was shown to vary between 0.3 s to 0.07 s (57). Also, the application of RF pulses chips away at this magnetization and lowers it by the cosine of the flip angle applied. ***Second,*** being a gaseous contrast agent, the diffusivity of the gas is much higher than that of ^{1}H (~1×10^{-5} cm^2/s versus 0.14 cm^2/s for ^{129}Xe at infinite dilution (58)), which is also dependent on the regional concentration of the HP gas (58). Lighter alveolar gases such as N_2 and O_2, increase the diffusivity of the heavier ^{129}Xe. ***Third,*** clinical imaging sequences require the acquisition to be completed in a single short breath-hold of about 15 seconds.

As a result of these restrictions, pulse sequences for HP gases are limited to fast sequences that can adequately sample k-space in a single breath hold and low flip-angles that effectively use the magnetization, and yet minimize blurring of the image. As RF refocused sequences such as the fast spin-echo require a much larger echo time, and also a large flip-angle, most of HP gas imaging has been done using the fast gradient re-called echo (FGRE) pulse sequence (59). To further minimize the TE, these sequences have also exploited the Hermitian symmetry property, which describes the relationship between k-space – $k(x,y)$ and its complex conjugate – $k^*(x,y)$. This is shown in **equation 2.8**.

$$k(x,y)=k^*(-x,-y) \tag{2.8}$$

This allows us to acquire only part of k-space, which minimizes the echo-time, diffusion-based attenuation and overall scan time.

The ideal flip-angle for HP gas MRI is significantly lower than 90°, and can be estimated by maximizing the amplitude of the center of k-space after the nth RF pulse (S_n) has been applied. This can be derived as shown below.

$$S_n = S_0 (\cos\alpha)^{n-1} \sin\alpha \tag{2.9}$$

where S is the signal at the center of k-space and the subscripts indicate the RF pulse number, α is the flip-angle. In order to ensure minimal decay of k_0, we would like to maximize S_n with respect to α. Hence,

$$\frac{dS_n}{d\alpha} = 0 \tag{2.10}$$

$$(n-1)(\cos\alpha)^{(n-2)}(\sin\alpha)^2 = (\cos\alpha)^n \tag{2.11}$$

Solving for α, we get

$$\alpha = \tan^{-1}\frac{1}{\sqrt{(n-1)}} \tag{2.12}$$

For Cartesian sequences that use sequential encoding of k-space, the 'n' in **equation 2.12** will refer to the number of phase-encodes needed to get to the center of k-space. Hence for 128 phase-encodes, the flip-angle that maximizes the center of k-space is 7.2 degrees.

2.2.4. Diffusion-weighted Imaging

As seen in **equation 2.1**, efficient transfer of gases to the blood stream requires a large surface area, and a thin intersitium. While a good portion of my thesis is dedicated to the diffusion of gases across this intersitium, it is also important to probe the changes in the alveolar surface area. Interestingly, this can be achieved by probing the diffusion of gases *within* an alveolus. In the healthy lung, while the diffusion of hyperpolarized gases is heavily restricted by the alveolus, with the onset of diseases like emphysema, which induces extensive alveolar destruction, the gases are now freer to diffuse. This change in the diffusion of a gas can be used to indirectly probe the underlying change in the alveolar microstructure. The information of gas diffusion can be indirectly measured using ventilation images. However, the pulse sequences that are used to acquire ventilation images must be modified to include additional gradients that can sensitize the images for this diffusion. Based on the underlying pulse sequence (spin-echo or gradient echo) these diffusion sensitizing gradients can be either unipolar or bipolar. For a GRE sequence, bipolar diffusion sensitization is applied, and is done before the readout gradient. An example of bipolar gradients is shown in the figure below (adapted from (60)).

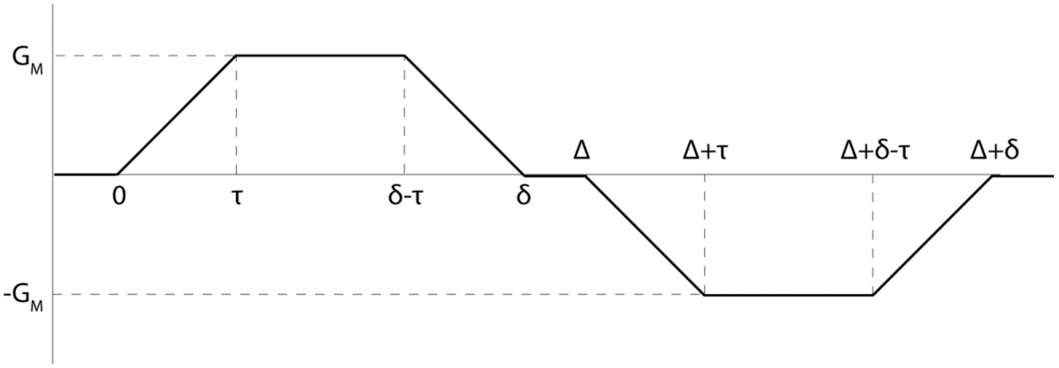

Figure 6: The bipolar gradients shown here (Stejskal-Tanner gradients) are used to sensitize for diffusion. The strength of the diffusion weighting (b-value) is determined by the gradient strength, and the timing parameters (τ, Δ, δ).

The application of such gradients will induce an additional phase to spins that experience a displacement, which cannot be re-phased. The extent of phase accumulation will vary as a function of the ramps, and the duration and amplitude of the gradients. Consider that during the application of the positive half of the diffusion gradient, a set of spins diffuse by a root mean squared distance r(t) ($\sqrt{2Dt}$, where D is the diffusion coefficient and t is the time) then they will experience a change in their resonance frequency ($\Delta\omega$). Consequently, this motion will cause the spins to accumulate some phase φ, which depends on the amplitude of the gradients (G), and is given by

$$\varphi(t) = \int_0^t G(t)\,\mathrm{r(t)}\,dt \tag{2.13}$$

As long as spins remain stationary during the application of both diffusion gradients, the phase imparted to the stationary spins during the positive half of the diffusion weighting gradient will be refocused by the application of the negative rephasing gradient lobe. However, the phase accumulated by the motion of spins, cannot be refocused by the negative gradient lobe. This results in an exponential loss in the measured signal, which depends on the 'b-value' or the strength of the diffusion weighting gradient, and mainly, the degree of molecular diffusion (D). Hence, by acquiring images with and without the diffusion-weighting gradients, the signal intensities of the resulting images ($S_{Weighted}, S_{non-weighted}$) can be used to calculate the 'apparent diffusion coefficient' (ADC) on a pixel-by-pixel basis.

$$S_{weighted} = S_{non-weighted} e^{-b.ADC} \tag{2.14}$$

Depending on the extent of molecular diffusion, the amount of diffusion-weighting can be controlled by adjusting the 'b-value' of the gradients. For example, compared to gases, water molecules experience lower diffusion, which is on the order of 1x10^{-5} cm^2/s, and hence typical b-values used for ^{1}H diffusion studies are on the order of 1000 s/cm^2. However, HP gases, especially ^{3}He (ADC ~ 2 cm^2/s at free diffusion), diffuse rapidly, and imparting significant diffusion attenuation requires lower b-values (<10 s/cm^2). This b-value depends on the shape of the gradient used and can be calculated by integrating the following equation (61)

$$b = (2\pi)^2 \int_0^{TE} \vec{k}(t).\vec{k}(t)dt \tag{2.15}$$

Where $k(t)=\frac{\gamma}{2\pi}\int_0^t \vec{G}(t)dt$, and is the net phase imparted by the gradient lobe. The resulting b-value for the bipolar trapezoidal gradients shown in **figure 6** can be written as (60):

$$b=\left(\gamma G_M\right)^2\left[\delta^2\left(\Delta-\frac{\delta}{3}\right)+\tau\left(\delta^2-2\Delta\delta+\Delta\tau-\frac{7}{6}\delta\tau+\frac{8}{15}\tau^2\right)\right] \quad (2.16)$$

While the diffusivity for HP ^{129}Xe (0.14 cm^2/s at infinite dilution) is higher than water, the challenges in implementing diffusion weighted imaging with xenon, arise from its lower gyromagnetic ratio. Thus obtaining adequate diffusion weighting (b-value of ~12 s/cm^2) with the highest clinical gradient strength (3.2 G/cm), would need longer diffusion gradients (~2.5 ms). This increases the minimum achievable echo time, increasing the T_2* attenuation. In spite of this challenge, high quality diffusion weighted images were acquired, and this will be discussed in **chapter 3**.

2.2.5. Radial Acquisition for HP Gases

HP gases, and more specifically ^{129}Xe, exhibit large diffusion coefficients, have a short T_2*, and require short scan durations (~15 seconds). These properties favor imaging their distribution using radial acquisition strategies. Unlike Cartesian sequences that raster through k-space, radial sequences as the name suggests, sample k-space radially. The radial acquisition offers the following advantages. ***1)*** *B*y using a center-out acquisition strategy, the ‘echo-times’ that can be generated with this sequence are well below a millisecond. This enables imaging chemical species that have a very short T_2* and hence can generate images with a reasonable SNR. This property is especially useful for imaging the dissolved-phase of ^{129}Xe, as discussed in **chapters 4** and **5**. ***2)*** This acquisition strategy densely over-samples the lower frequencies of k-space which helps minimize artifacts introduced by motion. This is helpful while imaging the lung, as this helps negate any artifacts introduced by the motion of the heart. ***3)*** As the gases have a larger diffusion coefficient, the attenuation introduced by diffusion-based accumulation of phase will be pushed to the edge of k-space. ***4)*** As shown by Scheffler *et al*. (62), radial acquisitions are also robust against the under-sampling of k-space. Thus radial acquisitions can be limited to a single breath-hold by acquiring fewer rays, or views of k-space, well below the Nyquist limit.

While the 2D radial acquisition samples a circular path in k-space, the goal with any 3D radial acquisition is to follow a trajectory that uniformly samples the surface of a sphere (63). In order to ensure uniform sampling of the surface of a sphere and thus minimize aliasing, the equations used for the 3D radial acquisition describe an Archimedean spiral through k-space (63). In addition to ensuring uniform k-space sampling, this acquisition strategy also reduced the number of views needed to satisfy the Nyquist condition by 50%. The Archimedean spiral trajectory indicated by the equations below, will sample the surface of a sphere, when scaled by the maximum gradient amplitude.

$$G_X(n) = \cos\left(\frac{Pn\pi}{180}\right)\sqrt{1-\left(1-\frac{2n}{N}\right)^2}$$

$$G_Y(n) = \sin\left(\frac{Pn\pi}{180}\right)\sqrt{1-\left(1-\frac{2n}{N}\right)^2}$$

$$G_Z(n) = \sqrt{\left(1-(G_X^2+G_Y^2\right)} \qquad (2.17)$$

where N is the number of views of k-space, n is the view number, n=1,2 … N, and P is an empirically chosen prime sampling factor used to randomize samples along the X-Y plane. This empirically chosen prime-sampling factor ensures the uniform sampling of the edge of the sphere, even when tremendously under sampled. This is illustrated in **figure 7**.

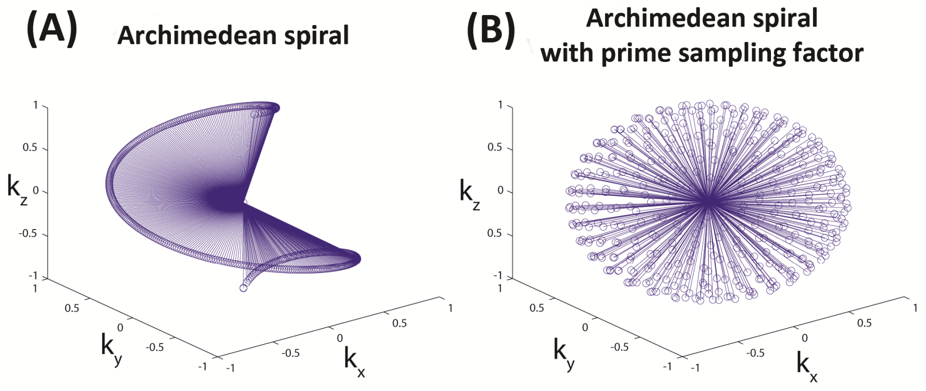
(A) Archimedean spiral

(B) Archimedean spiral with prime sampling factor

Figure 7: 3D radial acquisition of k-space, which uniformly samples the edge of a sphere. (A) shows an Archimedean spiral trajectory with just 400 views. This clearly shows non-uniform sampling of the edge of a sphere. (B) shows the Archime-

dean spiral with the same number of views, but with an empirically chosen prime sampling factor of 101. This ensures the uniform sampling of k-space, even when tremendously under-sampled.

The number of views required to adequately sample the edge of k-space is dictated by the area of subtended between each view at the surface of the k-space sphere (61) as described by **figure 8**.

$$k_{max}\Delta\Omega \leq \Delta \mathrm{k}^2 \tag{2.18}$$

where $\Delta\Omega = \sin\theta\Delta\theta\Delta\varphi$ is the solid angle subtended by the views at the edge of a sphere. As we ensure equiangular sampling of k-space, $\Delta\theta$ can be described as

$$\Delta\theta = \frac{1}{k_{max}L} \tag{2.19}$$

where L is the field of view (FOV). Similarly,

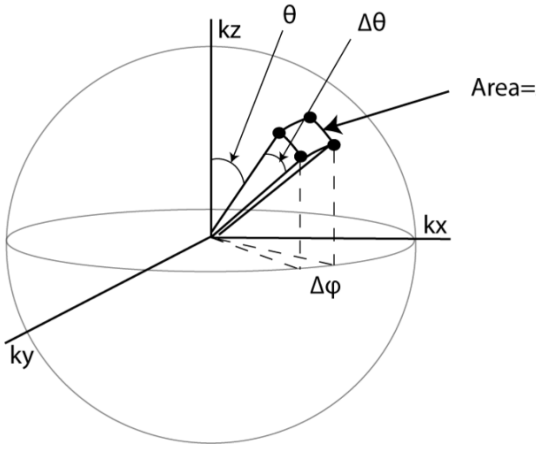

Figure 8: The calculation of Nyquist limits for the 3D radial sequence, adapted from (61).

$$\Delta\varphi = \frac{1}{k_{max} L \sin\theta} \tag{2.20}$$

As there are 4π spherical radians in a sphere, to satisfy the Nyquist condition, this solid angle can be obtained by acquiring N_S number of views of k-space, $\Delta\Omega = \frac{4\pi}{N_S}$.

Using **equations 2.19** and **2.20**, N_S can be written as

$$N_S = 4\pi\left(k_{max} L\right)^2 \tag{2.21}$$

As $k_{max} = \frac{1}{2\Delta x}$ and $\Delta x = \frac{L}{npts}$, for a center-out radial acquisition, **equation 21** is written as

$$N_S = \pi\left(npts\right)^2 \tag{2.22}$$

Hence for a 64×64×64 acquisition, the number of views of k-space required is ~12900 views.

2.2.6. Non-Cartesian Image Reconstruction

Although non-Cartesian acquisitions are preferred for imaging HP gases, they have yet to be widely adopted as their reconstruction remains moderately challenging. While Cartesian data acquired on an equally spaced rectilinear grid can be reconstructed rather simply using the FFT, non-Cartesian image reconstruction is impacted by the non-uniform sampling density of the data. As the FFT requires uniformly spaced data, this requires that non-Cartesian k-space data be re-sampled onto a uniform Cartesian grid, before the data can be Fourier transformed.

A commonly used approach to reconstruct non-Cartesian data is convolution gridding (64). Fundamentally, each point in k-space is convolved with a kernel (C), compensated for the density of samples (W), and then recast onto a cartesian matrix (R), and then finally Fourier transformed to yield the final image. This can be described mathematically as [Pipe]

$$m(x,y) = FFT\left(\left\{\left[\left(M(u,v)*W(u,v)\right)\otimes C\right]*R(u',v')\right\}\otimes^{-1} C\right) \tag{2.23}$$

where, M(u,v) is the radially acquired frequency domain data, and m(x,y) is the regridded Cartesian k-space data.

While non-Cartesian reconstruction was not the focus of my thesis, our group has made significant advances with radial reconstruction that has improved the quality of dissolved-phase images. Specifically, the following aspects of reconstruction were optimized. *First*, the choice of the convolution kernel, and the associated width, has an impact on the blurriness seen in the images. The optimal kernel, has been established in the literature to be the Kaiser Bessel (65). *Second*, while densely sampling the lower frequencies of k-space has its advantages for lung imaging, as it minimizes motion artifacts induced by the beating heart, it introduces an additional step in the reconstruction process

– density compensation (W). After the convolution gridding operation, each point in k-space was weighted in accordance with density, with heavier weighting applied to the higher frequencies of k-space. While this is still an area of active research and multiple methods that have been developed – Voronoi, hit-plane, the iterative density compensation method was chosen to be the optimal (66). After the density compensation operation, the resulting data is then cast onto a twice oversampled Cartesian grid. As we use non-slice selective pulses, this works to excite any and all xenon magnetization outside the FOV, which may fold in and cause aliasing artifacts. This oversampled grid ensures that the aliasing artifacts are pushed to the outer edges of k-space, and are minimized within the field of view. The re-gridded k-space data is Fourier transformed and cropped appropriately to give the reconstructed image. *The final step*, which had historically been neglected, is dividing the reconstructed image by the Fourier transform of the convolution kernel – deapodization. The optimized convolution kernel, deapodization, and density compensation algorithm have had a significant impact on the quality of hyperpolarized images, and the SNR has improved by 50%. This boost in SNR, in addition to providing higher quality images, has enabled the phase sensitive reconstruction of the dissolved-phase images to be discussed in **chapter 7**.

2.2.7. The Dissolved-Phase of hyperpolarized ^{129}Xe

2.2.7.1. Diffusive replenishment of HP ^{129}Xe in the alveolar septum

The signal from the xenon dissolved in the alveolar septum is derived entirely from diffusive transfer of magnetization from the airspaces. To understand the source of this signal, we must understand the mathematics of this diffusion transfer and its interplay with the RF pulses. The RF pulses used to detect xenon in the dissolved-phase also deplete its signal. But unlike the gas-phase of xenon, the dissolved-phase signal is replenished by the fresh gas-phase xenon magnetization that diffuses into these compartments. Much like the diffusion of carbon monoxide into the capillary blood, this diffusion of xenon is also governed by Fick's law. To understand and simulate the signal dynamics of the dissolved phase and understand the impact of barrier thickness on signal replenishment, Driehuys *et al.* postulated a 1D model of gas-transfer.

To model the signal dynamics of xenon in the dissolved-phase, the diffusion of xenon across the blood-gas barrier can be modelled as diffusion across the plane surface with a constant diffusion coefficient D. The entire gas-exchanging region is modeled to extend from $-L<x<L$, and the capillary extends from $-L_C<x<L_C$ and $L>L_C$. The thickness of the diffusion barrier is $L_{db} = L-L_c$. This is graphically illustrated in the figure below.

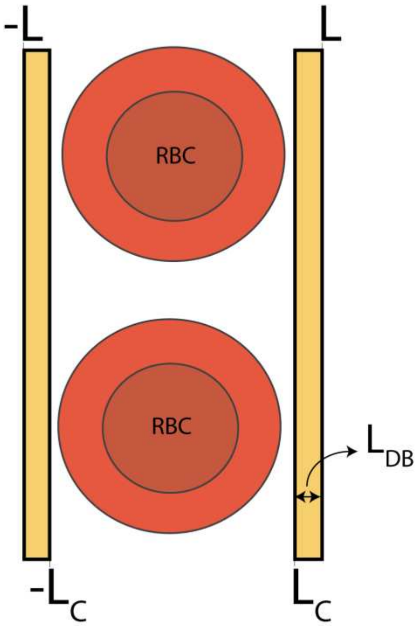

Figure 9: Graphical representation of the diffusion of xenon across a plain sheet.

To get an expression for the concentration (or magnetization) of xenon as a function of time, one needs a solution for the equation:

$$\frac{\partial C}{\partial t} = D.\frac{\partial^2 C}{\partial x^2} \tag{2.24}$$

which is Fick's second law. C is the concentration of the tracer, t is time, x is the distance, and D is the diffusion coefficient. The magnetization of ^{129}Xe in the dissolved-phase after the application of a 90 degree pulse can be obtained by solving equation 24. The solution for this equation is provided in (67) and the ^{129}Xe magnetization in the dissolved-phase M_{diss} can be written as

$$M_{diss}(x,t)=\lambda M_{air}\sum_{n=0}^{\infty}(-1)^n\left(erfc\left[\frac{(2n+1)l-x}{2\sqrt{Dt}}\right]+(-1)^n erfc\left[\frac{(2n+1)l+x}{2\sqrt{Dt}}\right]\right) \quad (2.25)$$

where λ is the fraction of the ^{129}Xe magnetization in the airspaces (M_{air}) that is in the dissolved-phase, erfc is the complement of the error function where erfc = 1- erf. While equation 25 gives the magnetization of the dissolved-phase at time t, the RBC signal (S_{RBC}) can be obtained by integrating this dissolved-phase signal from – L_C to L_C. Consequently, the barrier signal (S_{Barr}) can be obtained by subtracting the RBC signal from the integral of the dissolved signal obtained over -L to L.

$$S_{RBC}=Hct\int_{-Lc}^{Lc}M_{diss}(x,t)dx,$$ where Hct is the hematocrit

$$S_{Barr}=\int_{-L}^{L}M_{diss}(x,t)dx-S_{RBC}(t) \quad (2.26)$$

In modeling the dissolved-phase signal, we are making a few assumptions (47). ***First***, the solubility and the diffusion coefficient are considered to be constant throughout the lung. ***Second***, the T_1 of the ^{129}Xe in the dissolved-phase (T_1 of ^{129}Xe in deoxygenated blood is 2.2s, and 7.7s in oxygenated blood (68)) is longer compared the rate of signal replenishment and hence can be ignored. ***Lastly***, the capillary blood spends about 750 ms in diffusive contact with the ^{129}Xe in the alveolus. As the signal replenishment is much shorter than this capillary transit time, perfusion has not been included in the model. The solutions to the equations 2.26 can be normalized by the signal in the airspaces and written as follows (47)

$$\frac{S_{RBC}}{S_0} = \frac{4\lambda Hct\sqrt{Dt}}{L_A}\sum_{n=0}^{\infty}(-1)^n\left(ierfc\left[\frac{(2n+1)L-L_C}{2\sqrt{Dt}}\right] - ierfc\left[\frac{(2n+1)L+L_C}{2\sqrt{Dt}}\right]\right) \quad (2.27)$$

where S_0 is $M_{Air}L_A$ where L_A is the dimension of an alveolus. Similarly, the equation for the barrier can be written as

$$\frac{S_{Barr}}{S_0} = \frac{4\lambda Hct\sqrt{Dt}}{L_A}\sum_{n=0}^{\infty}(-1)^n\left(ierfc\left[\frac{2nL}{2\sqrt{Dt}}\right] - ierfc\left[\frac{(2n+2)L}{2\sqrt{Dt}}\right]\right) - \frac{S_{RBC}}{S_0} \quad (2.28)$$

The normalized S_{RBC} and S_{Barr} signals have been plotted as a function of replenishment time for a range of interstitial thicknesses in **figure 10** below.

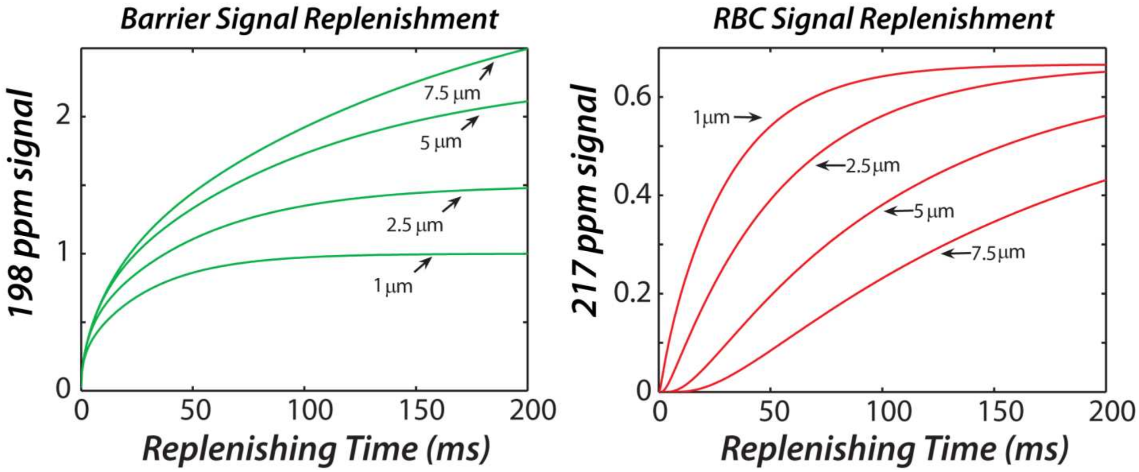

Figure 10: Barrier and RBC replenishment after the application of a 90 RF pulse. With minimal interstitial thickening, while the barrier signal increases in signal, the RBC signal shows a significantly delayed replenishment. This delay can be used as a sensitive probe of interstitial thickening.

As the barrier is immediately adjacent to the alveolar space, compared to the RBC signal, this signal replenishment begins earlier. Furthermore, it should be noted that minimal interstitial thickening of this barrier tissue delays the replenishment of the RBC signal. As seen in **figure 10**, with a nominally normal interstitial thickness of 1 μm, the RBC replenishment time begins almost immediately and is nearly complete by 100 ms. In contrast, with an interstitial thickness of 2.5 μm the RBC replenishment time almost doubles to about 66 ms. This RBC replenishment also lags the barrier signal, as the xenon diffuses into it first. The barrier signal replenishment is unaffected by this increase in thickness, and in fact shows an increase in signal intensity. Hence with a proper choice of acquisition parameters, one can weight for the delayed RBC signal replenishment. This delayed replenishment can be used as a marker of diffusion limitation, and as discussed in **chapter 6**, will form the basis for a global biomarker of gas-exchange.

2.2.7.2. Phase sensitive imaging of the ^{129}Xe in the barrier and RBCs

The low dissolved ^{129}Xe magnetization and the rapid T_2* makes dissolved-phase imaging challenging. By taking advantage of the dynamic replenishment of the dissolved-phase signal, which was highlighted in the previous section, improvement in xenon polarization, and by using rapid pulse sequences, direct imaging of the dissolved-phase was made possible. This first attempt at imaging the dissolved-phase imaging captured both the resonances in the images. One of the goals of my thesis is to create separate images of xenon in the barrier, and transiently bound to the RBCs, to get a fundamental view of gas-exchange in the lung.

The techniques I have used in phase-sensitive imaging of the dissolved-phase derive their concepts from fat-water ^1H imaging. This similarity arises as protons that are a part of the fat resonance are chemically shifted from the main water resonance by -3.5 ppm, and hence have a similar frequency difference as the resonances of the dissolved-phase of xenon (~225 Hz for fat-water, ~340 Hz for the barrier and RBC). The fat resonance is the source of chemical shift artifacts in conventional ^1H MR. As a result, the separation of fat and water has been the topic of research for multiple decades, which has yielded highly refined techniques and algorithms for fat-water separation and suppression. Some of these techniques rid the fat signal by selectively exciting only the water resonance using long RF pulses. Other approaches exploit the differences in the T_1 between fat and water, and use inversion recovery sequences to suppress the fat resonance. Long RF pulses and 180 degree flip-angles needed for these approaches are not applicable for the dissolved-phase because of its low gyromagnetic ratio (11.77 MHz/T), and short T_2^* (~2 ms).

As an alternative to RF based fat suppression, T. Dixon introduced a novel technique to create images of both fat and water (69). As the fat signal resonates 225 Hz below the water resonance, when the transmit and receive frequency are tuned to the water resonance, this frequency separation, causes the fat signal to accumulate phase with respect to the receiver. This technique introduced by T. Dixon (69) took advantage of this phase accumulation between the two resonances to separate the fat and water contributions. Two images using two different echo times, were generated using a spin-echo pulse sequence; the first image was acquired with both resonances in phase (fat + water image) and for the second image, the timing of the 180° RF pulse was adjusted to ensure the two resonances were 180° out of phase (water – fat image). Using a combination of the two images, a pure water or pure fat image could be generated. As this method used two TEs, this was the 2-point Dixon technique for fat-water separation. However, as this approach uses a spin-echo sequence, the issues that affect RF or T1 based approaches, also plague the 2-point Dixon technique. Thus the 2-point Dixon cannot be implemented to separate the components of the dissolved-phase in a single breath.

However, it is possible to use the principles of Dixon imaging to create separate images of the components of the dissolved-phase of ^{129}Xe, using just a single echo time (70). This is appropriate given its short T_2*. Using the radial pulse sequence, the echo-time is set such that the phase separation between the two resonances was 90° (**Figure**

11). At that echo time, once the phase offset with respect to the receiver has been corrected for, each receive channel will have information about one of the resonances. Hence by starting the data acquisition at that echo time, and employing a phase sensitive reconstruction, the two resonances can be separately imaged with at least the center of k-space with a 90° phase separation between the RBC and barrier. As this employs just one echo time, this is the 1-point Dixon technique. This strategy has been used in rats with the radial sequence to generate 2D images of ^{129}Xe in the barrier and RBCs (47). The echo time for a 90° phase separation (TE_{90}), can be derived as shown below.

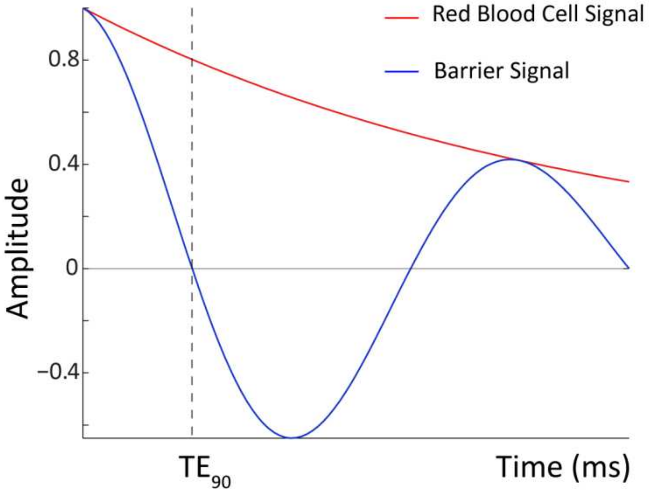

Figure 11: The variation in the amplitude of the center of k-space for the xenon in the red blood cells (on resonance; red) and the barrier tissue (blue). Data acquisition is initiated at TE_{90}, where the two resonances are 90° out of phase with each other.

The general equation for the phase difference accumulated by an ensemble of spins with a frequency difference Δf over time *t* in a magnetic field can be written as

$$\Delta\varphi(t) = 2\pi\Delta ft \tag{2.29}$$

where $\Delta\varphi(t)$ is the phase difference, γ is the gyromagnetic ratio. If the transmit and receive frequency were on resonance with the xenon in the RBCs, and the barrier was would resonate at Δf Hz lower in frequency, after a time t, the barrier being at a lower frequency will lag the RBCs by $\Delta\varphi$ degrees. At a time $t = TE_{90}$, the two resonances will be 90° out of phase $\left(\Delta\varphi = \frac{\pi}{2}\right)$. Using this information in equation 2.29, we get

$$\frac{\pi}{2} = 2\pi\Delta fTE_{90} \tag{2.30}$$

Hence, the echo time needed for a 90 phase separation can be calculated using just the frequency difference between the RBC and barrier resonances, and can be written as shown below.

$$TE_{90} = \frac{1}{4\Delta f} \tag{2.31}$$

While the 1-point Dixon technique provides a simpler approach to creating separate images of xenon in the RBC and barrier, it does require overcoming a few challenges. ***First,*** the 1-point Dixon acquisition is inherently sensitive to the inhomogeneity of the B_0 field. Moreover, any technique that uses phase to decompose chemical components will be sensitive to phase variations introduced by RF pulse imperfections, and local magnetic field inhomogeneity (71). The phase changes caused due to this inhomogeneity can be corrected for with the calculation of a B_0 map. ***Second***, the Dixon technique also does not account for the continuous evolution of phase between the two resonances after the first few k-space points have been acquired. As a result, the Dixon condition is valid only near the origin of k-space (k_0). ***Lastly***, while the two resonances may be 90° out of phase, they may still be at an arbitrary phase with respect to the receiver. Calculating this receiver phase offset requires developing calibration procedures, or as we will see in **chapter 7**, can be calculated using the acquired data. Hence, in spite of its shortcomings, the 1-point Dixon acquisition helps overcome the short T_2^* of the dissolved-phase and create separate images of its components in a single-breath.

As illustrated by the theory outlined in this chapter, my work combines the unique properties of hyperpolarized ^{129}Xe, optimized MR acquisition strategies, signal processing, and the mathematics of diffusion to provide a fundamentally new approach to studying alveolar microstructural changes, and more importantly, providing a new approach to imaging diffusive gas-exchange in the lung.

3. Imaging Lung Microstructure using Diffusion-Weighted ^{129}Xe MRI

In addition to ventilation and perfusion, the efficiency with which the lungs exchange gases depends on two structural parameters – the alveolar surface area, and the interstitial thickness. This chapter probes the changes in the alveolar surface area brought on by COPD, using diffusion weighted imaging. The results discussed in this chapter were previously published as a journal article: S.S. Kaushik *et al*., '*Diffusion-Weighted Hyperpolarized ^{129}Xe MRI in Healthy Volunteers and Subjects with Chronic Obstructive Pulmonary Disease*', Magnetic Resonance in Medicine, 2011; 65(4):1155-1165.

3.1. Motivation

3.1.1. Chronic Obstructive Pulmonary Disease (COPD)

Chronic obstructive pulmonary disease (COPD) is characterized by slowly progressing irreversible airflow limitation (72). COPD affects roughly 12 million patients in the United States, is the 3rd leading cause of death in the United States and Europe (73), and is one of the common causes of death that continues to increase in incidence. COPD describes a group of diseases (phenotypes) that include emphysema, bronchitis, and bronchiectasis. Moreover, multiple phenotypes can exist within a single individual. To treat and monitor COPD patients effectively, it will be necessary to assess the regional extent and severity of each phenotype, and to determine the predominance of one over the others (73).

To this end, thin-section computed tomography (CT) has been extensively investigated for the radiologic evaluation of COPD (8). CT can identify regions of airspace tissue destruction (emphysema) by their low x-ray attenuation, often defined as less than –950 Houndsfield units, and has shown good correlation to histology (9). CT images acquired at end-expiration can be used to visualize air trapping, and airway wall thickening can be measured in the first 6 generations (10). However, despite the power and high resolution achievable with CT, the associated radiation dose constrains its use in asymptomatic patients and in longitudinal follow-up studies (74), limiting its use for investigational purposes.

3.1.2. Hyperpolarized ^{3}He Diffusion-weighted MRI

Hyperpolarized (HP) ^{3}He MRI has established itself as a powerful, noninvasive imaging modality for diagnosis and evaluation of COPD (24). HP ^{3}He MRI provides relatively high-resolution images of ventilation, which permits areas of regional obstruction to be visualized. Beyond static ventilation imaging, ^{3}He MRI has been used to measure the apparent diffusion coefficient (ADC), which is arguably the most developed and straight forward to interpret. The principle of ADC MRI is that diffusion of ^{3}He atoms in the lung is constrained by the size of the alveolar space. Hence, the ^{3}He ADC measured in healthy lung is small [~0.25 cm^2/s in humans for typical protocols, (29)] compared to a large self-diffusion coefficient of ~2 cm^2/s. However, in regions of appreciable emphysematous tissue destruction, the ADC becomes elevated, eventually reaching a maximum value consistent with the free diffusion of ^{3}He in air (~0.8 cm^2/s). By contrast, ADC would not be expected to increase if airflow limitation was caused by an airway-predominant disease such as bronchitis.

Since the introduction of ^{3}He ADC (58,75) in small animal models of emphysema, considerable progress has been reported. In addition to revealing emphysema in patients with known COPD, ^{3}He ADC shows early emphysema-like changes in asymptomatic smokers (76) and in individuals exposed to second-hand smoke (32). The relation of ADC to alveolar size has been demonstrated by its sensitivity to postural gradients (33) and age-related changes in alveolar size (34). ^{3}He ADC MRI has proven highly reproducible in repeated studies (77) and has shown hints of disease progression in individual subjects (78). Recently, ^{3}He ADC was put on a firm theoretical footing by Yablonskiyi *et al.*, who demonstrated the ability to extract precise airspace dimensions from the ADC measurement (79). ^{3}He ADC has been compared clinically to CT, and these studies suggest that it correlates more strongly with DL_{CO} (Diffusing capacity of carbon monoxide in the lung) than the CT based metrics (80). Unfortunately, the scarcity of

^{3}He and its rapidly increasing cost have severely limited the broader dissemination of HP ^{3}He MRI.

3.1.3. Transitioning to Hyperpolarized ^{129}Xe MRI

The limitations of ^{3}He have made clear the need to transition to HP ^{129}Xe MRI, the supply of which is unconstrained. ^{129}Xe MRI has improved considerably (81)] since the first human ventilation imaging was demonstrated (25). ^{129}Xe MRI has also been implemented with diffusion weighting (58), and Mugler *et al.* first demonstrated ^{129}Xe ADC in healthy human volunteers (82), which was followed up by Sindile *et al.* (83). While Mata *et al.* demonstrated that ^{129}Xe ADC becomes elevated in an elastase-model of emphysema in rabbits (84), there have been no reports of ^{129}Xe ADC measurements in patients with COPD. Therefore, the aim of this study was to assess the clinical feasibility of ^{129}Xe ADC MRI and apply it in a population of healthy volunteers, COPD subjects, and age-matched control subjects. We report a detailed analysis of ADC trends with disease, age, and posture, and correlate the ADC values with conventional pulmonary function testing.

3.2. Methods

3.2.1. Subject Inclusion/Exclusion Criteria

Studies were conducted under the GE Healthcare Investigational New Drug (IND) as part of a Phase I clinical trial for hyperpolarized ^{129}Xe MRI, and studies were approved by the Duke University Medical Center (DUMC) Institutional Review Board (IRB). Written informed consent was obtained from the volunteers and subjects prior to enrollment. Subjects were excluded if they were pregnant or lactating; had a history of asthma, allergy, or hypersensitivity that affects the pulmonary function; had a history of cardiac arrhythmias; or had a respiratory illness (or exacerbation for COPD subjects) within 30 days of imaging.

The study consisted of a technical run-in phase for pulse-sequence development followed by an efficacy phase using a fixed version of each sequence. During the run-in phase, a group of healthy volunteers (HV) (3 men, 4 women, mean age = 32.9 ± 11.3 years) underwent the same version of the ^{129}Xe ADC MRI protocol that was used during the efficacy phase (with minor differences in b-values), and hence, these subjects are included as part of this report. These subjects met the same inclusion/exclusion criteria as the age-matched control subjects (see below), except they did not undergo pulmonary function testing.

For the efficacy phase, 1 subject with GOLD Stage I, 8 subjects with GOLD Stage II, and 1 subject with GOLD Stage III COPD were recruited from a population of patients who had a smoking history of at least 20 pack-years (7 men, 3 women; mean age = 65.9 ± 7.1 years). Given the relatively small population, Stage II patients were primarily selected to ensure observing a reasonable, but not overly variable, degree of pathology. The Stage II COPD subjects had a forced expiratory volume in 1 second (FEV_1) between 50 and 80%, FEV_1/FVC (forced vital capacity) of less than 70%. They had a single-breath carbon monoxide diffusing capacity (DL_{CO}) of less than 70% of the predicted value. The Stage I subject had an FEV_1 that was 81% of predicted and the Stage III subject had an FEV_1 that was 35% of predicted, as seen in **Table 1**. This GOLD classification is also defined in the appendix of this thesis. All COPD subjects had a chest x-ray or CT scan on file, with 8 out of 10 exhibiting evidence of emphysema, as determined by a board certified radiologist (HPM).

In addition, 10 age-matched healthy controls (AMC) were enrolled (4 men, 6 women, mean age = 62.9 ± 7.6 years). These subjects each had a smoking history of less than 5 pack-years and had not smoked for at least 5 years prior to participating in the study. Volunteers typically had an FEV_1 and DL_{CO} that were both greater than 80% of the predicted value and an FEV_1/FVC that was greater than 70%. All pulmonary function testing was conducted within one week of ^{129}Xe MRI. **Table 1** provides a complete list of all the PFT data for all subjects.

3.2.2. ^{129}Xe Polarization and Delivery

Isotopically enriched ^{129}Xe (85%) was polarized in an hour as detailed in **chapter 3**, to generate 1-L doses. With the subjects lying supine, HP ^{129}Xe was then administered from a Tedlar bag through 0.95-cm inner diameter Tygon tubing (Saint-Gobain Performance Plastics, Akron, OH). Each subject received a 1-L ^{129}Xe dose regardless of their lung volume, with inspiration commencing after exhaling to a volume estimated to be between residual volume (RV) and functional residual capacity (FRC). Imaging started within 1-2 seconds of the subject inhaling the contents of the bag. For each ^{129}Xe dose, the subject's subjects' blood pressure, heart rate, and oxygen saturation level were continuously measured using a Datex-Ohmeda monitoring system (GE Healthcare, Helsinki, Finland).

3.2.3. Hyperpolarized ^{129}Xe Imaging

Imaging was performed using a 1.5 T Excite 14M5 MRI scanner (GE Healthcare, Milwaukee WI) and a quadrature vest coil (Clinical MR Solutions, Brookfield, WI) tuned to the 17.66 MHz ^{129}Xe resonance frequency and proton blocked to enable localizing and shimming using the body coil of the scanner. Diffusion-weighted HP ^{129}Xe images were acquired in the coronal plane using a multi-slice spoiled gradient recalled echo (SPGR) sequence (field of view = 40 cm, slice thickness = 15 mm, matrix = 64×64, bandwidth = 15.6 kHz, TE/TR = 9.3/12 ms and flip angle = 5.1°). Diffusion weighting was achieved using bipolar gradients (amplitude = 3.2 G/cm, ramp time = 500 μs, and pulse width = 2.4 ms), having a b-value (60) of 12 s/cm^2. This b-value was used for all subjects except for 5 healthy volunteers, who received a slightly longer sensitizing gradient pulse width of 2.9 ms, resulting in a b-value of 18.76 s/cm^2. For each diffusion-weighted image, an accompanying unweighted image was acquired in an interleaved fashion to enable pixel-wise ADC values to be calculated from the two images. The total acquisition time was limited by the protocol to 16 seconds, thus restricting the number of slices to 10. As a result, the most anterior and most posterior slices of the lung were generally not scanned.

3.2.4. Source Image Processing

The images were interpolated by the reconstruction algorithm of the scanner from a 64×64 to a 256×256 matrix and saved in DICOM format. These images were then imported into MATLAB™ (The MathWorks, Inc., Natick, MA) to generate the ADC maps. To ensure that ADC calculations were made only on pixels corresponding to ventilated lung, several processing steps were applied to the source images. First, the non-diffusion weighted (b = 0) images were used to generate binary masks of each slice, using a threshold derived from the mean of the background noise plus twice its standard deviation. The background noise was determined from a 200×50-pixel region outside the lungs, which provided reproducible noise measurements regardless of its placement.

The relatively low threshold caused numerous islands of background noise to be retained in the mask. These islands were removed by an 'erosion' operation, which was followed by a 'dilation' operation to restore mask features belonging to ventilated lung, but lost during erosion. Erosion (Θ) of a binary image, *A*, by a smaller structuring element, *B*, is mathematically defined as (85)

$$A \Theta B = \{ z \mid (\mathrm{B})_Z \subseteq A \} \tag{3.1}$$

where $z = (z_1, z_2)$ is the coordinate within the image space and B_Z represents a translation of a symmetric structuring element across the image by one pixel at a time. *B* is chosen to be small compared to the primary image features, but large compared to the spatial scale of the image noise. Erosion of *A* by *B* thus retains the subset of points in *A* upon which the center of *B* can be placed such that all the pixels in *B* overlap only with pixels of value 1. Thus, regions of noise, which are smaller than the structuring element *B*, are removed. Following erosion, dilation ($\oplus$) is subsequently used to restore the size of image *A* using the same structuring element *B* according to (85)

$$A \oplus B = \{ z \mid [(B)_Z \cap A] \subseteq A \} \tag{3.2}$$

If the center of the structuring element falls on top of a pixel with value = 1, the pixel is dilated, meaning that all the neighboring pixels encompassed by the structuring element are replaced by 1.

3.2.5. ADC Calculation

The ADC value of each pixel was calculated from the segmented source images according to

$$ADC = \frac{1}{b}\ln\left(\frac{S_0}{S}\right) \tag{3.3}$$

where S is the signal intensity of the diffusion weighted image pixel, and S_0 is the intensity of the pixel without weighting. The resulting ADC maps were further processed by rejecting any pixels with a value outside the interval $0 \le \text{ADC} \le 0.14$ cm^2/s. The 0.14 cm^2/s cutoff was chosen because it corresponds to the expected free diffusion coefficient of xenon in nitrogen at infinite dilution and 37 °C (86). Finally, since ^{129}Xe diffusion in the visible airways is largely unrestricted (58), the airways were manually segmented out of the maps, such that ADC values for the airways and the distal lung parenchyma were calculated separately.

ADC maps were further analyzed for spatial gradients in the anterior-posterior and superior-inferior direction. ADC gradients in the anterior-posterior direction were calculated by plotting the average ADC for each of the ten slices and calculating the slope. ADC gradients in the superior-inferior direction were calculated by dividing each lung into 3 strips of equal height and using the mean ADC of each region to derive a corresponding slope.

3.2.6. Statistical Analysis

Linear regression analysis was used to test for correlations between ADC and pulmonary function tests, as well as ADC and age, and these were reported using Pearson's correlation coefficient. The mean ADCs of each subject group were tested for statistical significance using the Wilcoxon Rank Sum test. This test was chosen rather than the Student's t-test, because a Bartlett test of our data showed unequal variances between groups. The Wilcoxon test was also used to establish statistical significance of the anterior-posterior and superior-inferior ADC gradients observed in the maps.

3.3. Study Results

3.3.1. Effects of Image Processing

The signal-to-noise ratio (SNR) in ^{129}Xe MRI is generally lower than that achieved for ^{3}He MRI. In this work, the unweighted images had a mean SNR of 15.21 ± 4.74 versus 9.41 ± 2.98 for the weighted images. Therefore, several imaging processing steps were employed to eliminate noise in regions of the image outside the lungs.

Figure 12: Erosion and dilation of binary masks. (A) Non diffusion-weighted (b=0) gas-phase image of a COPD subject with emphysema. (B) The corresponding binary mask. The mask was generated using a threshold obtained using the mean background intensity mean plus twice its standard deviation. (C) Mask from A after erosion using a circular structuring element (radius = 3 pixels), showing that the majority of the background noise has been removed (D) Mask from B after dilation with the same structuring element showing the restoration of subtle image features.

Figure 12A shows a non-diffusion weighted (b=0) image slice, and **Figure 12B** shows the mask obtained using a simple thresholding procedure that retains much of the background noise, which, if propagated, would contribute meaningless values to the ADC maps. When this mask was eroded with a circular structuring element of 3-pixel radius (**Figure 12C),** most of the discontinuous noise was eliminated, but some structural features in the mask were also lost, particularly the major airways. However, as is seen in **Figure 12D,** subsequent dilation restores most of these structural features.

To assist in choosing an appropriately sized structuring element for erosion/dilation, the source images from several representative subjects in the HV, AMC, and COPD groups were also manually segmented to delineate the ventilated lung from the background. The resulting masks were applied to the source images and their ADC maps were calculated, along with the mean ADC and its standard deviation. These maps were then compared with those obtained by automatic segmentation using erosion/dilation with different sized structuring elements. These comparisons showed a circular structuring element with a 3-pixel radius to provide results identical to manual segmentation and, therefore, this element was used to erode/dilate the masks for all subjects. This is illustrated in **Figure 13**. For this example, the mean parenchymal ADC of a healthy subject obtained using a threshold mask without erosion/dilation or further manual segmentation was 0.041±0.026 cm^2/s. By contrast, manual segmentation reduced the mean parenchymal ADC to 0.037 ± 0.021 cm^2/s while erosion/dilation using a 3-pixel radius structuring element generated the same result (ADC = 0.037 ± 0.021 cm^2/s).

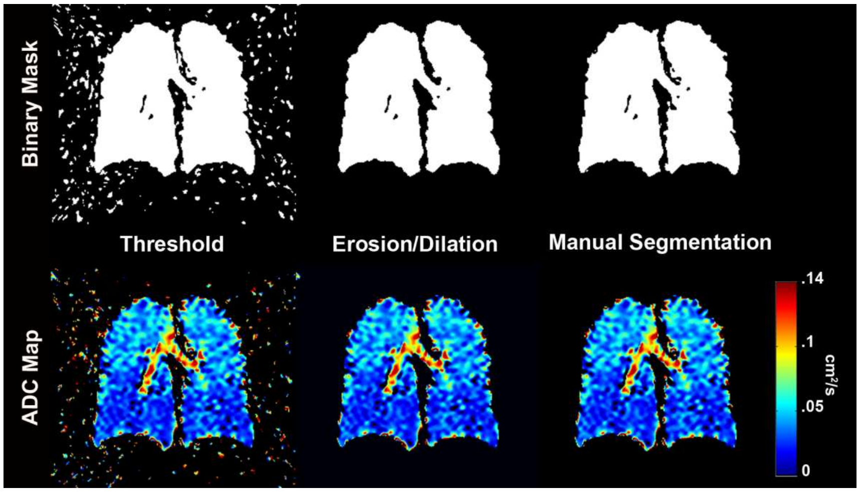

Figure 13: Effect of masking on the ADC map generation. Separate masks were generated for a healthy volunteer using only a threshold, a threshold followed by erosion/dilation, and manual segmentation. The top row shows the masks and the bottom row shows the corresponding ADC map obtained after application of the mask. With a threshold mask, the mean ADC of the healthy subject was 0.041 ± 0.026 cm^2/s.

This mean ADC reduced to 0.037 ± 0.021 cm^2/s with a mask that underwent erosion/dilation with a circular structuring element with a radius of 3-pixels. With a manually segmented mask, the mean ADC was the same as that obtained using erosion/dilation.

3.3.2. ^{129}Xe ADC in the Three Subject Groups

Figure 14 displays representative ADC maps from individuals in each of the three subject groups. **Figure 14A** shows the ADC map from a HV (age = 28 years) with a mean parenchymal ADC of 0.037 ± 0.021 cm^2/s, which is significantly smaller than the self-diffusion coefficient of pure xenon (0.06 cm^2/s) (58), indicating that confinement by the lung microstructure restricts the diffusion of xenon. In this healthy volunteer, the mean ADC in the airways, where ^{129}Xe experiences nearly free diffusion (58), was 0.083 ± 0.029 cm^2/s. This value actually exceeds the self-diffusion coefficient of pure xenon, indicating some degree of dilution with the lighter pulmonary gases such as nitrogen and oxygen occurred. The ADC values in this subject exhibit a narrow distribution, as seen in the corresponding histogram. **Figure 14B** shows the ADC map of an older AMC subject (age = 69 years), with a slightly higher, but still relatively low, mean parenchymal ADC (0.042 ± 0.025 cm^2/s) and a narrow ADC distribution in the histogram. By contrast, **Figure 14C** shows the ADC map of a **Stage II** COPD subject (age = 59 years) with a substantially higher mean (0.068 ± 0.028 cm^2/s), reflecting enlarged airspaces. The ADC measurements for all subjects in this study are summarized in **table 1**.

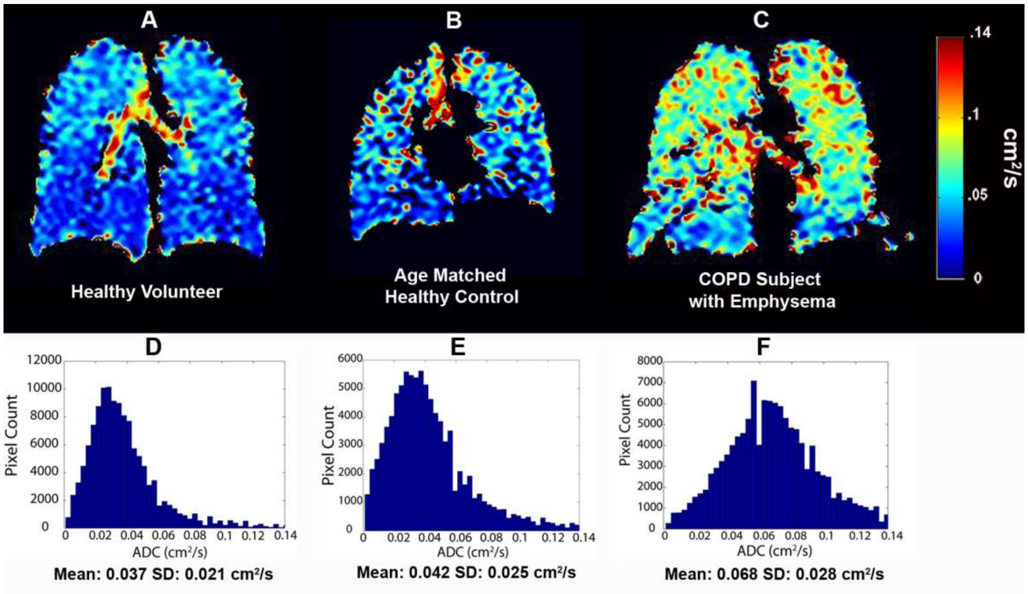

Figure 14: Representative slices from ^{129}Xe ADC maps and corresponding whole-lung ADC histograms. (A) Healthy volunteer (age = 28 years) with a low mean ADC of 0.037 ± 0.021 cm^2/s indicating normal alveolar microstructure. The ADC values in the airways are higher (0.083 ± 0.029 cm^2/s) and reflect nearly free diffusion. (B) Age matched healthy control displaying similarly low parenchymal ADC values (0.042 ± 0.025 cm^2/s). (C) COPD subject with emphysema shows high ADC values (0.068 ± 0.028 cm^2/s) in the parenchyma, indicating alveolar destruction. (D) Whole-lung histogram for the healthy volunteer in panel A showing narrow ADC distribution. (E) Whole-lung histogram for the age-matched control in panel B, exhibits a similarly homogenous distribution. (F) Whole-lung histogram corresponding to the COPD subject with emphysema in panel C, exhibiting a moderately broader distribution.

The mean parenchymal ADC from each of the three subject groups is summarized in **table 2** and graphed in **Figure 15**. As a group, the HVs had a mean ADC of 0.036 ± 0.003 cm^2/s, which is significantly lower than that of the AMC (0.043 ± 0.006 cm^2/s; p = 0.0046), which in turn was significantly lower than that of the COPD subjects

(0.056 ± 0.008 cm^2/s, p = 0.0021). Additionally, the mean ADC of the COPD subjects with emphysema was significantly elevated compared to that of the HV (p = 0.0003). Note that this mean for the COPD group excludes the two COPD patients who had no evidence of emphysema on their CT scans. Indeed, these two subjects showed mean parenchymal ADCs of 0.036 ± 0.021 cm^2/s and 0.039 ± 0.022 cm^2/s, which are below the mean ADC for the AMC and the subjects with emphysema. For all three groups, the mean airway ADC was ~0.08 cm^2/s, and as expected for a gases experiencing nearly free diffusion, there was no significant difference in airway ADC between the three groups.

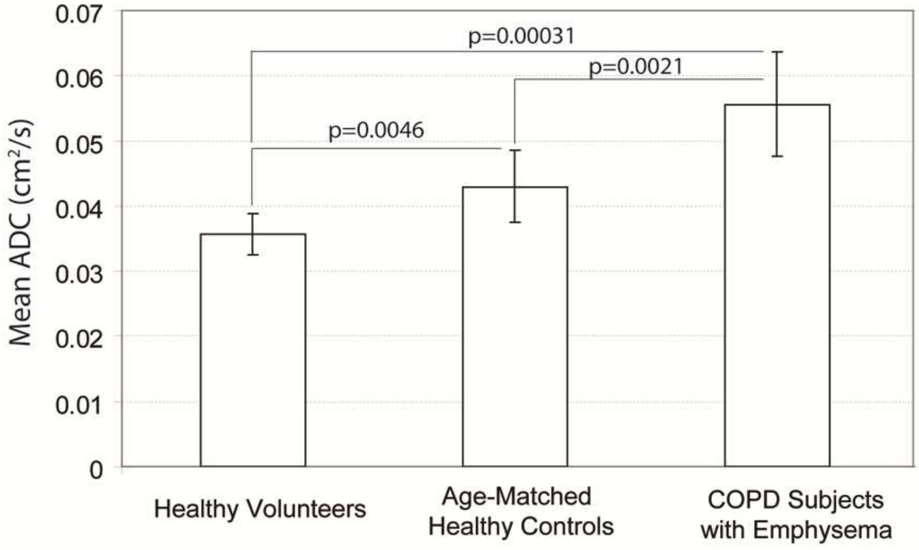

Figure 15: Mean parenchyma ADC values for each subject group. The mean ADC of the COPD subjects with emphysema (0.056 ± 0.008 cm^2/s) was significantly higher than that of the age-matched controls (0.043 ± 0.006 cm^2/s, p = 0.0021), which in turn was significantly higher than that of the healthy volunteers (0.036 ± 0.003 cm^2/s, p = 0.0046).

Table 1: Demographics and experimental values for all subjects.

Sub	Age Years	Sex	Parenchyma ADC cm^2/s		Airway ADC cm^2/s		FEV_1 %Pred	FEV_1/FVC % Pred	DL_{CO}/V_A % Pred
			Mean	SD	Mean	SD			
Healthy Volunteers									
5*	38	M	.035	0.025	0.069	0.032			
7*	32	M	.037	0.019	0.084	0.029			
8*	27	F	0.041	0.021	0.081	0.027			
9*	56	M	0.037	0.019	0.086	0.030			
10*	25	F	0.032	0.020	0.078	0.032			
12	28	F	0.037	0.021	0.083	0.029			
24	24	F	0.032	0.020	0.082	0.031			
Age-matched Controls									
31	64	M	0.053	0.031	0.079	0.032	91	75	62
33	65	F	0.037	0.020	0.074	0.030	107	72	74
36	55	M	0.045	0.029	0.093	0.034	96	79	86
37	66	F	0.033	0.018	0.085	0.030	113	84	96
38	67	M	0.048	0.022	0.087	0.031	83	75	86
43	52	F	0.043	0.025	0.078	0.031	87	79	82
44	69	F	0.042	0.025	0.085	0.030	117	76	75
45	66	F	0.043	0.023	0.083	0.033	99	67	98
46	51	F	0.044	0.027	0.075	0.030	118	74	71
COPD Subjects with Emphysema									
47	74	M	0.044	0.027	0.094	0.031	73	78	100
26	59	M	0.068	0.028	0.078	0.036	57	41	40
29	71	M	0.050	0.024	0.085	0.029	72	65	55
30	73	M	0.065	0.026	0.073	0.025	35	39	37
32	66	M	0.060	0.027	0.078	0.030	64	63	67
39	63	M	0.057	0.028	0.089	0.029	57	49	62
40	53	F	0.049	0.025	0.079	0.033	81	64	45
41	70	M	0.053	0.026	0.073	0.029	54	46	63
42	72	F	0.044	0.025	0.073	0.028	54	52	83
25	63	F	0.036	0.021	0.075	0.028	78	69	76
28	68	M	0.039	0.022	0.093	0.033	79	66	55

*** b = 18.76 s/cm^2 rather than b = 12 s/cm^2 used for all other subjects.**

Table 2: ^{129}Xe ADC distribution within the lungs

	Parenchymal ADC (cm^2/s)	Airway ADC (cm^2/s)	Superior- Inferior Gradient [b] (cm^2/s/cm)	Anterior- Posterior Gradient [b] (cm^2/s/cm)
Healthy Volunteers	0.036 ± 0.003	0.080 ± 0.005	0.00038 ± 0.00013	0.00072 ± 0.00017
Age-Matched Controls	0.043 ± 0.006	0.083 ± 0.006	0.00049 ± 0.00022	0.00065 ± 0.00038
COPD Subjects with Emphysema	0.056 ± 0.008	0.078 ± 0.006	0.00074 ± 0.00033	0.00003 ± 0.00047

[a] Values are population mean ± standard deviation.

[b] Major airways were excluded when determining ADC gradients.

3.3.3. ADC Gradients and Correlations

Each of the subjects depicted in **Figure 14** exhibit noticeable gradients in the ADC values with higher ADC observed in the apex relative to the base of the lungs. These superior-inferior gradients are well illustrated in the full ADC maps of a healthy volunteer depicted in **Figure 16**. These gradients, which produced a ~24% higher ADC in the apex relative to the base for the two healthy groups ($p = 0.00018$, HV; $p = 3.45\text{x}10^{-5}$, AMC), are consistent with those observed for all the groups as shown in **Figure 17A**. The superior-inferior gradient was larger ($p = 0.024$) for the COPD subjects with emphysema (0.00074 ± 0.00033 cm^2/s/cm) than for the AMCs (0.00049 ± 0.00022 cm^2/s/cm), which in turn was larger, though not significantly larger ($p = 0.09$), than the HVs

(0.00038 ± 0.00013 cm²/s/cm). The strong superior-inferior ADC gradient in the COPD subjects is indicative of greater smoking-induced tissue destruction in the upper lobes of the lung, which has also been reported in the CT (87), pathology (88), and ^{3}He MRI literature (29).

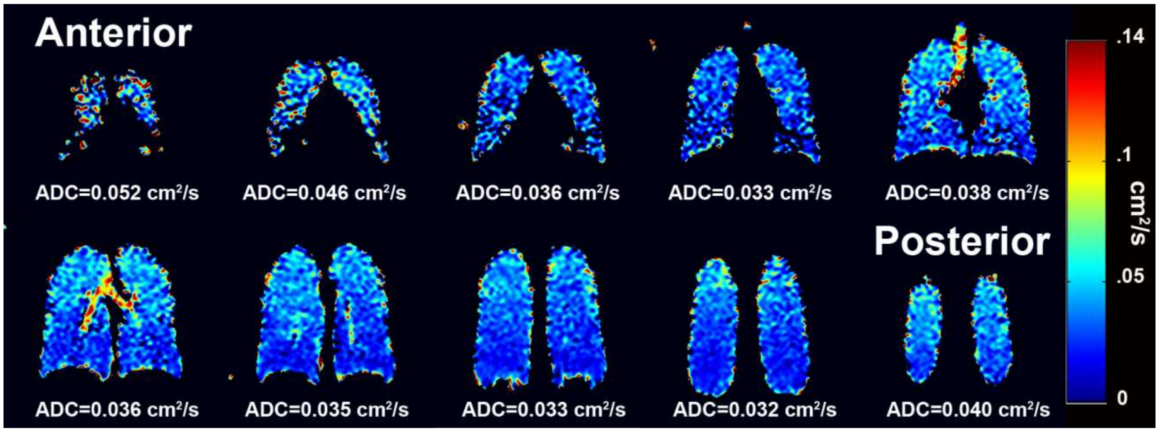

Figure 16: A complete ADC map for a healthy volunteer. The map shows clear ADC gradients in both the superior-inferior and anterior-posterior directions.

Figure 16 also shows a clear trend towards higher ADC values in the more anterior image slices. Such anterior-posterior ADC gradients are clearly present in both of the healthy groups, but this gradient was negligible in the COPD subjects with emphysema. As illustrated in **Figure 17B**, the average anterior-posterior ADC gradients for the HVs were 0.00072 ± 0.00017 cm²/s/cm and 0.00065 ± 0.00038 cm²/s/cm for the AMCs, but were nearly absent (0.00003 ± 0.00047 cm²/s/cm) for the COPD subjects with emphysema.

This difference was statistically significant relative to both the HV group (p = 0.014) and the AMC group (p = 0.0085).

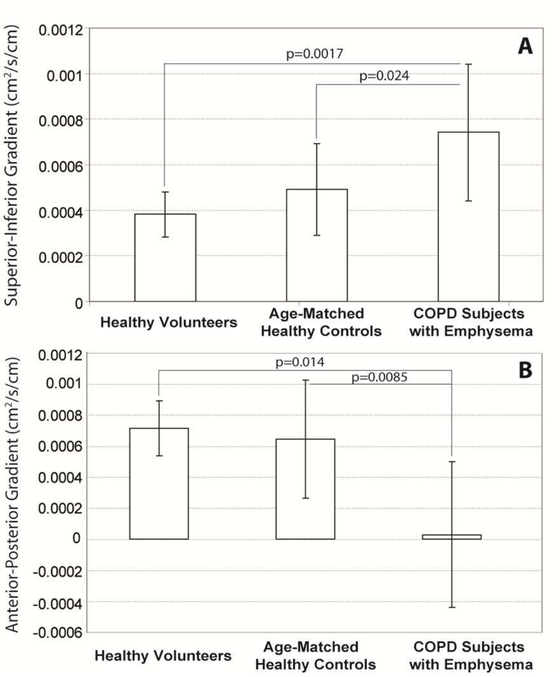

Figure 17: ADC gradients. (A) Mean ADC gradients in the superior-inferior direction. This gradient was significantly larger in the COPD subjects with emphysema (0.00074 cm^2/s/cm) than in the age matched healthy controls (0.00049 cm^2/s/cm, p = 0.024), and was also larger than that of the healthy volunteers (0.00038 cm^2/s/cm, p = 0.0017). There was no significant difference between the superior-inferior gradients observed in the two groups of healthy subjects (p = 0.09). (B) Mean ADC gradients in the anterior-posterior direction. The mean ADC gradient from the COPD subjects with emphysema (3.05×10^{-5} cm^2/s/cm) is significantly smaller than that of either the healthy volunteers (0.00072 cm^2/s/cm, p = 0.014) or the age matched healthy controls (0.00065 cm^2/s/cm, p = 0.0085). The ADC gradients from the two groups of two healthy subjects were not significantly different (p = 0.81) from one another.

For the COPD and AMC subjects, the mean parenchymal ADC was correlated with three pulmonary function metrics — DL_{CO}/V_A, FEV_1, and FEV_1/FVC. As illustrated in **Figure 18A-C**, the mean parenchyma ADC was moderately, yet significantly, correlated with all three metrics (FEV_1 and DL_{CO}/V_A expressed as percent predicted values). The mean parenchyma ADC also significantly correlated with the absolute DL_{CO}/V_A (mL/mHg/min/L) values ($r = -0.77$, $p = 0.0002$) but not with the absolute FEV_1. As shown in **Figure 18D**, the mean ADC for the HVs and AMCs also increased with age ($r = 0.56$, $p = 0.02$), with a slope of 0.0002 cm^2/s per year.

3.4. Inferences about ^{129}Xe ADC MRI

Diffusion-weighted MRI using HP ^{129}Xe poses numerous challenges compared to using ^3He. The nearly three-fold lower gyromagnetic ratio (γ) of ^{129}Xe and lower polarization achieved in our setting contributed to the low image SNR. Moreover, the lower diffusivity of ^{129}Xe relative to ^3He requires that a larger b-value be applied to achieve sufficient weighting to derive meaningful ADC calculations. Because the b-value also scales with γ^2 (60)], sufficiently large b-values could only be attained using relatively long diffusion weighting pulses. For this study, the 2.4 ms pulse durations required, resulted in minimum echo times of 8.3 ms, which contributes unwanted T_2*-weighting. These factors combined to create a significant SNR challenge and led us to introduce several processing steps to calculate ^{129}Xe ADC values only for pixels belonging to ventilated lung. This involved first creating a rough lung mask by applying a relatively low threshold, and refining the mask using erosion/dilation to remove residual background noise. This approach gave similar ADC results as when masks were generated by manual segmentation and have the advantage of being objective and fast. However, a disadvantage of the erosion/dilation technique is that it could erroneously remove isolated areas of ventilation smaller than the structuring element. Of course, the need for image processing would be substantially reduced by improving the relatively modest ^{129}Xe polarization (5-10%) available in this study. Considering that liter-quantities of HP ^{129}Xe with polarizations approaching 50% have recently been demonstrated (89), achieving better ADC map fidelity through improved image SNR appears promising.

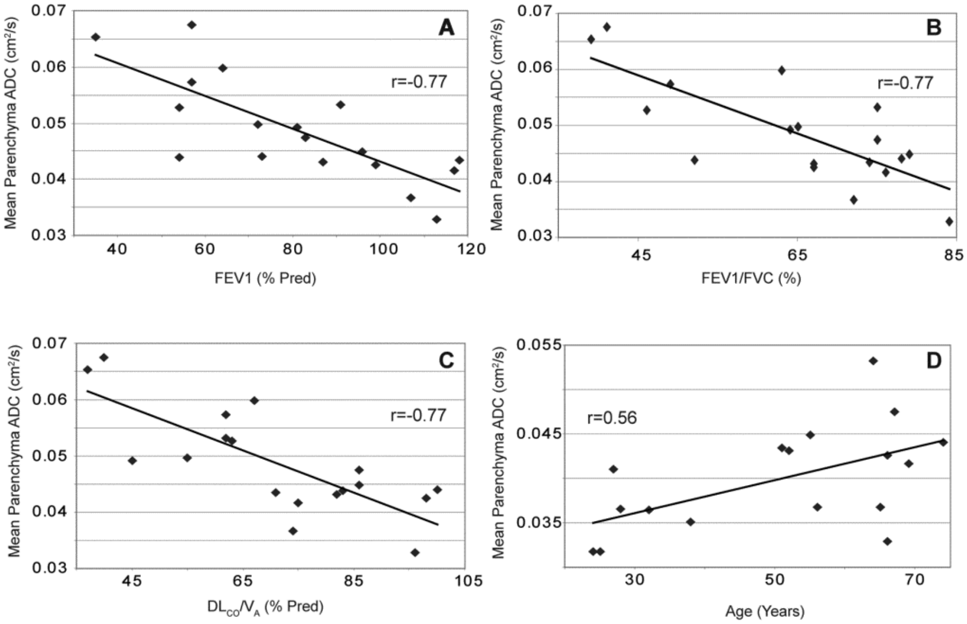

Figure 18: Correlation of mean parenchymal ADC with pulmonary function metrics and age. (A) Correlation with percentage of predicted FEV$_1$. r = –0.77, p = 0.0002. (B) Correlation with percentage of predicted FEV$_1$/FVC. r = -0.78, p = 0.0002. (C) Correlation with percentage of predicted DL$_{CO}$/V$_A$. r = –0.77, p = 0.0002. (D) Correlation with age (healthy subjects only). r = 0.56, p = 0.02.

Besides lower SNR, ^{129}Xe differs from ^{3}He in that xenon diffuses into the capillary blood-stream (43)], which could decrease ^{129}Xe concentration during imaging. Assuming an initial alveolar xenon concentration of 20% after inhalation, its solubility of ~15% in the blood, combined with a cardiac output of ~80 ml/sec would reduce the alveolar concentration to about 19.2% during a 16 second breath-hold. This change in concentration is expected to increase the xenon self-diffusion coefficient by only 0.9%. Given that any difference in diffusion will be further reduced by confinement, the influence of xenon solubility on the ADC is expected to be negligible.

The mean parenchymal ^{129}Xe ADC values of 0.036 cm^2/s for HVs agrees well with the preliminary values of 0.039 and 0.036 cm^2/s reported by Mugler *et al.* (82) and 0.04 cm^2/s reported by Sindile *et al*. (83). Even with this relatively small sample of 17 healthy subjects (7 HVs and 10 AMCs), ^{129}Xe ADC shows an increase with age. The age-related change can be compared to the annual ^{3}He ADC change of 0.0015 cm^2/s/yr reported by Fain *et al*. (34) by considering the predicted ADC for a single subject age. The predicted ^{3}He ADC at for a healthy subject at age 25 is 0.1875 cm^2/s, which gives a ^{3}He ADC slope of 0.8% per year. From our data, the predicted 129Xe ADC at age 25 is 0.0363 cm^2/s, giving a ^{129}Xe ADC slope of 0.6% per year. Moreover, the mean ^{129}Xe ADC correlates relatively well with pulmonary function testing, which is again similar to the trend seen for the ^{3}He ADC (29). The correlation of ^{129}Xe ADC with FEV$_1$/FVC (r = -0.78) is slightly weaker than that reported for ^{3}He ADC [r = -0.97, (29)]. Additionally, the standard deviation of the ^{129}Xe ADC did not correlate well with pulmonary function metrics, whereas such correlations have been reported for ^{3}He ADC (30). This difference may be attributable to the substantial superior-inferior ADC gradients seen with ^{129}Xe, which broadens the ADC distribution even in the absence of disease.

Although the mean ADC metric was effective in separating the three subject groups in aggregate, there was some overlap between the subjects with emphysema and the healthy volunteers. These deviations could result from different degrees of ^{129}Xe dilution into lung volumes (discussed below). However, similarly overlapping mean ADC data have been reported in asymptomatic smokers (76) and emphysema patients (29,90) in the ^{3}He MRI literature, suggesting that natural individual-to-individual variations in lung microstructure could also play a role.

The ADC gradients seen in the anterior-posterior direction in healthy subjects are attributable to gravity-dependent compression of the lung airspaces (91). Compression in the dependent lung is caused by the weight of the lung itself (91), with additional contributions from the weight of the heart (92). Thus, in the healthy lung smaller ADC values (smaller alveolar size) are expected in the dependent lung compared to the non-dependent lung. This observed trend is similar to that reported by Fichele *et al*. using ^{3}He ADC (51). However, the near absence of anterior-posterior ADC gradients in the COPD subjects with emphysema may suggest that the heterogeneity of emphysematous tissue destruction could negate the influence of gravity. The reduction of the anterior-posterior gradient has also been attributed to a decrease in the compressibility of the lung tissue due to COPD (33). A similarly small anterior-posterior gradient was seen by Diaz *et al*., using ^{3}He ADC (80). The superior-inferior gradient we observed in the HVs and AMCs corresponded to an average ADC reduction of 23.5%, which is significantly smaller ($p = 0.00018$, HV; $p=3.45\times10^{-5}$, AMC) than the 28.1% observed in the COPD subjects with emphysema, but still quite substantial.

The higher ^{129}Xe ADC observed in the superior lung may result from ^{129}Xe dilution effects. This conclusion is driven by reports suggesting that supine subjects exhibit a larger functional residual capacity (FRC) in the superior lung relative to the inferior lung (93). This greater residual volume will more fully dilute the inhaled ^{129}Xe in the superior lung, thereby producing larger xenon diffusion constants in this region. This superior-inferior gradient, which we note is the opposite of that reported by Sindile *et al*. (83), cautions that ^{129}Xe ADC, while sensitive to microstructure, is also affected by ^{129}Xe dilution in lighter alveolar gases. ^{129}Xe dilution could lead to erroneously high ADC values in regions of air trapping, which would admit very little xenon per breath. Such regions of high dilution could potentially be identified as those with very low SNR on the $b = 0$ images. Alternatively, the effect of ^{129}Xe dilution on ^{129}Xe ADC could provide a novel means to quantify regional fractional ventilation.

This study did have several limitations that could affect the precision of the results. First, the need for simplified logistics in this first clinical trial required that the inhaled ^{129}Xe volume remain fixed at 1 liter for all subjects regardless of their total lung capacity. Hence, subjects with smaller resting lung volumes would experience more alveolar expansion, perhaps slightly elevating the resulting ^{129}Xe ADC (90). However, smaller residual volumes of alveolar gas will result in less dilution of the inhaled ^{129}Xe, which will have the opposite effect on the ADC. Further work, in which inhaled volume is adjusted to the subject total lung capacity (TLC) (92), will be required to fully elucidate the interplay of these two effects. Also, the starting lung volume for subjects was only loosely controlled to lie between RV and FRC. Better control of initial lung volume, would likely improve reproducibility, particularly of the ADC gradients, which may be eliminated when lung volumes reach closer to TLC (94). Similarly future ^{129}Xe studies will use a consistent b-value for all subjects, rather than the two that were used here. Hence, while this small trial had certain limitations, and does not definitively cement the diagnostic utility of ^{129}Xe ADC, the preliminary results are encouraging.

This work showed that despite the lower gyromagnetic ratio, polarization, and free-diffusion of ^{129}Xe relative to ^{3}He, hyperpolarized ^{129}Xe ADC maps can be obtained in human subjects in a clinically feasible manner. The associated lower SNR of ^{129}Xe images requires careful segmentation of the lung from background noise, which we have accomplished using a thresholded mask in conjunction with erosion/dilation operations. The resulting ^{129}Xe ADC maps exhibit sufficient dynamic range to distinguish subjects with emphysema from age-matched control subjects, and younger healthy subjects. The mean ADC exhibits a moderate, yet significant correlation with pulmonary function tests, similar to what has been reported for ^{3}He ADC. Moreover, the ^{129}Xe ADC is sufficiently sensitive to reveal its dependence on changes in pulmonary microstructure due to subject age.

3.5. Summary

Taken together, the results reported in this work indicate that ^{129}Xe holds promise for replacing the scarcely available ^{3}He for generating pulmonary ADC measurements. ^{129}Xe ADC holds promise for the detection and characterization of early emphysematous changes in the lung. In conjunction with ventilation analysis (31) and the *dissolved-phase images* to be discussed in the next chapter, diffusion-weighted imaging could serve as a means to non-invasively phenotype and monitor the treatment of subjects with COPD.

4. Development of Simultaneous Gas and Dissolved-phase ^{129}Xe MRI

4.1. Motivation

HP ^{129}Xe exhibits physical and MR properties that make it almost ideally suited for probing gas-exchange. Inhaled ^{129}Xe is moderately soluble in the pulmonary tissues and capillary blood, and when ^{129}Xe is in either compartment, its magnetic-resonance detection frequency exhibits a dramatic chemical-shift, which allows for its discrete and separate detection from gaseous ^{129}Xe in the air spaces. These two resonances constitute the "dissolved-phase" of ^{129}Xe. This is graphically depicted in **figure 19A**, and **figure 19B** shows a typical gas-transfer spectrum in a healthy volunteer. As the pathway taken by ^{129}Xe to reach the capillary blood stream is identical to that of oxygen, imaging this dissolved-phase as a single entity, to first order, depicts the regional distribution of gas-exchange and is crucial to understanding the functioning of the lung.

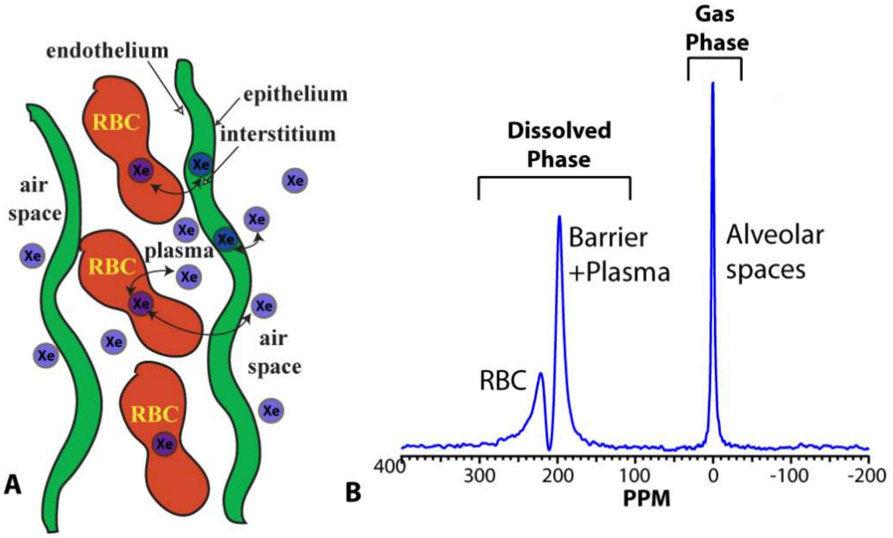

Figure 19: (A) Schematic showing the presence of ^{129}Xe in the air-spaces, plasma and the red-blood cells. The arrows indicate that ^{129}Xe is in constant exchange with the different compartments. (B) A typical ^{129}Xe spectrum in the lung, showing the three resonances corresponding to ^{129}Xe in the air-spaces (0 ppm), barrier and plasma tissue (197 ppm) and the red-blood cells (217 ppm).

Given the low signal-intensity of the dissolved-phase (~2% of the gas-phase), the initial efforts to image this dissolved-phase used an indirect approach. One such approach was the xenon transfer contrast (XTC), which took advantage of the exchange dynamics between the dissolved and gas-phase xenon resonances (95). As the resonances of xenon are in continuous exchange, pulsing on the dissolved-phase will cause a mild depolarization of the gas-phase magnetization, and this depolarization was used to map the dissolved-phase distribution. This technique was a good first step to mapping this dissolved distribution, and was also extended to 3D (45). However, this technique is complicated by the need for large saturation pulses and a multi-breath acquisition to correct for T_1 decay, both of which limit its widespread acceptance as a clinical tool to study gas-exchange (45). The most important shortcoming of this approach is its inability to create separate images of the components of the dissolved-phase – ^{129}Xe in the barrier, and ^{129}Xe in the RBCs. As mentioned in **chapter 1**, creating an independent image of ^{129}Xe in the RBCs will provide a truly fundamental image of gas-exchange in the lung. Attempting to create such an image using XTC would require a highly selective excitation of the either the RBC or the barrier resonance, which is not feasible, and hence this technique is limited to studying the dissolved-phase as a single entity. These drawbacks led our group to drive the transition to imaging the dissolved-phase directly, the feasibility of which was first demonstrated in the preclinical arena (47), and more recently, direct dissolved-phase imaging was translated to the clinic (43). The direct approach to imaging the dissolved-phase takes us a step closer towards creating independent images of ^{129}Xe in the barrier and the RBCs.

At the start of this thesis work, our group had just shown the ability to image the dissolved-phase directly, in a single breath-hold (43). Importantly, we observed that these initial dissolved-phase ^{129}Xe images exhibited a strong gravitational gradient that reversed when subjects were imaged prone vs. supine (96). Moreover, these images also hinted at significant heterogeneity within a given gravitational plane. However, confirming and quantifying these observations required overcoming a several shortcomings. a) *The imaging approach was not yet proven to be reliable and reproducible*. b) *As the gas-phase is the source magnetization for the dissolved-phase distribution, quantifying the dissolved-phase distribution will require also acquiring an image of the gas-phase in the same breath-hold.* Single-breath gas and dissolved-phase images were first acquired by Mugler *et al.* (46) who exploited the chemical shift artifact using a Cartesian GRE sequence to acquire both the gas and dissolved-phase images within the same field of view. However, because of the longer TEs needed with the GRE sequence, overcoming the short dissolved-phase T_2* (~2ms) and acquiring good images using this approach required very high polarizations of ^{129}Xe (~40%). Again, the fundamental flaw in this approach is the inability to create separate images of the xenon in the barrier and the RBCs. Nonetheless, this work provided important initial confirmation of our observation that dissolved ^{129}Xe images exhibit significant gravitational gradients, and further provided a valuable framework for quantifying the gas-exchange distribution.

Alternatively, we hypothesized that a 3D radial pulse sequence is more ideally suited to image both the gas and dissolved-phase in a single breath. By sampling the free induction decay (FID), this sequence can generate sub-millisecond ‘echo’ times that helps us overcome the short dissolved-phase T_2*. More importantly, this sequence, in conjunction with a number of algorithms from the proton literature, was felt to lend itself best to create separate images of the ^{129}Xe in the barrier and the RBCs. However, the clinical implementation of this sequence to image the gas and dissolved-phase in a single-breath would require overcoming a few challenges – a) *Unlike the approach of Mugler et al., which pulsed on both gas and the dissolved-phase distributions, this radial acquisition would require the selective excitation of the dissolved-phase.* b) *To image both the gas and dissolved-phase, we need twice the number of RF pulses. As the HP signal is depleted with the application of an RF pulse, the flip-angles should be carefully chosen to minimize the decay of the longitudinal magnetization*. This chapter will focus on overcoming these challenges that hindered the development and subsequent clinical translation of a single-breath gas and dissolved-phase imaging approach using a 3D radial pulse sequence.

4.2. Improving the reliability of dissolved-phase imaging

While the initial demonstration that dissolved-phase imaging could be achieved in a single breath-hold was important, there were technical hurdles to overcome to ensure the technique is established on a reliable and reproducible footing. The quality of dissolved-phase images was unpredictable and seemed to vary drastically with each subject scanned. One such example is seen in **figure 20,** which shows the dissolved-phase images acquired with similar parameters in two subjects, but one severely contaminated with artifacts. Hence, it was really important to understand the underlying factors that control dissolved-phase image quality.

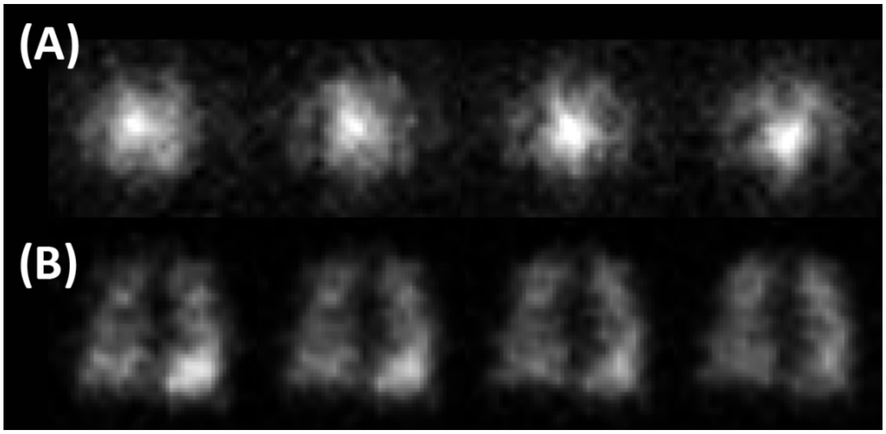

Figure 20: Dissolved-phase images acquired in two subjects with the same imaging parameters. The subject shown in (A) exhibited severely compromised image quality, while for the subject in (B), the dissolved-phase image was normal.

While the image quality is impacted by the choice in imaging parameters (flip-angle, TE, TR, receiver bandwidth), polarization, or subtle changes in the reconstruction parameters, one issue was suspected to be primarily responsible for good image quality – selective excitation of the dissolved-phase resonances. Dissolved-phase imaging requires a sufficiently short, yet highly selective RF pulse to avoid exciting the 50-fold larger gas-phase resonance to avoid generating significant artifacts in the images. To provide some background, **figure 21** shows the expected pulse profile of a Hamming-apodized 3-lobed sinc pulse, which is currently being used for RF excitation of the dissolved-phase of xenon. The bandwidth (BW) of the resulting rect-like frequency profile is dictated by the length of the RF pulse, $BW = \frac{1}{t_0}$ where t_0 is time to the first zero crossing of the sinc pulse.

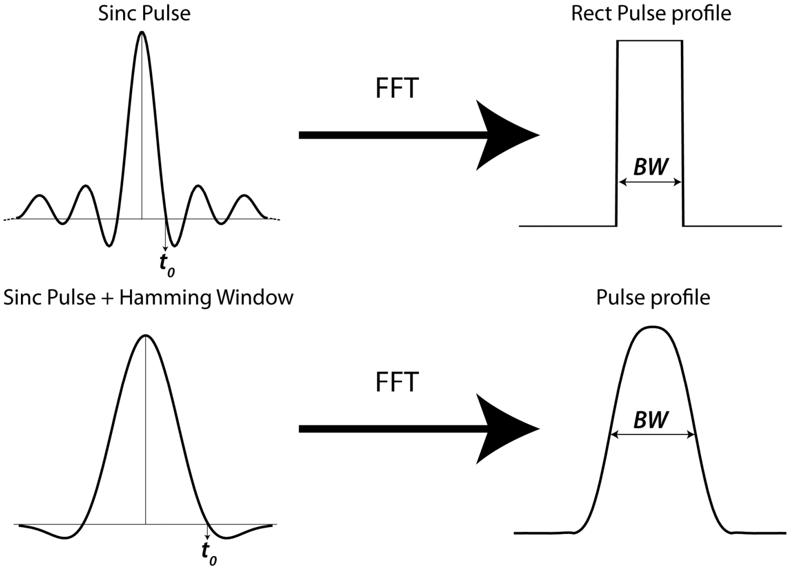

Figure 21: Idealized RF frequency profiles. An infinitely long sinc pulse would give an ideal, rect frequency profile. The RF pulses used clinically, are truncated and apodized. A three-lobe, apodized sinc pulse would give a slightly broadened, smoother frequency profile.

Traditionally, dissolved-phase imaging has employed a 1200-μs 3-lobed sinc pulse. The resulting RF frequency profile would have a bandwidth of ~3400 Hz. This bandwidth is sufficiently narrow to avoid exciting the gas-phase resonance, which on a 1.5T system, is ~3800 Hz from the dissolved-phase. However, as the dissolved-phase is only 2% of that in the gas-phase, even if 2% of the RF power intended for the dissolved-phase were to be applied on the gas-phase, this would lead to equal contributions to the free induction decay (FID) from both gas and dissolved-phases. Even such a minimal, unintentional excitation would lead to significant artifacts in the dissolved-phase image, as seen in **figure 20A**.

To investigate this theory further, we undertook a careful review of prior dissolved-phase spectra that were acquired with the same RF pulse used for imaging. While these spectra should reveal only the RBC and barrier resonance, they instead contained varying amounts of gas-phase signal. It was noticed that this off-resonance excitation of the gas-phase varied based on the amount of applied RF power. This RF power is controlled using the amplitude of the RF pulse set using the pulse sequence, or the transmit gain (TG, in dB). As an example, **figure 22** shows two dissolved-phase spectra acquired in different subjects, but with the same pulse length and the same effective RF power. The spectrum seen in **figure 22A** was acquired with low RF amplitude, and a high TG, and we see minimal excitation of the gas-phase resonance. In contrast, **figure 22B** was acquired with a larger RF amplitude, and a lower TG, and shows a significantly larger gas-phase excitation.

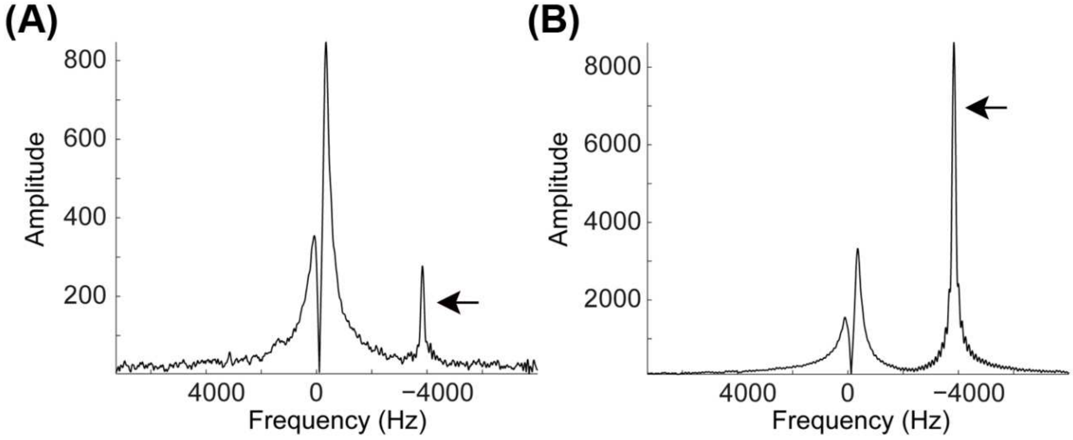

Figure 22: Variable off-resonance gas-phase excitation. (A) Shows a magnitude dissolved-phase spectrum acquired with a low RF amplitude and high TG, resulting in minimal off-resonance gas-phase excitation (B) A similar spectrum was acquired with the same pulse length, with a higher RF amplitude and lower TG, which yielded significantly larger gas-phase excitation.

These results show that the off-resonance excitation is variable and depends on the amplitude of the RF pulse, and the transmit gain – both of which decide the applied flip-angle. Gaining further insight into this off-resonance excitation and studying the impact of these parameters will require measuring the actual frequency profile of the RF pulse.

4.2.1. RF Frequency Profile Mapping

It was hypothesized that the main reason for the off-resonance excitation of the gas-phase could be a distortion of the frequency profile of the RF pulse. Also, with the results seen in **figure 22**, the choice of flip-angle and transmit gain could distort the frequency profile differently. If distorted, this profile could retain RF power at much higher frequencies than theoretically estimated, which will result in unintentional excitation of the gas-phase resonance.

In order to confirm this hypothesis, a pulse sequence was developed to map the frequency profile of the RF pulse. Because of its higher thermal signal, as a surrogate for xenon, the experiments were carried out using a sodium phantom and a surface coil. With the gradients turned off, both transmit and receive frequencies in the sequence were dynamically changed to cover a specified bandwidth (BW) about the main sodium resonance (f_s). At each frequency, a sodium spectrum was acquired. The amplitude of these spectra would then be an indicator of the power deposited at that frequency. By then plotting the peaks of the individual sodium spectra as a function of the transmit and receive frequency, we can measure the frequency profile of the RF pulse. This process is graphically explained in **figure 23A-B**. **Figure 23C** shows the frequency profile of the 1200-μs sinc pulse, which shows a dip in the pass-band and the prominent side lobes in the profile as indicated by the arrows. At a field strength of 1.5T, these prominent side-lobes appear at a frequency that is ~200 Hz from the gas-phase resonance, and hence will cause its significant off-resonance excitation. Surprisingly, similar results have been reported by Chan *et al.* (97), who also noticed a warping of the RF frequency profile used for slice selection and this was attributed to the non-linearity of the RF amplifier. Hence, one can conclude that this RF distortion induced by the non-linear amplifier causes the off-resonance excitation of the gas-phase, and understanding its behavior will have a significant impact on dissolved-phase imaging.

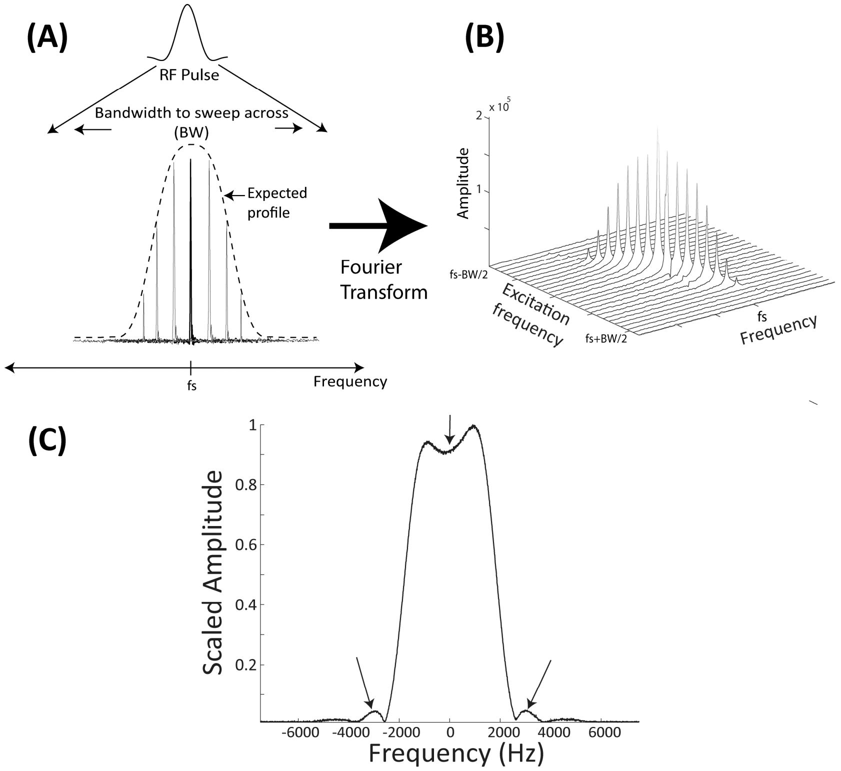

Figure 23: (A) graphically illustrates the method used to map the frequency profile of an RF pulse. Multiple spectra of the sodium phantom were acquired using a sinc pulse while sweeping across a range of frequencies (BW) around the main resonance. The peaks of the resulting spectra shown in (B) were used to plot the frequency profile of the pulse (C).

With this tool to map the frequency profile, we were ideally poised to understand the impact that RF amplitude and TG have on the frequency profile. Frequency profiles using a sodium phantom were first acquired with a constant RF amplitude (scaled to the maximum) and with a varying TG. As shown in **figure 24A**, the frequency profile was warped irrespective of the TG, and as the RF amplitude was increased, the frequency profile became progressively worse. **Figure 24B** shows the frequency profiles acquired with a constant TG (150 dB) while the RF amplitude was increased (11 – 100% of maximum). Surprisingly, the frequency profile acquired with low RF amplitude (11%, blue profile) at this high TG, was free of any distortion. However, an increase in RF power brought on by the higher RF amplitudes warped the frequency profile. Hence, based on these results, an increase in RF power brought on by RF amplitude or TG, are not equivalent. Also, it would be preferable to operate at high TGs and a low RF amplitude as the warping introduced in this regime was lower. Based on these results, one can speculate that the distortion is introduced by two stages. The first may be introduced by the *mixer* that feeds into the exciter board to generate a modulated RF waveform. The second stage of distortion would be introduced by the RF amplifier, which is known to have a non-linear gain response (97). Furthermore, these results seem to explain the pattern of off-resonance excitation seen in **figure 22**.

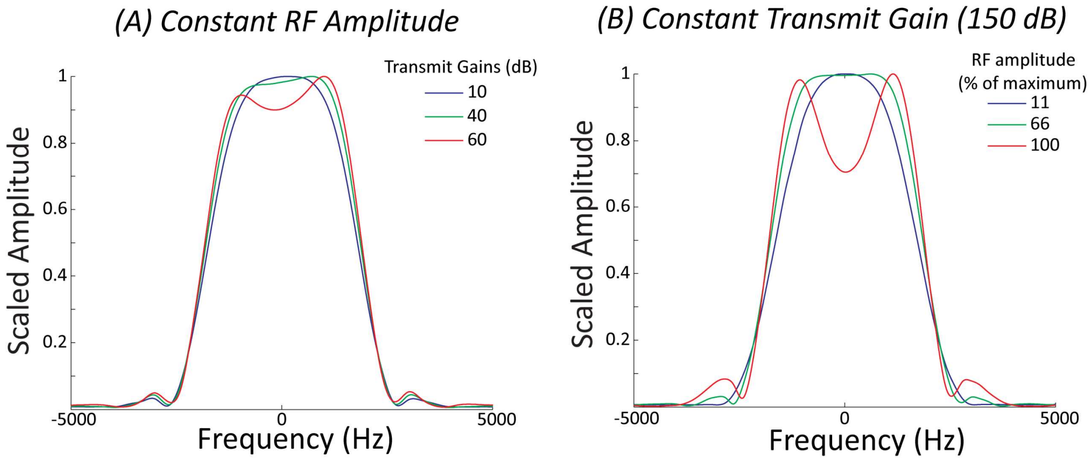

Figure 24: B-spline smoothed RF frequency profiles for an apodized 3-lobed 1200-μs sinc pulse. The frequency profiles have been measured as a function of transmit gains (A) and RF amplitudes (B). As shown in (A), low gains and high RF amplitudes seem to introduce prominent side lobes, whereas high gains and a low RF amplitude shown in (B) produce a cleaner RF frequency profile.

4.2.2. Characterizing Off-resonance Gas-phase Excitation

The previous section showed that the off-resonance excitation was caused by warped RF pulse which was potentially caused by the mixer and the non-linear RF amplifier. Based on the warping introduced by these two stages, it was expected that higher RF powers would cause larger off-resonance excitation of the gas-phase of ^{129}Xe. Conversely, in the dissolved-phase spectra acquired at higher RF powers (RF amplitude was increased at a constant TG), it was noticed that the amplitude of the off-resonance gas-phase signal dropped.

The off-resonance excitation pattern as a function of RF power was empirically characterized. The goal of this experiment was to determine a pulse-length that would be short enough to overcome the short dissolved-phase T_2*, and the associated transmit power that would minimize off-resonance gas-phase excitation, thus giving us a pulse that is ideal for dissolved-phase imaging. This characterization was performed on a 1.5T GE clinical scanner, using the ^{129}Xe vest coil, which was wrapped around a loading shell that contained and an ALTEF bag with 1-L of HP ^{129}Xe (natural abundance). Transmit and receive frequencies were placed +3.832 Hz above the gas-phase resonance frequency, to simulate dissolved-phase excitation. As the bag of gas would not have a dissolved-phase resonance, any signal seen would be a measure of off-resonance gas-phase excitation, and hence, RF pulse imperfection. Sinc pulses of pulse lengths 1–1.5 ms were used to acquire multiple spectra over a specified range of applied flip-angles (1-35°) which corresponded to RF powers of 7.5-264 W. This is illustrated in **figure 25A**. As shown in **figure 25B**, for pulse lengths shorter than 1.2 ms, the off-resonance excitation increased with an increase in power, and dropped minimally at higher powers. However, for the 1.2-ms sinc pulse, there exists a narrow band of powers where the off-resonance excitation was greatly minimized. The minima for this narrow band occurred at a power of 106 W. At higher pulse-lengths, this narrow band shifted to a lower power. Although the off-resonance excitation was lower for the 1.4-ms pulse, 1.2-ms was considered ideal, as it provided the perfect balance between the high-selectivity needed to excite just the dissolved-phase and was short enough to overcome the short T_2* of the dissolved-phase (~2 ms). With this information in hand, it is now clear that the dissolved-phase image with significant artifacts shown in **figure 20A** was acquired at an RF power that corresponded to a flip-angle of 10°, which as shown in **figure 25B**, would have extensive excitation of the gas-phase. This empirically characterized pulse length and power was used for all subsequent dissolved-phase imaging.

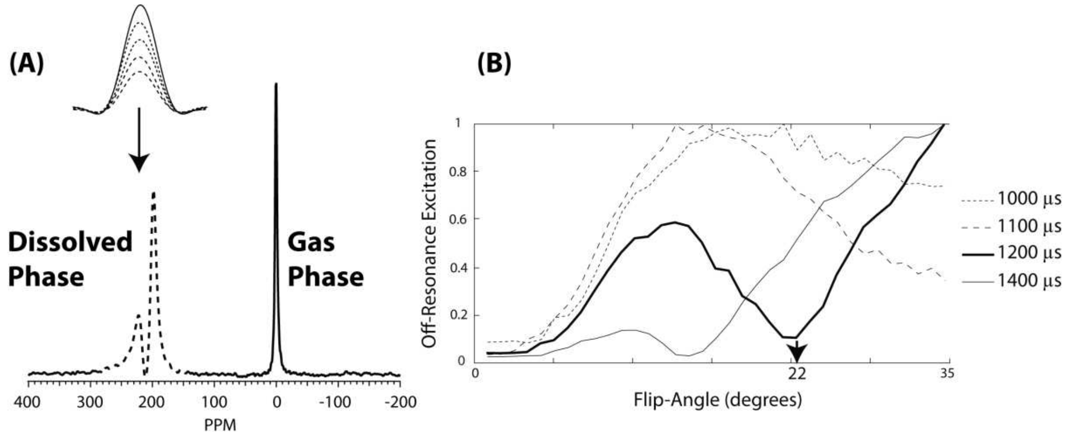

Figure 25: (A) Schematic showing the characterization of off-resonance excitation. To model dissolved-phase excitation using a bag of polarized xenon, 3-lobed sinc pulses of varying amplitudes were used to pulse 3.8 kHz above the gas-phase resonance. (B) Gas-phase signal intensities for various pulse lengths as a function of RF power. The 1.2-ms sinc pulse reduced the gas-phase excitation for a narrow band of RF powers.

To test the validity of this finding in-vivo, this experiment was repeated in 3 healthy volunteers, and the results matched the phantom experiments by showing a reduced gas-phase excitation at a flip-angle of 22°. **Figure 26A** shows just the gas-phase signal (off-resonance) of a dissolved-phase spectrum as a function of flip-angle for a 1.2-ms sinc pulse. As shown, there was reduced off-resonance excitation at an RF power of 106 W, which corresponded to a flip-angle of 22° (**figure 26B)**. Based on these results, dissolved-phase imaging was carried out with a 1.2-ms sinc pulse and an RF power of 106 W.

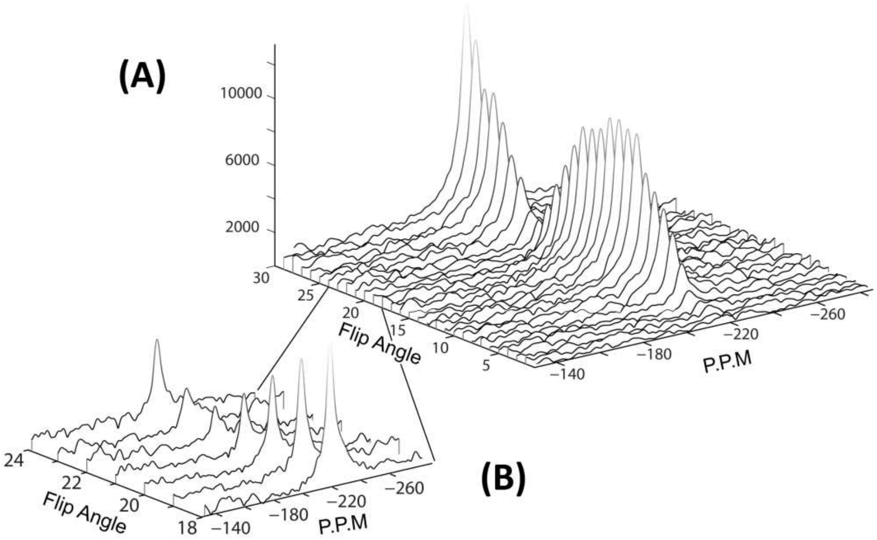

Figure 26: In-vivo confirmation of the variable off-resonance excitation pattern. (A) Spectra acquired in a human subject shown as a waterfall plot of only the gas-phase off-resonance signal for a 1.2-ms sinc pulse, as a function of flip-angle. This off-resonance excitation reached a minimum at a flip-angle of 22°, which is also shown in (B).

4.3. Radial Pulse Sequence

An interleaved radial sequence was written to acquire single-breath images of the gas and dissolved-phase (**figure 27).** The acquisition began with both transmit and receive frequencies centered on the gas-phase resonance. Once a ray of k-space was acquired, transmit and receive frequencies were changed to that of the dissolved-phase resonance (+217 ppm), and after increasing the flip-angle to an appropriately higher value, the same ray of k-space was acquired again. This process was repeated until all of k-space was sampled using an Archimedean spiral sampling strategy.

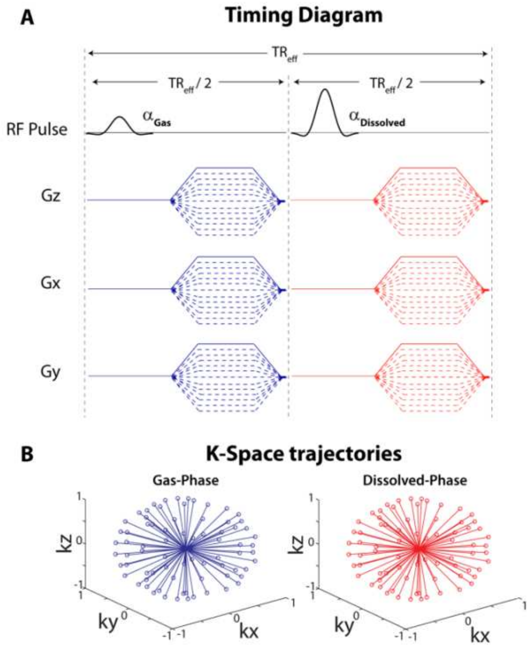

Figure 27: (A) The interleaved 3D radial pulse sequence. The sequence began by pulsing on the gas-phase resonance with a small flip-angle, acquiring a ray of k-space. Transmit and receive frequencies were then changed to pulse on the dissolved-

phase with a larger flip-angle and the same ray of k-space was acquired. This was repeated to isotropically sample k-space as shown in (B).

4.3.1. In-Vitro Experiments

The feasibility of this approach was first demonstrated in vitro, on a 2T preclinical MR scanner. To create a dissolved-phase signal, hydrophobic gas-exchange membranes were used to continuously infuse ^{129}Xe into distilled water. Distilled water and gas flowed at 20 ml/min and 5 ml/min respectively, through a hydrophobic hollow fiber membrane module (MicroModule, Membrana, Charlotte, NC), where ^{129}Xe was infused into the water (98). The HP ^{129}Xe infused water passed from the modules through the center of the RF coil. The ^{129}Xe exhaust from the membrane outlet was also routed into the RF coil and wrapped around the liquid line to create a reference gas-phase signal (**figure 28**). Imaging began on the 'dissolved' ^{129}Xe resonance, and images were acquired using the modified radial sequence and the following imaging parameters: pulse duration (sinc)=1200 μs, views=2500 for each frequency, TE/TR=2/250 ms, BW=8 kHz, FOV=10 cm, resolution=$32 \times 32 \times 32$, flip angles (gas/dissolved)=20/30°. The k-space data was then split, and the dissolved and gas phase components, were reconstructed separately, using NUFFT reconstruction (99). The images shown in **figure 29**, showed that the sequence was capable of dynamically changing transmit and receive frequencies and the applied flip-angle, while sampling k-space identically for both the gas and dissolved-phase resonances.

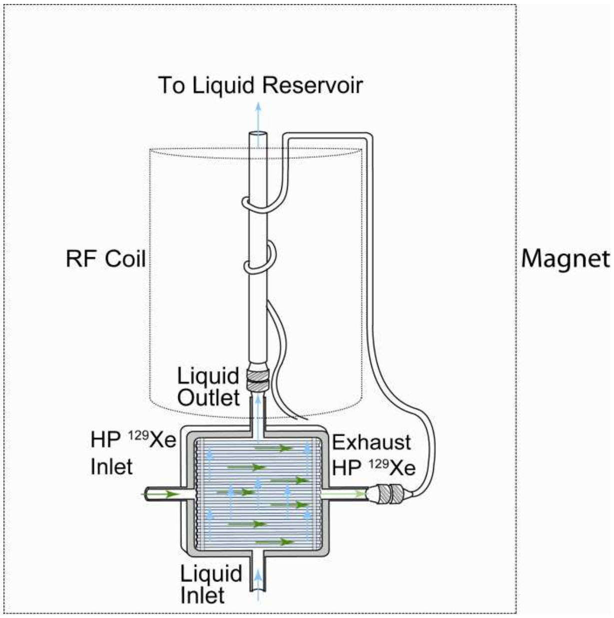

Figure 28: Imaging schematic. The exhaust gas line is wrapped around the water outlet line to provide the additional gas-phase signal.

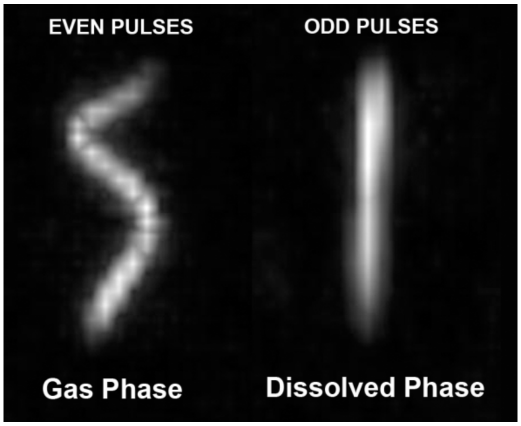

Figure 29: Maximum intensity projections of the 3D images of ^{129}Xe in the gas and dissolved-phases.

4.3.2. Clinical Imaging

With the successful in-vitro experiments, and properly characterized RF pulses, the new radial pulse sequence was ready for clinical imaging. As the clinical images need to be completed in a 16-second breath-hold, the number of rays of k-space was chosen to under-sample k-space by a factor of ~3. To prevent gradient-infidelities, the ramp time of the gradients was kept at a higher value (~500 μs). To minimize off-resonance gas-phase excitation, the RF length was chosen to be 1200 μs, and the flip-angle for the dissolved-phase was dialed in to be 22. The acquisition began at the gas-phase with a 0.5 flip-angle. Once all the rays of k-space were acquired, the data were split and reconstructed using the NUFFT algorithm (99) to yield separate images of the gas and dissolved-phase. Thus, the modified radial pulse sequence could be used to reliably obtain isotropic, co-registered single breath gas and dissolved-phase images. An example of these images is shown in **figure 30**.

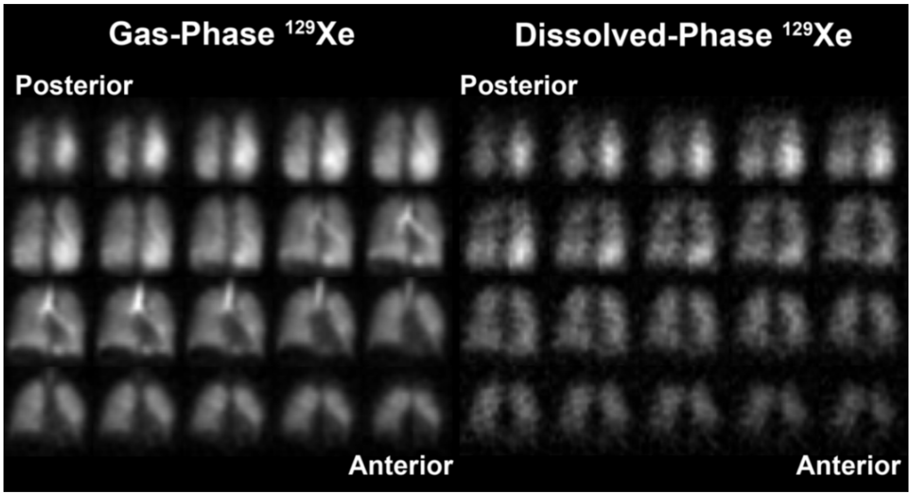

Figure 30: Example single-breath gas and dissolved-phase images acquired in a healthy volunteer.

4.4. Summary

This chapter focused on the key technical developments that enabled the reliable acquisition of 3D isotropic gas and dissolved-phase ^{129}Xe images using an interleaved 3D radial pulse sequence. This reliability was achieved by improving the selective excitation of the dissolved-phase of ^{129}Xe. With the acquisition strategy established on a reliable footing, we are ideally poised to quantify the distribution of the dissolved-phase signal, which will the focus of **chapter 5**.

5. Probing the Effect of Posture on the Distribution of Dissolved-Phase Images

The results presented in this chapter were published as a journal article: S.S. Kaushik *et al.*, '*Probing the regional distribution of pulmonary gas-exchange through single-breath gas and dissolved-phase imaging*', Journal of Applied Physiology, 2013; 115 (6), 850-860.

5.1. Motivation

With a robust ^{129}Xe gas-transfer acquisition in hand, our second goal was to develop a fundamental understanding of the physiologically relevant information provided by these images. This was done by performing ^{129}Xe MRI of the lungs under a set of conditions that are known to alter the underlying pattern of physiological gas exchange. Thus, ^{129}Xe gas-transfer was imaged in both the supine and prone position for all subjects. Such postural changes are known to alter the resting perfusion distribution (52) and diffusing capacity for oxygen (100). Moreover, our preliminary efforts in imaging the dissolved ^{129}Xe distribution showed the images were characterized by a strong postural gradient, which favored the dependent lung. We thus hypothesized that, upon developing a single-breath method of imaging ^{129}Xe gas-transfer, a postural gradient would be detectable in both the individual ^{129}Xe gas- and dissolved-phase distributions and that gravitational gradients would still be retained in the normalized ^{129}Xe gas-transfer maps. Furthermore, we hypothesized that gradients in the gas- and dissolved-phases, as well as in ^{129}Xe gas-transfer would reverse when subjects were repositioned from the supine to the prone position. Such imaging of the underlying variability of ^{129}Xe gas-transfer in healthy subjects provides a necessary platform to probe basic lung physiology and eventually understand the pathophysiological changes that arise with the onset of pulmonary diseases.

5.2. Methods

5.2.1. Subject Inclusion/Exclusion Criteria

Studies were approved by the Duke Institutional Review Board and conducted under FDA IND 109,490. Written, informed consent was obtained from all the subjects prior to the scan. All subjects were at least 18 years of age (8 men, 1 woman, average age = 45.6 ± 18.7 years) and had less than a 5 pack-year smoking history, had not smoked in the last 5 years, and had no diagnosed pulmonary disorders. The body mass index (BMI) for the subjects ranged from 19-29.6 (average BMI = 24.3 ± 3.6). Subjects were excluded if they were unable to hold their breath for 16 seconds, had a history of cardiac arrhythmias, were pregnant or lactating, or had a respiratory illness within 30 days of MRI. One hour prior to MR studies, subjects underwent pulmonary function testing, including measures of total lung capacity (TLC) that were used to interpret aspects of the MR images.

5.2.2. Xenon Polarization and Delivery

Each subject received two 1-L doses of HP ^{129}Xe (isotopically enriched to 86% ^{129}Xe, Linde Gases, Stewartsville, NJ). The polarization process is described in **chapter 2**. Prior to gas inhalation, subjects were instructed to inhale to TLC and exhale to functional residual capacity (FRC) twice. They then inhaled the gas through 0.95-cm ID Tygon tubing (Saint Gobain Performance Plastics, Akron, OH) and held their breath for a maximum of 16 seconds while the images were acquired. Throughout the imaging session, blood oxygenation and heart-rate were monitored using an MR-compatible monitoring system (GE Healthcare, Helsinki, Finland).

5.2.3. MR Acquisition and Workflow

Studies were conducted on a 1.5-T scanner (GE Healthcare EXCITE 15M4, Waukesha, WI) equipped with a 2-kW broadband (8–70 MHz) amplifier for the multinuclear RF chain (CPC, Hauppauge, NY). Subjects were fitted in a quadrature ^{129}Xe vest coil (Clinical MR Solutions, Brookfield, WI) tuned to 17.66 MHz and proton-blocked to permit ^{1}H MRI of the thoracic cavity to be performed with the scanner's body coil, without repositioning the subject.

Single breath gas and dissolved-phase were acquired with the following parameters: sinc pulse duration = 1.2 ms, TE/TR = 0.932/7.5 ms, matrix = 32×32×32, 1001 rays for each frequency, gas flip-angle = 0.5°, dissolved flip-angle = 22°, bandwidth = 15.625 kHz, FOV = 40 cm. the k-space data was then reconstructed using the NUFFT algorithm. In order to constrain the image analysis to the thoracic cavity, radial ^{1}H images were acquired with the following parameters: hard pulse duration = 274 μs, TE/TR = 0.336/2.4 ms, matrix = 64×64×64, 5647 rays, 512 dummy pulses, flip-angle = 5°, bandwidth = 15.625 kHz, and FOV = 40 cm.

The imaging workflow was as follows: after the acquisition of a free breathing localizer in the supine position, ^{1}H radial thoracic-cavity images were acquired after the subject had inhaled 1-L of air from a polyethylene bag from functional residual capacity. This was followed by administering 1-L of ^{129}Xe for single-breath acquisition of the gas- and dissolved-phase distributions in the supine position. The subject was then transferred to the prone position without changing the coil orientation, and a second, 1-L single-breath scan of the dissolved and gas-phase distribution was acquired. This was followed by another radial breath-hold ^{1}H thoracic cavity scan in the prone position.

The 1-L air bag was used to make sure that the lung was expanded to roughly the same volume as during the ^{129}Xe scan.

5.2.4. Quantitative Analysis of Images

To match the resolution of the anatomical images, the ^{129}Xe gas-phase images were up-sampled from their native 32×32×32 matrix to 64×64×64, using bilinear interpolation. The ^{1}H and gaseous ^{129}Xe images were then registered using a multi-resolution, affine transformation, with joint entropy as the cost function and a cubic-spline interpolation using the Image Registration Toolkit (101). This is illustrated in **figure 31A** and **31B**. The thoracic-cavity ^{1}H image was then segmented using the region-growing algorithm in 3DSlicer (36) to create a binary thoracic-cavity mask (**figure 31C**). This mask was then manually segmented to remove airways, morphologically closed using a spherical structuring element (diameter = 7 voxels), and was followed by an additional filling operation, in MATLAB™ R2011a (MathWorks, Inc., Natick, MA) to create the final mask shown in **figure 31D**. **Figure 31E** shows multiple slices of the thoracic cavity image and the corresponding, processed thoracic cavity mask.

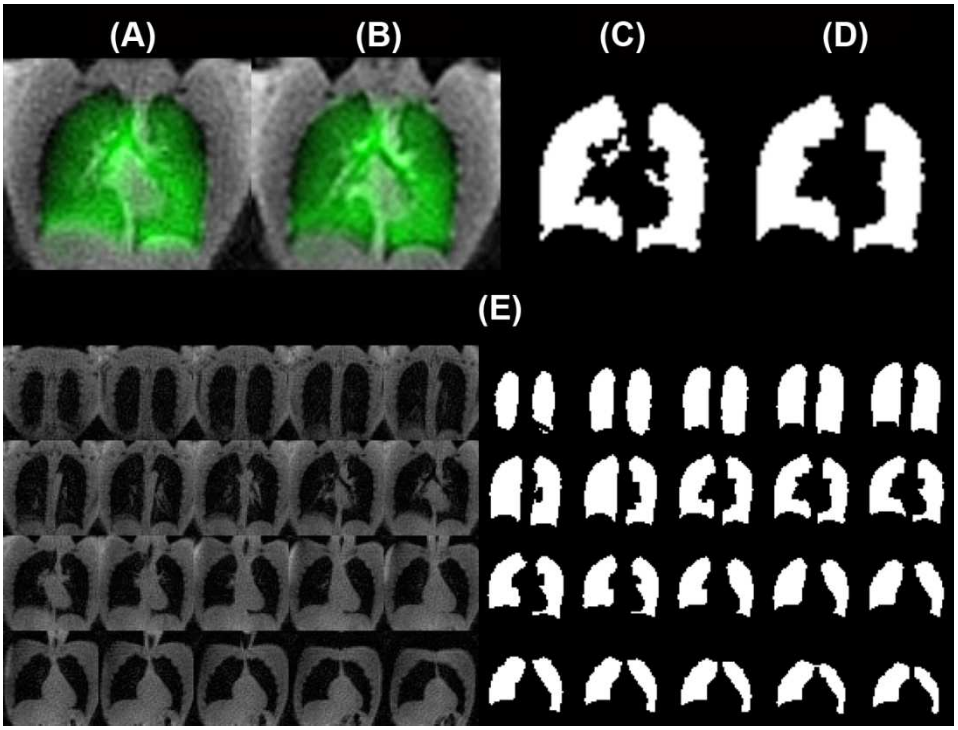

Figure 31: Image processing to limit analysis to the thoracic cavity. In spite of volume-controlling the acquisitions, (A) shows a significant mis-registration of the gas-phase image (green) and the thoracic cavity image (gray), which is reduced post registration in (B). Registered thoracic cavity image used to create a "mask" as shown in (C), which is manually segmented and morphologically closed to create the mask in (D). (E) shows the thoracic cavity image and the corresponding processed mask.

Both gas- and dissolved-phase images were normalized by the sum of their respective voxel intensities within the thoracic cavity mask (16), and the resulting dissolved-phase images were divided on a voxel-by-voxel basis by the corresponding gas-phase images to create the gas-transfer maps. **Figure 32** shows an example of these gas-transfer maps in a supine healthy subject.

The axial gas and dissolved-phase images in **figure 32** exhibit a gravitational gradient. However, when these images are normalized and divided, this gradient is retained in the gas-transfer maps**.** The gas-transfer is higher in the dependent lung and diminishes in the anterior, non-dependent lung. Hence, the gas-transfer itself exhibits a gravitational gradient beyond what is attributable to the gas-phase ^{129}Xe distribution.

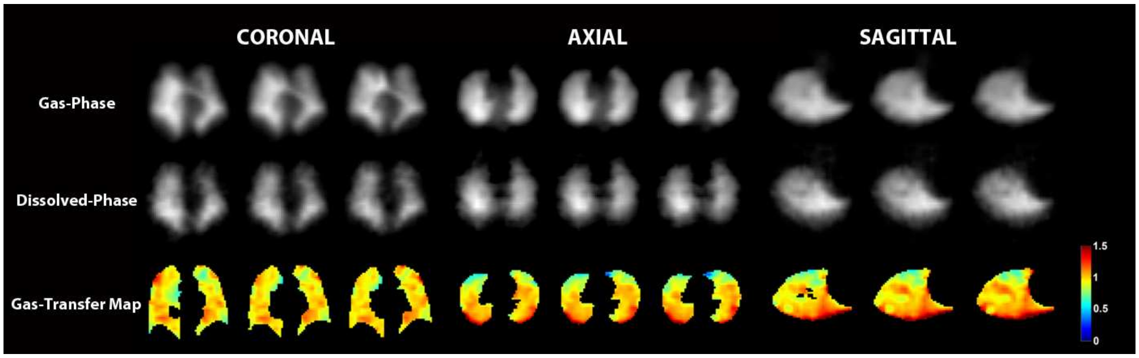

Figure 32: Representative single breath, isotropic gas- and dissolved-phase images and the corresponding gas-transfer map, defined as the normalized dissolved-phase image to gas-phase image ratio.

5.3. Study Results

5.3.1. Postural gradients

An example showing the impact of posture on the gas-transfer map is shown in **figure 33**. When supine, as seen in **figure 33A**, this subject showed decreasing gas-transfer from the posterior to anterior lung. However, when the subject was prone (**figure 33B**), this gas-transfer gradient reversed, and showed higher values in the anterior lung that decreased towards the posterior lung. This is made clearer in **figure 33C**, where the gas-transfer distributions are plotted as a function of slice position. This plot shows quantitatively, the visual reversal seen in **figures 33A** and **33B**. Furthermore, it also speaks to the extent of gas-transfer variability in this subject, who showed a 43% change in gas-transfer when supine, and 27% when prone. Also, in both postures, gas-transfer was non-monotonic and showed a marked increase in slices iso-gravitational with the main pulmonary arteries. The results for this subject are representative of most subjects scanned. To quantify this posterior-anterior signal intensity gradient, the images were subjected to a linear-regression (weighted by voxel count) of the mean signal intensity of each slice as a function of slice position. These results are summarized in **table 3.**

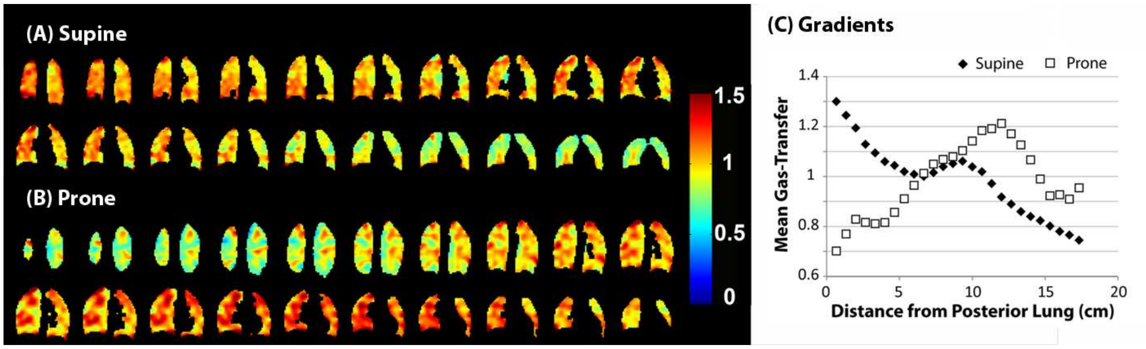

Figure 33: Representative gas-transfer map from a healthy volunteer (subject 2) in the supine (A) and prone (B) positions. (C) Mean gas-transfer as a function of lung position, showing higher gas-transfer in the dependent lung for both postures.

Table 3: Subject demographics and postural gradients

Sub	Age (yrs)	TLC (L)	Gradients (% of mean cm^{-1})						Mean Gas-Transfer	
			Supine			Prone				
			Gas	Dissolved	Gas-Transfer	Gas	Dissolved	Gas-Transfer	Supine	Prone
1	29	9.16	-3.51	-5.30	-2.28	-1.16	2.34	3.24	0.997	1.017
2	60	8.05	-2.43	-4.85	-2.56	3.37	5.55	2.45	1.003	1.001
3	68	7.00	-2.19	-4.15	-2.32	1.13	2.69	1.94	1.001	0.999
4	23	7.84	-3.28	-4.84	-2.08	-3.88	-0.93	2.95	0.991	1.011
5	59	7.56	-2.54	-3.57	-1.36	2.07	4.49	2.78	0.988	0.997
6	65	7.17	2.40	0.54	-1.98	-0.21	0.10	0.46	1.008	1.008
7	51	5.74	-2.17	-3.42	-1.34	1.90	3.96	2.32	0.996	1.003
8	22	6.71	-1.71	-2.13	-0.80	-1.66	-0.74	1.42	0.998	1.005
9	33	7.96	-1.81	-5.30	-3.24	0.95	2.34	-0.08	1.026	1.010

Changes in the posterior-anterior gradients (slope of the regression line) and mean gas-transfer difference between postures were evaluated for significance using a matched pair T-test. The significance level was set at 5% ($p < 0.05$) for all comparisons. Gas-phase images exhibited a modest population-mean posterior-anterior gradient of -1.92 ± 1.73% cm^{-1} for supine subjects that reversed and diminished significantly to 0.28 ± 2.23% cm^{-1} ($p = 0.042$) when the subjects were prone. Dissolved-phase ^{129}Xe images exhibited a larger posterior-anterior gradient of -3.46 ± 1.91% cm^{-1} for supine subjects that did reverse significantly ($p = 0.0034$) to 2.18 ± 2.47% cm^{-1} when subjects were prone. These gradients persisted in the gas-transfer maps, and these also reversed significantly ($p < 0.001$) when subjects changed from the supine (-1.99 ± 0.74% cm^{-1}) to prone (1.94 ± 1.14% cm^{-1}) position. These results are shown in **figure 34** and summarized in **table 4**.

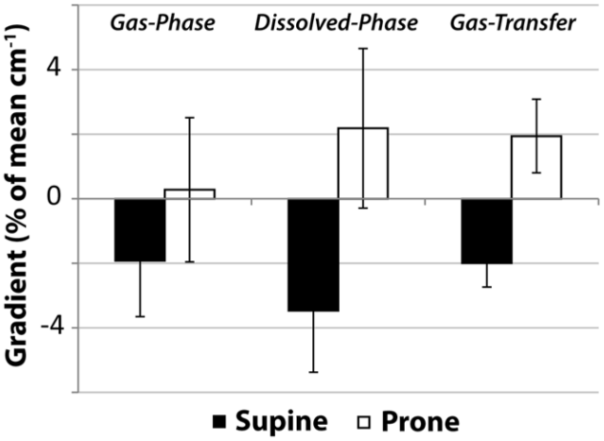

Figure 34: Signal intensity and gas-transfer gradients for all subjects. Gas-phase gradients were significantly impacted by posture ($p = 0.042$). Dissolved-phase images also showed a significant gradient reversal when subjects were repositioned from the supine to the prone position ($p = 0.0034$). The gradient in gas-transfer also reversed significantly when subjects were repositioned from supine to prone ($p < 0.0001$).

Table 4: Mean gas-transfer gradients and coefficients of variation

Posture	Gas	Dissolved	Gas-Transfer
Gradients			
Supine	-1.92 ± 1.73	-3.46 ± 1.91	-2.00 ± 0.74
Prone	0.28 ± 2.23	2.18 ± 2.47	1.94 ± 1.14
Coefficient of Variation			
Supine	0.34 ± 0.05	0.38 ± 0.05	0.19 ± 0.04
Prone	0.32 ± 0.04	0.36 ± 0.05	0.20 ± 0.04

5.3.2. Gas-Transfer Heterogeneity

Gas-transfer maps and source images were further analyzed for heterogeneity by calculating the coefficient of variation (CV) for the whole lung. The CV for all the subjects has been summarized in **table 4** and is graphically shown in **figure 35**. The population-mean CV of the gas- and dissolved-phase ^{129}Xe images were similar and not significantly impacted by posture (gas, $p = 0.21$; dissolved, $p = 0.22$; gas-transfer, $p = 0.45$). However, for both postures, the whole-lung CVs of the dissolved-phase image were modestly higher than those of the gas-phase images (supine, $p = 0.0001$; prone, $p = 0.0028$). Interestingly, the CV of the normalized gas-transfer maps relative to either the gas- or dissolved-phase images alone was roughly 45% lower in both positions. In spite of the pronounced spatial variation in the gas-transfer maps, the gas-transfer value averaged over the entire lung remained near unity for all subjects and displayed no significant posture-dependence (supine mean gas-transfer: 1.00 ± 0.01; prone mean gas-transfer: 1.01 ± 0.01; p = 0.25).

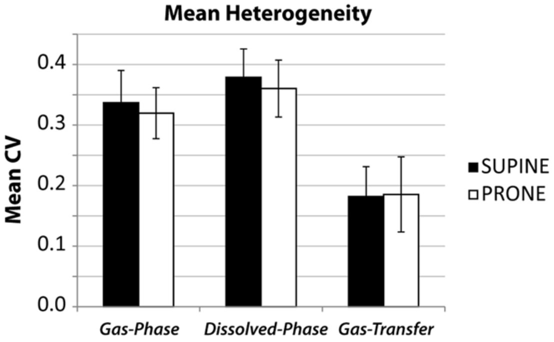

Figure 35: Population means for whole lung CVs. Mean gas-transfer CV was almost half that of the gas- and dissolved-phase images. Dissolved-phase images had significantly higher CVs than the gas-phase images for both postures (p = 0.0001, supine; p = 0.003, prone). No significant posture-dependent change in CV was observed in gas- (p = 0.22) and dissolved-phase (p = 0.21) images or gas transfer maps (p = 0.34).

5.3.3. Impact of Lung Inflation

The distribution of gas-transfer was also impacted by lung inflation. In the supine position, subjects with larger total lung capacities tended to exhibit greater gas-transfer heterogeneity than those subjects with smaller TLC. Because all subjects in this study received the same 1-L dose of HP ^{129}Xe, this meant imaging was done at lung inflation levels ranging from FRC + 10.9% of TLC to FRC + 17.4% of TLC. Hence, subjects with larger lung volumes underwent imaging at a lower degree of lung inflation. As shown in **figure 36**, for supine subjects, gas-transfer CV correlated significantly with TLC ($r = 0.77$, $p = 0.015$). However, when prone these same subjects exhibited no correlation between CV and TLC ($r = 0.18$, $p = 0.64$). Also, no significant posture-dependent difference in polarization-corrected SNR (SNR/polarization) was observed ($p = 0.55$, gas-phase; $p = 0.42$, dissolved-phase). Thus, TLC-dependent heterogeneity observed in the supine position does not appear to be explained by lower image SNR resulting from greater ^{129}Xe dilution, but instead reflects fundamental aspects of gas-transfer distribution. Similarly, CT studies have shown that tissue-density gradients are almost completely eliminated when the lung is fully expanded (102). Lower lung inflation may lead to alveolar de-recruitment and small airway closure (103), which could contribute to the increased CV seen in subjects with higher TLC. By contrast, no correlation was seen between CV and lung volume ($r = 0.2$) for prone subjects, which may be due to the more uniform lung expansion in that position (104).

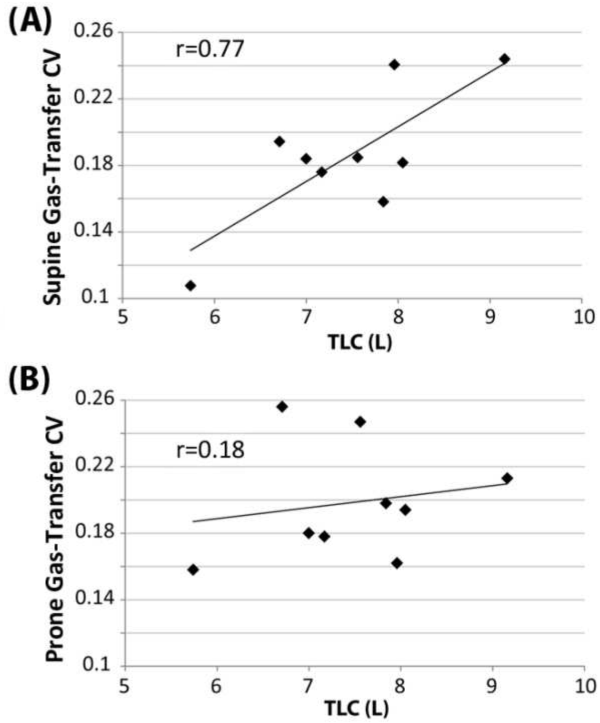

Figure 36: Whole-lung gas-transfer CV as a function total lung capacity. (A) Gas-transfer CVs in supine subjects. A significant ($p = 0.015$) increase in CV with increasing TLC is observed in supine subjects. (B) Gas-transfer CVs in prone subjects. CV in prone subjects showed no significant correlation with the TLC ($p = 0.64$).

5.4. Inferences about Gas-Transfer

5.4.1. Gravitational gradients

The acquisition and analysis method described accounts for the contribution of the gas-phase ^{129}Xe distribution to the dissolved-phase ^{129}Xe image, permitting quantitative regional mapping of ^{129}Xe gas-transfer. These maps corroborate our hypothesis that ^{129}Xe gas-transfer itself is heterogeneous in normal subjects and is subject to gravitational gradients that reverse with subject posture. Indeed, ^{129}Xe gas-transfer varies by 30-40% across the lung field. These single-breath ^{129}Xe gas-transfer images show trends that are consistent with observations from other imaging modalities and experimental techniques that image tissue density (105) and perfusion (15,16,52), while providing a unique window on the regional variability of lung function in healthy subjects.

It is important to note that ^{129}Xe gas-transfer imaging signal arises from fundamentally different physical origins than established physiologic measures of respiratory gas transfer. Firstly, since ^{129}Xe gas-transfer images are acquired in a single breath, they will report primarily on well-ventilated regions of the lung. Secondly, ^{129}Xe gas-transfer signal arises almost exclusively from the alveolar septa where diffusion from the alveolar spaces continuously replenishes the dissolved ^{129}Xe magnetization. Given that the harmonic mean thickness of the barrier L=1 micron, and the diffusion coefficient of ^{129}Xe in the barrier $D=0.33 \times 10^{-5}$ cm^2/s, ^{129}Xe takes only ~1.5 ms $\left(t = L^2/2D\right)$ to diffuse across the interstitial barrier and into the RBCs, and only ~150 ms more to saturate the septum (106). Furthermore, 40–50% of the dissolved ^{129}Xe signal originates from the capillary blood, which transits through the capillary network in 0.75 seconds. Since local blood volume tracks with perfusion (107), ^{129}Xe transfer imaging may be thought of as approximating local VQ matching. Hence, in this regard, ^{129}Xe transfer MRI is a closer surrogate for studying the oxygen transfer pathway than other imaging modalities that infer this information indirectly through ventilation and perfusion metrics.

The postural gradients in ^{129}Xe gas-transfer we observed are consistent with tissue density, ventilation, and perfusion gradients reported by other imaging modalities, which are summarized in **table 3**. For supine subjects, lung tissue density has been reported to exhibit a posterior-anterior gradient of -4.33% cm^{-1} by CT (105) and -4.9 ± 1.9% cm^{-1} by MRI (22). By comparison, the mean ^{129}Xe gas-transfer gradient of -2.00 ± 0.74% cm^{-1} for supine subjects was of the same sign, but roughly half as large. This is because ^{129}Xe transfer is affected by tissue density gradients, which in turn cause a gradient in the intra pleural pressure that similarly increases ventilation in the dependent lung. Since ^{129}Xe gas transfer is 'ventilation-normalized,' this explains why ^{129}Xe gas-transfer exhibits a smaller gradient than the dissolved signal or tissues density alone. Comparing ^{129}Xe gas-transfer distribution to perfusion distributions measured by other modalities, revealed a gravitational gradient that was of the same sign, but somewhat smaller than the perfusion gradient of -3.10 ± 1.50% cm^{-1} observed for supine subjects by SPECT (16) and roughly half the -4.40 ± 3.20% cm^{-1} gradient reported by PET (15). However, the supine ^{129}Xe gas-transfer gradient was very similar to the perfusion gradient reported by ASL (-2.10 ± 4.32% cm^{-1}), albeit with reduced inter-subject variability. For prone subjects the ^{129}Xe gas-transfer gradient was reversed and exhibited a positive slope of 1.94 ± 1.14%

cm^{-1}, which is comparable to the density gradient of 2.72% cm^{-1} measured by CT (105), as well as perfusion gradients of 2.70 ± 1.50% cm^{-1} measured by SPECT (16) and 1.11 ± 1.68% cm^{-1} by ASL MRI (52). However, it was less than half the perfusion gradient of 5.20 ± 4.30% cm^{-1} reported by PET (15). While perfusion and tissue density contribute significantly to the gas-transfer distribution, the differences noticed in the gravitational gradients can be attributed to the sensitivity of the dissolved-phase signal to the capillary blood volume (not flow), and the tissue density primarily in the acinar region of the lung.

Although all subjects demonstrated a consistent trend of increasing ^{129}Xe gas-transfer from non-dependent to dependent lung in both positions, this behavior was distinctly non-monotonic and unique to each subject scanned (see **Figure 37**). For example, when scanned prone, subjects 6, 8, and 9, exhibited prominently increased ^{129}Xe gas-transfer in the central image slices that decreased towards the anterior lung. In fact, even for supine subjects, a subtle increase in ^{129}Xe gas-transfer was seen in the central lung at the plane of the main pulmonary arteries. This was evident for 7 out of the 9 subjects, with 2 other subjects displaying a ^{129}Xe gas-transfer plateau in the central regions of the lungs. Such non-monotonic behavior has also been reported in tissue-density (105) and perfusion (108) distributions, but their origins have not been probed extensively. As a result of the non-monotonic increase in the ^{129}Xe gas-transfer in the more central slices of the lung, the full degree of ^{129}Xe gas-transfer variability in this population was poorly reflected by a simple linear gradient metric.

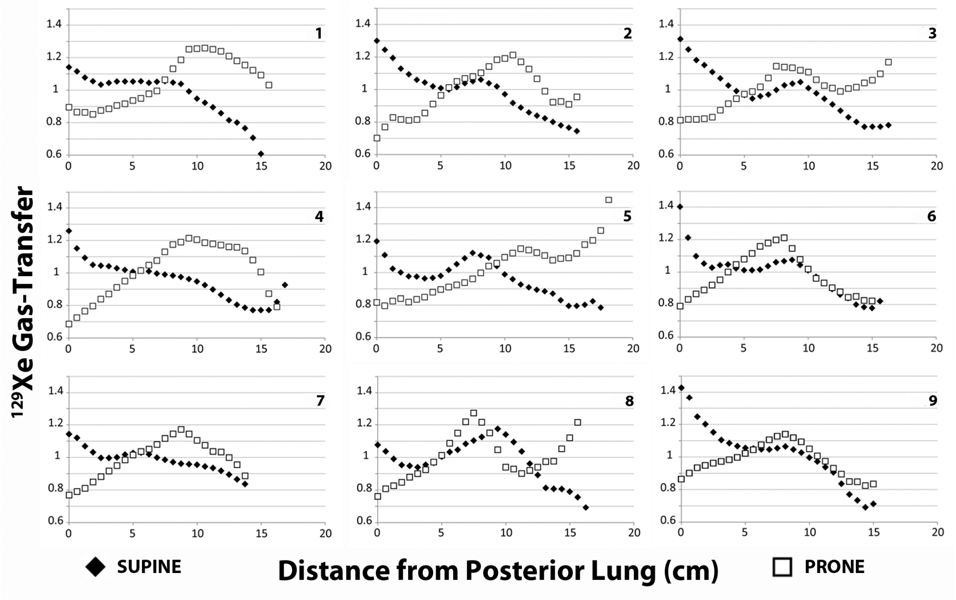

Figure 37: ^{129}Xe gas-transfer pattern for all subjects (subject number indicated in upper right-hand corner of each panel).

The general gravitational trend observed in our study is consistent with the classic West model, which predicts a larger fraction of capillary blood volume to reside in the gravitationally dependent lung (109), and hence provides a larger sink for ^{129}Xe gas-transfer. Of course, as shown by Hopkins, *et al.*, the remaining tissues of the lung also follow a gravitational "slinky"-like density pattern that favors the dependent lung (22).

5.4.2. Additional sources of heterogeneity

Beyond gravity induced changes in distribution, additional factors contribute significantly to ^{129}Xe gas-transfer heterogeneity in resting healthy subjects (110,111). One consideration may be the shape of an individual's chest cavity, which impacts regional lung expansion and alveolar recruitment (105). To this end some regions may exhibit slower ventilatory filling, which gives rise to lower gas-phase signal intensity, and consequently, lower dissolved-phase intensity.

Additionally, the effect of the heart must also be considered, because its weight compresses the pulmonary tissue beneath it, increasing tissue density in this region (112). As a greater portion of the heart rests over the left lung, we might expect differences in the ^{129}Xe gas-transfer gradient between the right and left lung. However, no such differences were observed in our study, which may suggest that ventilation is equally increased in these areas of high tissue density. Finally, the observation of increased ^{129}Xe-transfer in regions iso-gravitational with the main pulmonary arteries suggests that those capillary beds may be filled preferentially, even relative to regions experiencing greater gravitational compression.

For supine subjects, ^{129}Xe gas-transfer was also affected by the extent of lung expansion. Specifically, ^{129}Xe gas-transfer heterogeneity as measured by whole-lung coefficient of variation (CV) was found to be highest for supine subjects with larger TLC, who were therefore imaged at a lower level of lung inflation after inhaling 1-L of ^{129}Xe. This is consistent with CT studies that have shown that tissue-density gradients are almost completely eliminated when the lung is fully expanded to TLC (102). By contrast, lower lung inflation may lead to alveolar de-recruitment and small airway closure (113), which could contribute to the increased CV seen in subjects with higher TLC. However, for prone subjects, ^{129}Xe transfer CV did not correlate with lung volume (r = 0.2), which may reflect more uniform lung expansion in that position (114).

5.4.3. Gas-transfer matching

Although ^{129}Xe gas-transfer images exhibited significant heterogeneity and varying gradient patterns, the mean ^{129}Xe gas-transfer ratio for all the subjects, regardless of posture, was ~1. This finding is noteworthy considering that ^{129}Xe gas-transfer values in a given gravitational plane ranged from as low as 0.6 to as high as 1.4, and exhibited even greater range at the voxel level. Much like the well-established ventilation-perfusion ratio, the ^{129}Xe gas-transfer ratio appears to exhibit a wide range of values in healthy subjects, and yet retain nearly perfect ‘matching’ when averaged over the entire lung. The substantial regional variability observed in ^{129}Xe gas-transfer suggests that the healthy lung at rest possesses significant “reserve capacity”, a notion that has also been put forth to explain why stereology-based estimates of pulmonary diffusing capacity consistently predict diffusing capacities that exceed the experimentally measured values (115,116). In fact DL_{CO} is known to increase with cardiac output (117). Thus, it could be intriguing to conduct ^{129}Xe gas-transfer MRI in subjects undergoing either exercise-induced or physiological stress, because these conditions should make the perfusion-dependent capillary bed filling more uniform, and would be expected to result in correspondingly uniform ^{129}Xe gas transfer maps, and exhibiting a narrower range.

5.4.4. Gas-Transfer Gradients in Subjects with Disease

In addition to the healthy subjects, single-breath gas and dissolved-phase images were acquired in the supine position, in two subjects with disease – one with idiopathic pulmonary fibrosis (IPF) and the other was described by a physician to have a combination of emphysema and asthma. Shown in **figure 38A** and **38B**, are the gas-transfer maps obtained in the two subjects.

The first feature that stands out in both subjects is the reduction of the gradient in gas-transfer values from the posterior dependent lung to the anterior, non-dependent lung. This gradient reduction is made obvious in **figure 38C**, which shows the gradient calculated from the images of the two disease subjects and for comparison, also shows the gradient in a healthy volunteer. As reported earlier, the mean gas-transfer gradient in the supine healthy volunteers is $-2.00 \pm 0.74\%\ \mathrm{cm}^{-1}$, and in the subject with IPF, this gradient was -0.6% cm^{-1} and for the subject with emphysema and asthma, -0.82% cm^{-1}. Mugler *et al.* similarly noted that the posterior-anterior gas-transfer gradients reduced in subjects with disease (46).

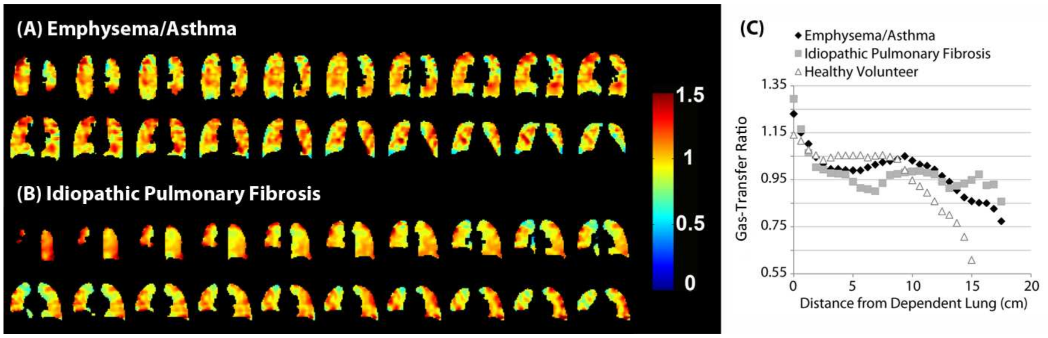

Figure 38: Gas-transfer maps in subjects with emphysema/asthma (A) and idiopathic pulmonary fibrosis (B). (C) shows gas-transfer gradients in these two subjects and a healthy subject for comparison.

This reduction in the gas-transfer gradient could once again, point to the notion of reserve capacity. The extensive alveolar damage induced by both disorders could require the subjects to use their remaining gas-exchange capacity to maintain oxygen saturation, thus minimizing the gradient in gas-transfer. Interestingly, in spite of this reduced gradient, the mean gas-transfer for the whole lung for both subjects was unity. Hence, acquiring the dissolved-phase images as a single entity may provide a good estimate of gas-transfer in the lung, but for subjects with IPF, this example suggests that there could be subtle changes in the distribution of xenon in the barrier and the RBCs, and points to the need to create separate images of the components of the dissolved-phase of xenon.

5.5. Summary

This work discussed in this chapter has demonstrated the feasibility of acquiring 3D, isotropic images of gas-phase and dissolved-phase HP ^{129}Xe in a single breath. This acquisition, coupled with appropriate normalization, enables mapping of regional gas-transfer from airspace to pulmonary blood and tissues. The study conducted to study the impact of posture on gas-transfer, has confirmed our primary hypothesis that gas-transfer in the healthy lung at rest is heterogeneous, and favors the dependent lung. Although the distribution of gas-transfer can be characterized by a linear gravitational gradient reverses when subjects are imaged prone rather than supine, this analysis does not capture the full extent of the heterogeneity. The healthy subjects studied exhibit a distinctly non-monotonic posterior-anterior variation of gas-transfer with particularly increased values in the plane of the main pulmonary arteries. In aggregate, this study suggests that healthy individuals possess a significant reserve capacity for gas-transfer, which results in a heterogeneous distribution under basal conditions. However, while that distribution has some similarities among subjects, it also appears to follow patterns specific to individual body habitus. Furthermore, in the two subjects with disease, in spite of the whole lung gas-transfer being unity, we noticed that the gas-transfer gradient was significantly reduced which indicates a loss in the reserve capacity of the lung.

Given that capillary blood contributes significantly to the gas-transfer intensity in a given voxel, the study of the impact of posture and the data from the subjects with disease point to the value of further separating the dissolved ^{129}Xe signal into its parenchymal tissue and red blood cell (RBC) components (118).

6. Gas-Transfer Spectroscopy as a Biomarker for Diffusion-limitation

The results presented in this chapter were published as a journal article: S.S. Kaushik *et al.*, '*Measuring Diffusion-limitation with a Perfusion-Limited Gas – Hyperpolarized ^{129}Xe Gas-transfer Spectroscopy in Patients with Idiopathic Pulmonary Fibrosis*', Journal of Applied Physiology, 2014; 117(6), 577-585.

6.1. Motivation

As shown in **chapter 5**, the reliability of dissolved-phase imaging was significantly improved by minimizing the off-resonance excitation of the gas-phase. Additionally, acquiring an image of the gas-phase in conjunction with the dissolved-phase enabled quantification of the gas-transfer distribution, and further confirmed that this distribution varied with subject posture (119). However this work was limited in that both the barrier and RBC resonances were imaged together as a single entity. This makes it difficult to untangle the competing effects of regional changes in perfusion, interstitial thickness and alveolar-capillary surface area available for gas exchange. Hence, harnessing the properties of ^{129}Xe to more fully evaluate regional gas exchange requires the ability to detect ^{129}Xe transfer to the RBCs separately from transfer to the barrier.

Working on separating the dissolved-phase components requires understanding the physical mechanisms controlling the dissolved-phase components. The radio frequency pulses applied to excite the ^{129}Xe magnetization in the barrier and RBC, also consume it. As the xenon in either of these compartments is in dynamic exchange with the xenon in the gas-phase, this depleted magnetization is replenished when ^{129}Xe atoms and their associated magnetization diffuse back into these compartments from the airspaces. This was illustrated using a mathematical model (47) as shown in **chapter 2**, and again, in **figure 39**. For a typical mean harmonic barrier thickness of 1 micron, after the depletion caused by an RF pulse, the RBC signal is replenished within 50 ms. However, if the interstitium becomes thickened even by a few microns, we see that this replenishment time is drastically increased.

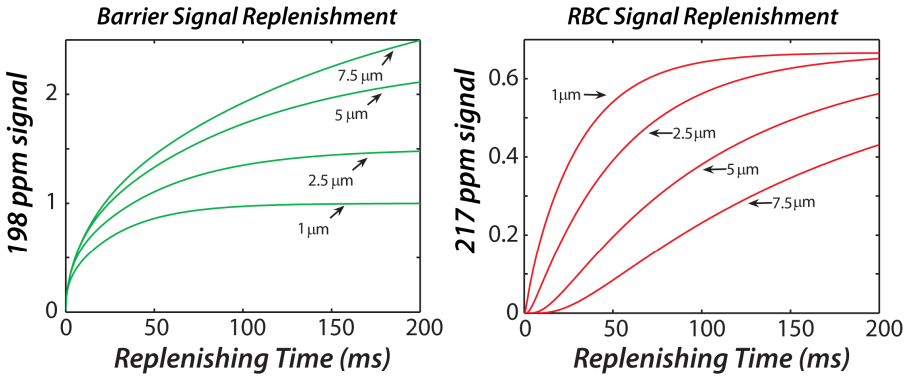

Figure 39: Signal replenishment of the dissolved-phase resonances as a function of barrier thickness. Even minimal interstitial thickening causes an increase in the replenishment time for the RBC signal.

Because these xenon atoms must first diffuse through the barrier before reaching the RBCs, it was hypothesized that the ratio of ^{129}Xe signal in RBCs versus barrier would be reduced in patients with interstitial lung disease. We sought to first test this hypothesis by employing simple ^{129}Xe gas-transfer spectroscopy to evaluate the global gas-transfer impairment averaged over the entire lung. Given the relative simplicity of implementing and executing ^{129}Xe transfer spectroscopy, and the small volumes of gas required, this measurement could be easily added to the calibration sequence of the broader ^{129}Xe MRI protocol.

An appropriate population to study this approach is in patients with idiopathic pulmonary fibrosis (IPF), a rare but particularly devastating form of interstitial lung disease, with an estimated incidence of 10.7/100000 people (120). IPF is characterized by decreased fibroblast death, which results in excessive collagen deposition that thickens the interstitial barrier tissue in the lungs causing diffusion limitation (121). IPF has a poor prognosis, with a mean survival of approximately 3 years from diagnosis (40). This is largely attributable to a lack of viable therapeutic options that can reverse or halt disease progression (120). However, numerous therapies are now under investigation for the treatment of IPF (41,122), and these clinical trials are in need of sensitive biomarkers to monitor their potential benefits and efficacy. Given the continuing need to develop non-invasive biomarkers of gas-transfer impairment, and that this patient population has known diffusion limitation (123), this group is well suited for initial evaluation of ^{129}Xe gas-transfer spectroscopy.

This chapter is going to focus on a proof of concept study which was done to establish a preliminary range of normal values for the RBC:barrier signal ratio in healthy subjects, understand the short- and intermediate-term reproducibility, and establish the degree to which ^{129}Xe gas-transfer spectroscopy correlates with conventional metrics of gas exchange such as DL_{CO}. Moreover, we tested the hypothesis that ^{129}Xe gas-transfer spectroscopy can detect impaired gas-transfer was tested in patients with IPF compared to healthy volunteers.

6.2. Methods

6.2.1. Subject Recruitment

The study was approved by the Duke Institutional Review Board and written informed consent was obtained from all subjects prior to recruitment to the protocol. ^{129}Xe spectra were acquired in 6 subjects with idiopathic pulmonary fibrosis (mean age = 66.8 ± 12.3 years, all men) and 11 healthy volunteers (mean age = 41.3 ± 17.8 years, 10 men, 1 woman). One hour prior to MR studies, all subjects underwent baseline pulmonary function testing and body plethysmography to obtain functional residual capacity (FRC) and total lung capacity (TLC) measurements by methods previously described (119), and DL_{CO} by the single breath method (124), in order to characterize lung function and lung diffusing capacity of the subject cohorts and to aid in interpreting the ^{129}Xe transfer spectra.

6.2.2. Xenon Polarization and Delivery

As detailed in **Chapter 2**, isotopically-enriched ^{129}Xe (85%, Linde Gases, Stewartsville, NJ) was polarized using Rb-vapor spin-exchange optical pumping in a commercially available polarizer (Model 9800, Polarean Inc., Durham NC). ^{129}Xe transfer spectra were acquired using a 200-mL dose of ^{129}Xe, which was cryogenically accumulated and subsequently dispensed into a Tedlar bag (Jensen Inert Products, Coral Springs, FL), typically polarized between 10–14%. This dose was then mixed with 800 mL of ultra-high purity nitrogen, and administered to the subject. Prior to inhalation, subjects were coached to inhale to total lung capacity (TLC) and exhale to functional residual capacity (FRC) twice. Following this, the subjects inhaled the contents of the bag through a 6 mm ID Tygon tube, and held their breath for 4–8 seconds during which time ^{129}Xe spectra were acquired (see below). The subject's heart rate and oxygen saturation were monitored using an MR-compatible monitoring system (GE Healthcare, Helsinki, Finland).

6.2.3. Dissolved-phase Spectroscopy

6.2.3.1. Acquisition

Studies were conducted on a 1.5-T MRI scanner (GE Healthcare, 15M4 EXCITE). Subjects were fitted with a quadrature ^{129}Xe vest coil tuned to the gas-phase xenon Larmor frequency of 17.660445 MHz (Clinical MR Solutions, Brookfield, WI). Spectra were acquired in a single breath-hold with the following parameters: dissolved-phase ^{129}Xe was selectively excited by applying a 3-lobe sinc pulse of 1200 μs duration to the ^{129}Xe-RBC resonance, 3832 Hz above the gas phase. Spectra were collected with TE = 0.932 ms, TR = 20/40 ms, receiver bandwidth = 8.06/15.63 kHz, flip-angle = 15–19°, and number of FIDs = 200. Subsequently, in the same breath-hold, the transmit/receive frequency were switched to the gas-phase resonance, and with otherwise identical pulse parameters, a single gas-phase reference spectrum was acquired. The acquisition is graphically illustrated in **Figure 40**.

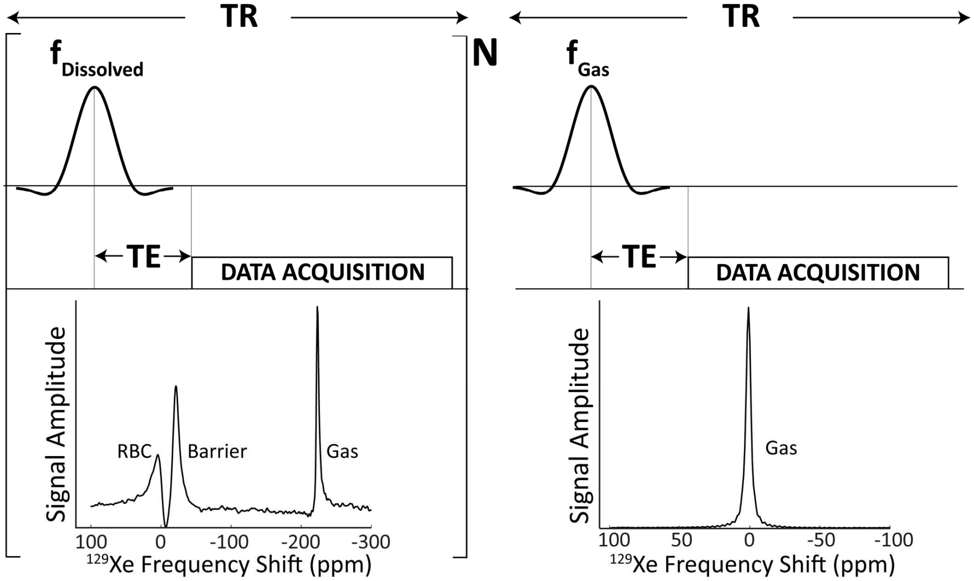

Figure 40: Acquisition scheme for the dissolved and gas-phase ^{129}Xe spectra. First, 200 dissolved-phase ^{129}Xe spectra were acquired by pulsing and acquiring on the RBC resonance, +3832 Hz above the gas-phase resonance. Then, with identical acquisition parameters, transmit and receive frequencies were lowered to match the gas-phase ^{129}Xe resonance, and a single reference spectrum was acquired.

For a subset of healthy subjects (n = 7), spectra were acquired again using the same protocol ~30 minutes later to study the short-term reproducibility. To analyze the inter-scan variability over a longer time period (t = 2.2 ± 1.8 months), 9 healthy volunteers participated in a follow-up scan, and ^{129}Xe transfer spectra were again acquired as described above.

6.2.3.2. Processing and Analysis

^{129}Xe spectra were processed in MATLAB™ (MathWorks, Natick, MA) as follows. Because the first ^{129}Xe spectra in the series occurred an arbitrary time after starting inhalation, they were expected to contain ^{129}Xe signal that had accumulated "downstream" of the pulmonary capillary beds in the larger vasculature. Therefore, the first 100 free induction decays of the series were discarded. However, their associated 100 RF pulses ensured that any ^{129}Xe signal from the larger vasculature should be depleted to ~1% of its starting value. Thus, signal in the remaining spectra originated entirely from ^{129}Xe within the capillary beds and represented a diffusive steady-state. The remaining 100 FIDs were averaged together and processed as follows. The averaged FID underwent 50-Hz line-broadening using an exponential apodizing function. Such techniques are commonly used in NMR spectroscopy to improve the SNR of spectra (125). The FID was then Fourier transformed to yield a ^{129}Xe spectrum consisting primarily of dissolved phase ^{129}Xe signal, with only a small amount of gas-phase ^{129}Xe signal to provide a reference frequency. As recently shown by Chang *et al*. (126), the complex spectrum was curve fit using a nonlinear least squares optimization algorithm to a sum of complex frequency-dependent Lorentzian functions for the three resonances (RBC, barrier and gas), allowing each to have its own amplitude, central frequency, line width, and phase, according to

$$S(f) = \sum_j S\left(f, A_j, f_j, \Delta f_j, \phi_j\right) \tag{6.1}$$

where each complex Lorentzian is given by

$$S_j\left(f, A_j, f_j, \Delta f_j, \phi_j\right) = A\left[\frac{1}{1+\left(\frac{f-f_j}{\Delta f_j}\right)^2} + \frac{i(f-f_j)}{1+\left(\frac{f-f_j}{\Delta f_j}\right)^2}\right]e^{i\phi_j} \tag{6.2}$$

and *f* is frequency, A_j is the amplitude of a given resonance, f_j its resonant frequency, Δf_j its full width at half maximum (*FWHM*), and ϕ_j its phase.

Typical fits of the real and imaginary channels of a ^{129}Xe transfer spectrum are shown in **Figure 41** along with the three fitted resonances with phase differences removed. The same fitting procedure was applied to the single gas-phase reference spectrum. The resulting fit parameters were used to compute the area under the curve (AUC) of each resonance, which for Lorentzian functions is simply the product of peak amplitude and FWHM. From these AUCs the ratio of the RBC to barrier (RBC:barrier) was calculated and used as the primary metric of gas-transfer. To further investigate whether changes in RBC:barrier ratio were caused by changing RBC or barrier signals, the ratios of each resonance to the dedicated gas-phase reference spectrum, RBC:gas and barrier:gas, were also computed.

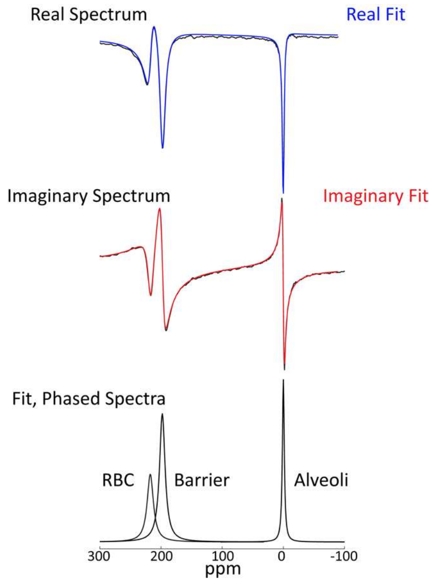

Figure 41: Curve fitting the dissolved-phase ^{129}Xe spectra. The real (blue) and imaginary (red) spectra were fit separately. The imaginary fit was re-phased by 90° and averaged with the real spectrum to generate the final fit parameters, including amplitude, frequency and spectral width for each peak.

A Wilcoxon Rank-sum test was used to test whether the various ratios, frequencies, and peak widths were significantly different between the two groups. Reproducibility was assessed using Bland-Altman plots and a pair-wise, two-tailed t-test was used to check for significant differences between the scans. Potential associations between the subject's RBC:barrier ratio and lung volume, age and DL_{CO} were also evaluated. To examine the impact of the fixed dose volume on our measurements, a metric to estimate lung inflation during ^{129}Xe signal acquisition was defined as $(FRC+1L)/TLC$, and correlated against the spectroscopic ratios for the healthy volunteers. The significance of the correlations was examined using a two tailed t-test.

6.3. Study Results

^{129}Xe gas-transfer spectra were successfully acquired in all subjects, whose demographics and pulmonary function test data are summarized in **table 5**. **Figure 42A** shows a ^{129}Xe transfer spectrum from a typical healthy volunteer compared to that of an age-matched subject with IPF. For this healthy volunteer, the RBC:barrier ratio was 0.49, whereas for the IPF subject, it was 0.17, nearly 3-fold lower.

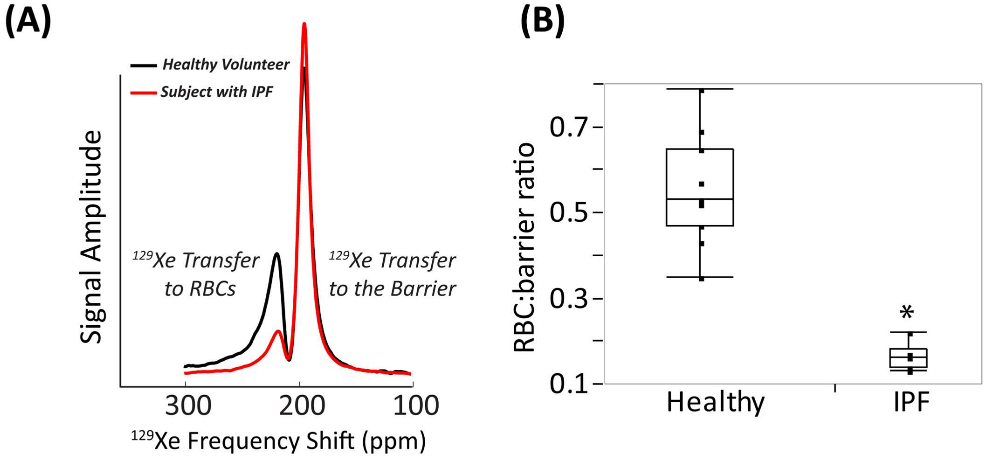

Figure 42: (A) Shows a truncated dissolved-phase spectrum from a representative healthy volunteer and a subject with IPF. Compared to the healthy volunteer, this IPF subject exhibits a 2.9-fold reduction in the RBC:barrier ratio. (B) For all subjects the RBC:barrier ratio was 0.55 ± 0.13 in the healthy volunteers, which was reduced by 3.3-fold in the IPF patients to 0.16 ± 0.03 ($p = 0.0002$).

The RBC:barrier ratio was consistently diminished in the entire IPF group relative to the healthy volunteers. As shown in **Figure 42B**, the mean RBC:barrier ratio for all healthy volunteers was 0.55 ± 0.13 compared to a more than 3-fold smaller value of 0.16 ± 0.03 for IPF subjects (p = 0.0002). Further investigation revealed that the reduced RBC:barrier ratio in IPF subjects was attributable to a 2.1-fold reduction in the RBC:gas (p = 0.02) and a 1.6-fold increase in barrier:gas (p = 0.01) (**Figure 43**). These ratios are summarized in **table 5**.

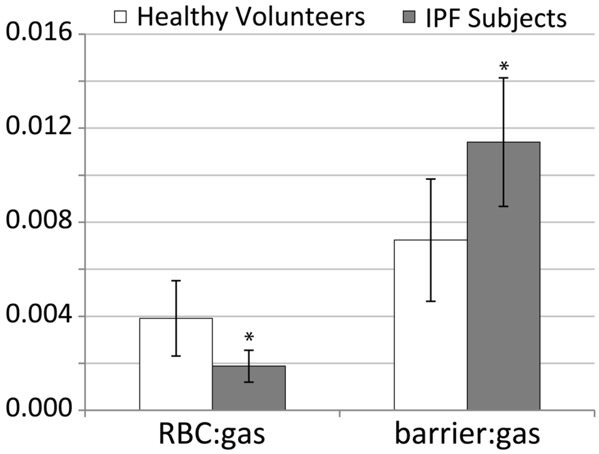

Figure 43: Comparison of the RBC:gas ratio and the barrier:gas ratio in healthy volunteers and IPF subjects. The RBC:gas ratio was reduced ~2-fold in IPF vs. healthy subjects (p = 0.02) and the barrier:gas ratio was increased ~1.6-fold in IPF subjects (p = 0.01). These two effects together reduced the overall RBC:barrier ratio in the IPF subjects.

Table 5: Subject demographics, spectroscopic ratios and pulmonary function data

Sub[a]	Age (years)	Ratios[b]			TLC[c] (L)	DL_{CO}[c] (ml min^{-1} mm Hg^{-1})	Lung Inflation (%)
		RBC:barrier	RBC:gas	barrier:gas			
1	59	0.47	0.002	0.005	7.6	23.3	59.1
2	65	0.47	0.003	0.006	7.2	28.1	62.6
3	51	0.35	0.002	0.007	5.7	21.5	74.9
4	24	0.79	0.003	0.004	6.7	26.6	66.3
5	33	0.57	0.003	0.005	8.0	31.8	68.6
6	29	0.43	0.003	0.007	6.3	27.8	61.7
7	27	0.65	0.005	0.008	7.2	42.7	54.6
8	23	0.53	0.007	0.014	7.3	31.9	46.7
9	22	0.69	0.006	0.009	9.2	29.8	54.9
10	56	0.52	0.004	0.007	6.6	25.7	70.3
11	65	0.53	0.004	0.008	7.0	30.1	59.7
1	74	0.13	0.002	0.012	4.2	10.8	-
2	83	0.22	0.003	0.013	4.7	12.6	-
3	54	0.17	0.003	0.016	3.8	11.2	-
4	51	0.14	0.002	0.011	3.3	7.2	-
5	72	0.16	0.001	0.008	4.1	9.4	-
6	67	0.16	0.001	0.009	3.8	9.4	-

In addition to their significantly lower RBC:barrier ratios, the IPF subjects also exhibited differences in their RBC resonance frequencies and widths. As shown in **table 6**, the RBC resonance frequency was 342.2 ± 15.5 Hz above the barrier resonance in healthy volunteers, but the RBC frequency was 43.3Hz lower in patients with IPF (298.9 ± 21.7 Hz, $p = 0.003$). By contrast, the frequencies of the barrier and gas-phase resonances did not differ significantly between the groups. However, the spectral widths of all three resonances were significantly different between the two groups. The mean width of the RBC resonance was 166.5 ± 16.5 Hz (with line broadening subtracted) in the healthy volunteers, but significantly narrower in the IPF subjects (125.8 ± 16.8 Hz, $p = 0.0002$). This was true for the barrier resonance as well, with the healthy volunteers exhibiting a width of 144.4 ± 10.4 Hz, and the IPF subjects exhibiting a barrier width of only 124.7 ± 6.0 Hz ($p = 0.001$). The width of the gas-phase resonance in IPF subjects was ~62% of that in the healthy volunteers (18.6 ± 6.0 Hz vs. 30.2 ± 9.6 Hz, $p = 0.01$).

Table 6: Frequencies and widths of resonances in healthy volunteers and IPF subjects

	Frequency (Hz)[a]			Width (Hz)		
	RBC (ppm)	**Barrier (ppm)**	**Gas**	**RBC**	**Barrier**	**Gas**
Healthy	342.2±15.5 (217.4)	0.0±11.0 (198.0)	-3497.0±6.5	166.5±16.5	144.4±10.4	30.2±9.6
IPF	298.9±21.7 (214.3)	-5.0±9.7 (198.2)	-3500.2±13.8	125.8±16.8	124.7±6.0	18.6±6.0
p-value	0.003	0.18	0.18	0.0002	0.0009	0.01

[a] Frequencies are referenced to the mean barrier resonance frequency in the healthy volunteers. Chemical shift (ppm) referenced to the gas phase frequency of 17.66 MHz.

As shown in **Figure 44A,** the RBC:barrier ratio obtained in healthy volunteers during a given MRI session did not change significantly. The mean difference between scans 1 and 2 was 0.036 ± 0.06 or 6.6% (p = 0.15) as seen in **table 7**. While RBC:barrier was highly reproducible within a given imaging session, it did change significantly over scans conducted on different days. On average, the RBC:barrier ratio acquired on the second day of scanning was 8.25% lower than on day one, and this was significant (p = 0.01). As shown in **table 8**, the bulk of this variability was contributed by 2 subjects whose RBC:barrier ratios were reduced by 24.5% and 16.5% (subjects 2 and 7) between scan and rescan. The RBC:gas and barrier:gas metrics however, showed no significant short-term or inter-scan change ($p > 0.1$). The same was true for the frequencies and widths of all three resonances, all of which were highly reproducible ($p > 0.1$).

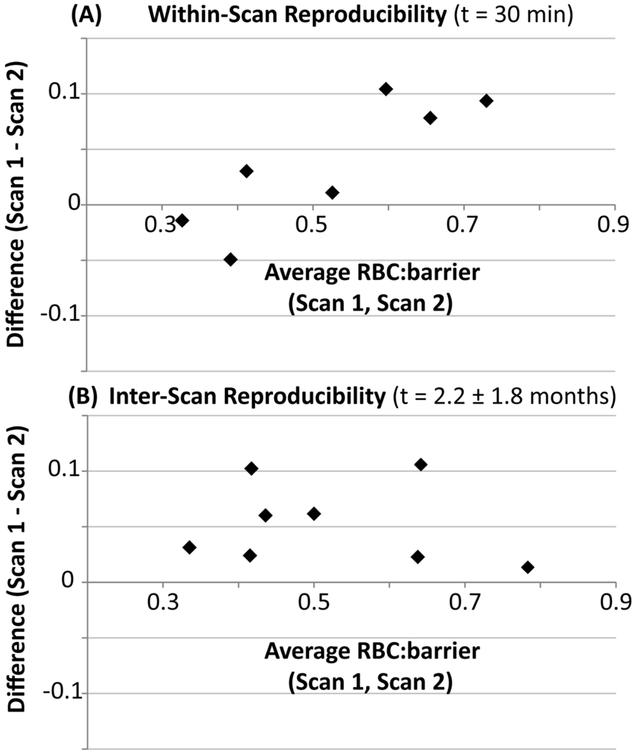

Figure 44: Bland-Altman plots showing the reproducibility of the RBC:barrier ratio. (A) Within a given session, RBC:barrier had a variability of 6.6%, which was not significant. (B) Over different scanning sessions, RBC:barrier was significantly reduced in the follow-up session ($p = 0.01$), with a mean variability of 8.25 %.

RBC:barrier across all subjects studied, correlated to a high degree with DL_{CO} ($r = 0.89$, $p < 0.0001$, **Figure 45A**). There was also evidence that for healthy subjects, total RBC signal depended on lung inflation level during acquisition (**table 5**). Since the subjects received an identical fixed volume of gas, those with larger total lung capacity (TLC), were scanned at a lower level of lung expansion. As shown in **Figure 45B,** we found a robust association between the RBC:gas ratio and the lung inflation parameter (r = -0.78, p = 0.005). The barrier:gas ratio also correlated with lung inflation (r = -0.67, p = 0.025); however, the RBC:barrier ratio did not (r = -0.28, p = 0.40).

Table 7: Intra-scan variability of the spectroscopic ratios

Subject	Ratios					
	RBC:barrier		RBC:gas		barrier:gas	
	Scan 1	Scan 2	Scan 1	Scan 2	Scan 1	Scan 2
2	0.37	0.42	0.003	0.004	0.006	0.01
3	0.32	0.33	0.003	0.002	0.007	0.007
4	0.78	0.68	0.003	0.003	0.004	0.005
6	0.43	0.40	0.003	0.003	0.007	0.007
7	0.65	0.55	0.005	0.004	0.008	0.007
8	0.53	0.52	0.007	0.008	0.014	0.014
9	0.70	0.62	0.006	0.005	0.009	0.008

Table 8: Inter-scan variability of the spectroscopic ratios

Subject	Ratios					
	RBC:barrier		RBC:gas		barrier:gas	
	Scan 1	Scan 2	Scan 1	Scan 2	Scan 1	Scan 2
1	0.47	0.41	0.0024	0.0026	0.0050	0.0065
2	0.47	0.37	0.0030	0.0026	0.0064	0.0070
3	0.357	0.32	0.0025	0.0020	0.0070	0.0063
4	0.797	0.78	0.0029	0.0032	0.0036	0.0041
6	0.43	0.40	0.0030	0.0034	0.0069	0.0085
7	0.65	0.63	0.0050	0.0059	0.0077	0.0095
8	0.537	0.47	0.0072	0.0091	0.0136	0.0194
9	0.70	0.59	0.0063	0.0035	0.0091	0.0060
11	0.53	0.54	0.0042	0.0041	0.0080	0.0078

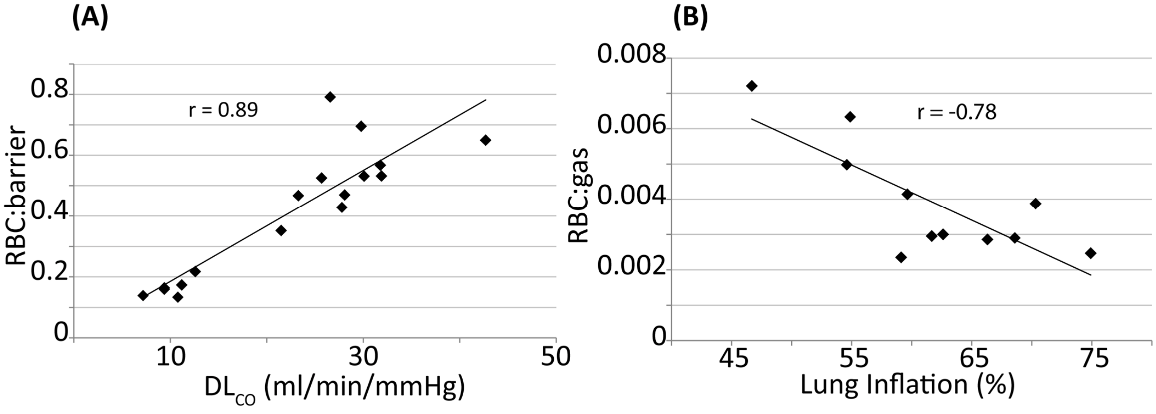

Figure 45: Correlations of gas-transfer metrics. (A) RBC:barrier was strongly correlated with DL$_{CO}$ (r = 0.89, p < 0.001). (B) In healthy subjects, the RBC:gas metric was significantly reduced by greater lung inflation (r = -0.78, p = 0.005).

6.4. Inferences about ^{129}Xe Gas-Transfer

6.4.1. Measuring diffusion-limitation with a perfusion-limited gas

The ability to use ^{129}Xe to measure diffusion limitation may appear counter-intuitive given that xenon, like other inert gases, is traditionally considered to be "perfusion-limited." This apparent paradox was recently explained by Cleveland *et al*. (48), who pointed out the fundamental differences between MR-based detection of hyperpolarized ^{129}Xe magnetization and traditional diffusing capacity measurements. Standard physiological measurements of gas-transfer exploit the physical consumption of a tracer (V) in accordance with Fick's law $V = \frac{Ad\left(P_A - P_C\right)t}{x}$ (67), where A is the surface area, d is the diffusion constant, P_A is the alveolar partial pressure of the tracer, P_C is the capillary partial pressure of the tracer, t is the measurement time and x is the thickness of the membrane. This consumption is driven by the alveolar-capillary partial pressure gradient (P_A - P_C). Since inert gases like xenon quickly saturate the alveolar septum and cause this partial pressure gradient to vanish, the only means to remove more xenon from the alveolar spaces during a breath hold is to increase perfusion. This is why xenon is considered to be “perfusion-limited.”

In order to measure diffusion limitation by traditional means, carbon monoxide (CO) is typically used because it binds strongly to hemoglobin such that the pulmonary blood acts as an “infinite sink” and the alveolar-capillary partial pressure gradient is maintained (127). In this way, the bulk consumption of CO during a breath-hold is primarily limited by its rate of diffusion across the blood-gas barrier. If the blood-gas barrier thickness increases, the flux of CO across it is reduced and less CO is taken up by the capillary blood before it exits the gas-exchange region.

However, when HP ^{129}Xe is combined with MR-based detection and destruction of magnetization, it can detect diffusion limitation. It should be noted that while the net flux of xenon atoms across the barrier is zero, the net flux of ^{129}Xe *magnetization* into these compartments is non-zero. This is because the radio frequency (RF) pulses used to detect dissolved ^{129}Xe magnetization, also consume it. This depletion can only be replenished by new magnetization from the xenon diffusing in from the alveolar compartment (106).

Because the barrier is adjacent to the alveoli, magnetization within this compartment is replenished first. By contrast, the RBC compartment cannot be replenished until ^{129}Xe magnetization has traversed the barrier. Thus, ^{129}Xe magnetization in the barrier and RBCs is "pinned" to a depleted, non-equilibrium value by continuous RF irradiation. With a thickened barrier, the magnetization flux to the RBCs will be particularly diminished, as the time it takes for the magnetization to diffuse across a barrier (τ) scales as the square of its thickness (Δx) as $\tau \sim \frac{\Delta x^2}{2D}$ (47). Such thickening only impacts the replenishment of the RBC resonance, since only this compartment is separated from the airspaces by the barrier tissue. By contrast, the barrier signal is not diminished by thickening, and depending on its chemical composition, this signal can even be increased by inflammation or fibrosis. Hence, with the proper choice of acquisition parameters, interrogating HP ^{129}Xe signal in the RBCs relative to the ^{129}Xe signal in the barrier can detect diffusion impairment.

In this small subject population, the global RBC:barrier ratio exhibited a considerable dynamic range. For example, one IPF subject exhibited an RBC:barrier more than 5-fold lower than the largest ratio seen in a healthy volunteer (0.79). This supports our hypothesis that ^{129}Xe transfer spectroscopy can serve as a marker of diffusion impairment. This is further bolstered by a strong correlation between RBC:barrier and the well-established measure of pulmonary gas exchange, DL_{CO}. Although these two techniques differ substantially in their implementation, they are able to measure similar effects.

6.4.2. Gas-transfer in healthy volunteers

The mean RBC:barrier ratio in healthy volunteers was 0.55 ± 0.13, but exhibited a relatively broad range (0.35–0.79), even in this relatively small subject population. The lowest ratio observed was 0.35 or 64% of the population mean, whereas the largest value of 0.79 was 144% of the population mean. In healthy volunteers, we assume that the blood-gas barrier is of normal thickness, and there exists no diffusive limitation to ^{129}Xe reaching the RBCs. Thus, the remaining source of variability appears to be contributed by individual differences in the resting capillary blood volume. If a greater fraction of the capillary bed is recruited and perfused at rest, this provides a larger pool of RBCs for ^{129}Xe to enter, and the RBC:barrier ratio will increase accordingly. Additionally, as noticed by Qing *et al*. (49), our healthy volunteers with the largest lung capacity also exhibited the greatest RBC:barrier ratio. This is likely because for these subjects, inhaling 1 liter of gas from functional residual capacity (FRC) left them at the lower lung inflation during data acquisition, and this resulted in a larger capillary blood volume during MR acquisition (128).

The potential sensitivity of RBC:barrier to lung inflation was illustrated in one healthy volunteer who conducted a series of breathing maneuvers during continuous acquisition of ^{129}Xe spectra. With the same acquisition parameters described in the methods section, 803 spectra were acquired over a 16 second time interval. During this time, the subject performed a 4 s breath hold, followed directly by a 4 s Valsalva maneuver (positive pulmonary pressure caused by forced exhalation against a closed airway), a 4 s Müller maneuver (negative pulmonary pressure caused by forced inhalation against a closed airway), and finally an exhale to FRC during the remaining 4 s. This is shown in **figure 46**.

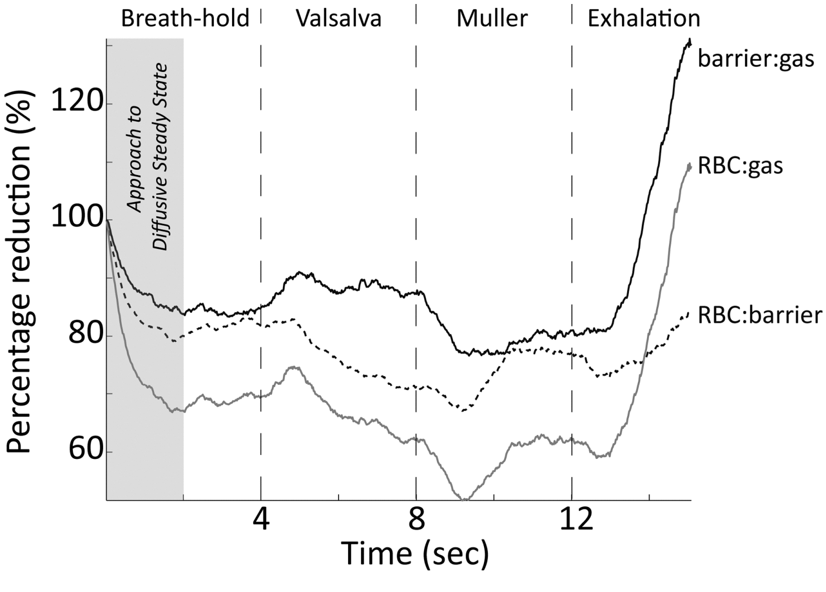

Figure 46: Changes in the RBC:gas, RBC:barrier and barrier:gas ratios observed during a breath-hold. Spectra were processed using a 'sliding-window' processing technique to provide a pseudo-temporal depiction. During the breath-hold, RBC:gas

and RBC:barrier ratio are initially reduced by depletion of ^{129}Xe magnetization in the larger vasculature (downstream signal). During the Valsalva maneuver RBC:gas diminishes while barrier:gas remains stable, resulting in diminishing RBC:barrier ratio. This is attributable to a reduction in capillary blood volume during the maneuver. Conversely, the Müller maneuver increases capillary blood volume, and hence the associated ratios. Exhalation increases overall gas-transfer, but also maximally increases capillary blood volume, which is reflected in an increasing RBC:barrier.

During the initial 2-seconds of the breath-hold, ^{129}Xe magnetization reaches a diffusive steady state as ^{129}Xe magnetization in the larger vasculature (downstream signal) is depleted by RF pulsing. Then, the Valsalva maneuver increases alveolar pressure, which decreased capillary blood volume, estimated to be 17.2% over 5 seconds by Smith *et al*. (129) . This corresponds reasonably well to our observed 11% reduction in RBC:barrier over 4 seconds during the Valsalva maneuver. In contrast, during the Müller maneuver Smith *et al.* (129) demonstrated that capillary blood volume increases by 6.1% over 5 seconds. This again is consistent with the 5.4% increase in RBC:barrier that we observed. Lastly, during exhalation, as the alveolar pressure is greatly reduced, the transfer of ^{129}Xe to both the barrier and the RBCs increased dramatically. Although this is an anecdotal study, it illustrates that the lung inflation and alveolar pressure during the breath-hold can affect these gas-transfer metrics.

The reproducibility of the RBC:barrier ratio during repeat testing provides additional insights into this measurement. While intra-scan repeat testing showed RBC:barrier to remain stable, this ratio decreased significantly over different days (t = 2.2

± 1.8 months, 8.3%, p = 0.01). A large portion of this variability was contributed by subjects 2 and 7, whose RBC:barrier ratios were reduced by 24.5% and 16.5% on follow-up (**table 8**). The variation in subject 7 may have been caused in part by a higher heart rate during the first session relative to the second (74 bpm to 55 bpm). This higher heart rate, and presumed greater cardiac output, may increase capillary recruitment and thereby present a larger capillary blood volume into which ^{129}Xe can diffuse. However, heart rate cannot explain the change in RBC:barrier seen in subject 2 (52 bpm to 49 bpm). It may be the case that this subject had a lower resting capillary blood volume at scan 2. This could be attributable to differences in lung inflation, as previously discussed. As we did not control for subject exercise prior to the MRI study, the variability in the RBC:barrier may also be caused by differences in the subject's activity profile prior to scans.

Given these observations in healthy subjects, it appears that controlling lung inflation will be important to maximize reproducibility of measurements. However, the optimal means to do so within a ^{129}Xe MRI study is still somewhat unclear. One possibility is to inhale ^{129}Xe and continue on to TLC as is done for DL_{CO}. However, at such inflations it appears from our data that ^{129}Xe gas-transfer and capillary blood volume is minimized and SNR is reduced. Alternatively, Diaz *et al*., demonstrated excellent reproducibility of ^{3}He apparent diffusion coefficient measurements, by tailoring inhaled volumes to 15% of subject TLC (90). However, this requires *a priori* knowledge of lung volumes from plethysmography, and requires subjects reliably starting their inhalation from FRC. An alternative approach may be to make measurements at end-expiration as is common in contrast-enhanced perfusion MRI (130). Although this involves exhaling 15–20% of the ^{129}Xe magnetization, it may be the most reliable means to minimize inter-subject variability of gas-transfer measurements.

6.4.3. Gas-transfer in IPF subjects

^{129}Xe gas-transfer to RBCs was dramatically reduced in the IPF subject group. In aggregate, these patients exhibited an RBC:barrier ratio that was only 29% of the mean value seen in healthy volunteers. In fact, the lowest ratio observed in IPF, was only 24% of the mean in healthy volunteers and represented just 17% of the highest ratio observed in a healthy subject. Although RBC:barrier can vary significantly in healthy subjects, and this variability is likely attributable to differences in resting perfused capillary blood volume, this does not seem a plausible explanation for the low gas-transfer in IPF. In healthy subjects, RBC:barrier exhibited a mean variability of 8.3%, with individual excursions of 20% being somewhat rare. Thus, it seems that the more than 3-fold reduction in RBC:barrier observed in IPF subjects cannot simply be attributed to a 3-fold reduction in perfused capillary blood volume. Instead, the reduced gas-transfer to RBCs must be caused, at least in part, by thickening of the blood gas barrier. Such thickening delays the diffusive replenishment of ^{129}Xe magnetization to the RBCs. Moreover, depending on ^{129}Xe solubility within the thickened barrier, the barrier signal can actually be increased. Both of these effects work together to reduce the RBC:barrier ratio. In fact, to significantly impede the transfer of ^{129}Xe magnetization requires only 10 microns of interstitial thickening (47). Thus, we suggest that significant areas of the IPF lung remain perfused even in the presence of a thickened blood-gas barrier. These areas would contribute significantly to diffusion limitation, which we observe both with ^{129}Xe spectroscopy and conventional DL_{CO}. This notion is further supported by pulmonary ventilation/perfusion imaging using high-resolution CT showing that, even in injured or inflamed lung, perfusion can be maintained to continue resolving the insult, despite the deleterious effect on O_2 saturation (131).

6.4.4. Changes in the frequency and width of ^{129}Xe resonances

While the amplitudes of the ^{129}Xe RBC and barrier resonances are of primary interest, their frequency and spectral width convey additional insights regarding capillary blood oxygenation and hemoglobin levels (132,133). A somewhat surprising finding was that the frequency of the RBC resonance was ~43 Hz (2.3 ppm) lower in patients with IPF than in healthy volunteers (**table 6**). This may be understood by considering the work of Wolber *et al.*, who reported in vitro studies showing that the frequency of the

RBC resonance increases with oxygen saturation (132). The RBC frequency increases by 5 ppm (88 Hz at 1.5 T) over an oxygen saturation range of 30 – 100% (132). Interestingly, our observed RBC frequency of 217.4 ppm in healthy subjects lies below the 221 ppm in vitro value reported by Wolber *et al*. for fully oxygenated blood, and suggests that average SpO_2 in our healthy population is only ~0.95. The 2.3 ppm lower RBC frequency in our IPF patients suggests an average SpO_2 of only 0.60. However, pulse oximetry in all our subjects revealed that healthy subjects had an SpO_2 above 95%, and even IPF patients had SpO_2 above 90%. This apparent discrepancy can be reconciled by recognizing that SpO_2 is measured in the distal vasculature, whereas ^{129}Xe spectroscopy reports from within the alveolar capillary bed. Hence, even in healthy subjects, a fraction of the ^{129}Xe-RBC resonance arises from cells that are early in their transit through the capillary bed and are not yet fully oxygenated. However, in healthy subjects, such oxygenation is largely complete within 1/3 of the blood transit time, and thus ^{129}Xe spectra are derived from roughly 2/3 fully oxygenated blood and 1/3 partially oxygenated blood. By contrast, the diffusion limitation in IPF means that maximal oxygenation is only achieved towards the very end of alveolar-capillary transit. Hence, ^{129}Xe spectra in IPF are more heavily weighted towards deoxygenated RBCs. Thus, the reduced ^{129}Xe-RBC frequency in IPF appears to be a second indicator of diffusion limitation. Interestingly, as interstitial thickness will vary across the lung, along with their attendant oxygen saturation times, it may become possible to crudely image such regional oxygenation, by employing chemical shift imaging and measuring RBC frequencies locally (134). By contrast, the frequency of the barrier resonance did not differ significantly between IPF and healthy subjects, consistent with literature reports that it is independent of blood oxygenation (132).

Of further note is that the spectral widths (full width at half maximum [FWHM]) of all three ^{129}Xe resonances are significantly narrower in subjects with IPF than in healthy volunteers (**table 6**). For example, the width of the barrier resonance was 144.4 ± 10.4 Hz in healthy volunteers but was reduced to 124.7 ± 6.0 Hz in the IPF subjects ($p = 0.001$). The width of ^{129}Xe resonances is driven by exchange of ^{129}Xe between the different frequency environments. For the simple case of ^{129}Xe in whole blood, the width of the barrier (plasma) resonance is known to increase linearly with hematocrit (133) as ^{129}Xe exchanges between the RBCs and plasma. The nominal barrier width is ~127 Hz ($T2 \approx 2.5$ ms) for whole blood with hematocrit of 38 ± 2% (133). The diminished barrier width we observed in IPF may indicate that a greater fraction of the barrier resonance is contributed by ^{129}Xe further removed from the RBCs in the now thickened interstitium, where exchange with RBCs is absent. Like the barrier resonance, the RBC resonance was also considerably broader in the healthy volunteers (166.5 ± 16.5 Hz) than in IPF patients (125.8 ± 16.8 Hz, $p = 0.0002$). The RBC resonance in healthy volunteers was only slightly broader than reported in pure RBCs in vitro, which have a width of ~152 Hz (T2 ≈ 2.1 ms (133)). Thus, while the ^{129}Xe-RBC resonance frequency is affected by oxygenation, its narrower width in IPF may indicate that those RBCs experience fewer susceptibility gradients as fibrotic processes keep them more distal from the air-tissue interfaces. Finally, the gas-phase resonance was also broader in the healthy volunteers (30.2 ± 9.6 Hz) than in IPF subjects (18.6 ± 6.0 Hz, $p = 0.01$). This may indicate that some portion of the gas-phase linewidth in healthy volunteers is contributed by exchange into the dissolved-phase compartments, and this exchange may be impeded in the presence of fibrosis.

6.4.5. Study Limitations

There are several technical limitations that must be considered when interpreting the RBC:barrier and other ratios reported here. ***Firstly***, the measurement is likely to depend on the choice of RF pulse repetition time and flip angle. If a lower flip angle and/or longer TR were used, ^{129}Xe magnetization in RBCs would not be depleted as much and significant RBC signal might arise from larger vasculature to increase the RBC:barrier ratio. Similarly, the opposite case of larger flip and/or shorter TR would limit RBC replenishment and reduce the RBC:barrier ratio. The flip-angles used to acquire spectra in our study varied between 15.3° and 19.6° because they were taken prior to transmitter gain calibration. This variability could explain some degree of variability seen in the

RBC:barrier on repeat scans. ***Secondly***, the ratio calculation is predicated on equal excitation of the RBC and barrier resonances. But this can be undermined by distortion of the RF pulse frequency profile due to non-linearity of the power amplifier. In our system we estimate this to result in application of a marginally (6%) lower flip angle on the RBC than the barrier resonance. However, the impact of such imperfection is not immediately clear as it causes less depletion of the RBC magnetization, but also less excitation; these two effects would cancel. In any case, it should be possible to create a distortion-free selective RF frequency profile, as demonstrated by Leung *et al.*, using phase modulated composite RF pulses (135). However, none of the RF effects discussed above are expected to change the relative differences we observed in IPF vs. healthy volunteers; they would only impact the absolute magnitude of RBC:barrier obtained across different MRI systems. Furthermore, in this preliminary study, subject hematocrit was not measured. We speculate that the hematocrit will positively correlate with the RBC:barrier ratio. Thus, future studies should consider correcting spectroscopic metrics for potential disease-induced variations in hematocrit (136), and ensure that the RBC:barrier ratio is truly indicative of diffusion limitation. ***Lastly***, we note that RBC:barrier in patients with significant lung disease could be affected by heterogeneity of ventilation (137) and diffusion-perfusion ratios (138). The heterogeneity in ventilation has been shown to change DL_{CO} measurements by ~6% (137). Also, as the uptake of CO is dictated by the regional diffusion-perfusion ratio (138), changes in regional perfusion will impact the uptake of ^{129}Xe in the RBCs.

6.5. Summary

This study has confirmed our hypothesis that spectroscopic interrogation of dissolved-phase HP ^{129}Xe can detect diffusion impairment in subjects with IPF. These patients exhibited an RBC:barrier that was 3.3-fold lower than for healthy volunteers and this ratio was strongly correlated with the well-established DL_{CO} measure of gas-exchange. Given its excellent sensitivity to diffusion impairment, this metric can lend itself to longitudinal assessment of lung function and analyze response to a potential therapy. Moreover, the ability to detect variations in RBC:barrier dynamically, during breath-hold and exhalation, provides a fundamentally novel means to study gas exchange dynamics, and further improves the specificity of the technique to differentiate pulmonary diseases. Additionally, ^{129}Xe transfer spectroscopy provides intriguing complementary information, via the oxygenation-dependent frequency of the RBC resonance, as well as the line widths of all three resonances. However, further studies are needed to better understand the degree to which RBC:barrier and all other parameters reported here depend on lung inflation and capillary blood volume. Methods must be developed to ensure that the ratio is measured in a way that is maximally reproducible, not only at a given imaging site, but across centers. While the work in this chapter measures gas-exchange on a global basis, this measurement forms the fundamental basis for the next chapter, which extends this technique to create three-dimensional images of the transfer of ^{129}Xe exclusively to the RBC.

7. Imaging ^{129}Xe in the Gas-phase, Barrier and the RBCs in a Single Breath

The results presented in this chapter were recently submitted as a journal article: S.S. Kaushik *et al.*, '*Single-Breath Imaging of Hyperpolarized ^{129}Xe in the Airspaces, Barrier, and Red Blood Cells using an Interleaved 3D Radial 1-Point Dixon Acquisition*', Magnetic Resonance in Medicine, 2014.

7.1. Motivation

The spectroscopic studies of patients with idiopathic pulmonary fibrosis (IPF) presented in **chapter 6**, showed the importance of separating ^{129}Xe transfer into its barrier and RBC constituents. Global gas-transfer spectra demonstrated that the ratio of ^{129}Xe uptake in the RBCs vs. barrier was 3.3-fold lower in IPF patients than in healthy volunteers. Additionally, this ratio correlated well with conventional physiologic measurements of gas exchange (DL_{CO} correlation = 0.89), provided dynamic spectroscopic information, and in healthy subjects, the RBC:barrier was sensitive to changes in capillary blood volume and alveolar pressure. Beyond the overall uptake ratios, the frequency of ^{129}Xe in the RBC compartment appeared to reveal sensitivity to oxygenation at the alveolar capillary level. Hence, based on these results, individually visualizing the RBC and barrier compartments could provide fundamental insights about regional gas-exchange.

Separating ^{129}Xe uptake in the barrier and RBCs shares many similarities to the more familiar problem of fat-water separation in ^{1}H MRI (139). Like fat and water, which at 1.5 T are separated by ~220 Hz, ^{129}Xe in the barrier and RBC compartments are separated by ~340 Hz. However, unlike ^{1}H in fat and water, ^{129}Xe in the RBC and barrier experience a very short T_2^*, which constrains the available time for typical, well-known Dixon techniques. Therefore, early efforts to generate separate images of ^{129}Xe in the barrier and RBCs in a rat model of fibrosis utilized the simpler 1-point Dixon technique (47). This approach acquires images at an echo time such that when the center of k-space is sampled, the two resonances are 90° out of phase. By subsequently phase-shifting the image, ^{129}Xe signal from the RBC and barrier components are largely confined to the real and imaginary receiver channels. This first study generated only 2D projection images, but the approach was recently extended to acquire fully 3D isotropic images of the two compartments in a rat model of late-stage fibrosis (48). Both studies showed that while the ^{129}Xe uptake in the barrier compartment was largely unaffected, ^{129}Xe uptake in RBCs was markedly reduced in fibrotic regions.

A significant advance in translating ^{129}Xe gas-transfer clinically was recently made by Qing *et al.*, who separated the barrier and RBC images using the hierarchical IDEAL algorithm (49). This extension of the original IDEAL algorithm allows data to be acquired at multiple (and arbitrary) echo times, while the B_0 inhomogeneity is iteratively calculated and removed at multiple resolution levels to enable the RBC and barrier images to be decomposed. However, one challenge of the IDEAL algorithm is that it requires images to be acquired at 3 echo times (TEs). Acquiring dissolved ^{129}Xe signal at longer TEs is challenging given the short T_2*. However, Qing *et al*. overcame this by employing very high ^{129}Xe polarizations and demonstrated well-separated images that correlated well with global spectroscopic measures (49).

This chapter presents the simulation and phantom based initial validation, and the ultimate clinical translation of the 1-point Dixon approach to separately image ^{129}Xe in the barrier and the RBCs using only a single, sub-millisecond TE. Such short TEs are more robust against T_2^* blurring and enable sampling more of k-space within a single breath-hold. By further acquiring an interleaved gas-phase image, we can image all three compartments in a single breath-hold. The availability of the gas image, allows B_0 inhomogeneity to be removed by using this image to calculate a phase map. To serve as an initial test of the 1-point Dixon method, the images were acquired in healthy volunteers and patients with IPF. This patient population is advantageous for several reasons. First, as already shown by ^{129}Xe spectroscopy, IPF patients exhibit a significant diffusion limitation caused by interstitial thickening of the blood-gas barrier, which reduces ^{129}Xe uptake in RBCs (140). Hence, ^{129}Xe gas-transfer to RBCs was expected to exhibit focal gas transfer defects. Moreover, patients with IPF exhibit features of traction bronchiectasis, honeycombing, reticular and ground glass opacities, and consolidation in their CT images, providing a means to conduct some qualitative validation of the 1-point Dixon imaging approach.

7.2. 1-point Dixon Simulations

As seen in **chapter 6**, the regions of fibrosis and interstitial inflammation seen in subjects with IPF, should limit the diffusion of ^{129}Xe to the RBCs. With a proper choice of acquisition parameters, these regions in the ^{129}Xe-RBC images are expected to show gas-transfer 'defects'. However, the ability to visualize such defects using the 1-point Dixon technique depends on a couple of factors. a) *The echo time needed for a 90° phase separation should be accurately calibrated*. b) *The Dixon condition is valid only at the center of k-space (k_0), beyond which the RBC-barrier phase difference continues to evolve. The acquisition should be rapid enough to minimize the impact of this continued phase accumulation*. The simulation presented in this section tests how perfect these conditions have to be to still visualize defects in the ^{129}Xe-RBC image.

7.2.1. Methods

The simulations were implemented in Matlab. A 3D mathematical phantom was used, and the source code for this phantom was made available by Jeff Fessler from the

University of Michigan. The building blocks of the phantom are the mathematical definitions for common shapes (circle, cylinder, rectangle, ellipse, and triangle). By specifying the dimensions of these shapes, their centroid, and signal intensity, an image of the phantom can be obtained by calculating the sum of the signal intensities of the specified shapes. The primary advantage of using this approach is in obtaining its frequency information. As the phantom is mathematically defined by the various shapes, this k-space data is obtained by evaluating the Fourier transform at the specified coordinates. Hence, even if k-space were radially sampled, the frequency data will be truly representative of the underlying phantom, as it has the advantage of not needing any interpolation.

The 3D phantom was defined to have complex data, with the real data representing the red blood cells, and the imaginary data representing the barrier. This ensured that the real and imaginary channels were inherently 90° out of phase. With a field of view of 40 cm, the phantom was defined to be a cylinder in both channels, with a radius of 15 cm, and a length of 30cm. To mimic the RBC:barrier ratio in healthy volunteers, the signal intensity for the real data in the phantom was 0.5, and the imaginary data was set to 1i. For the real component of the phantom alone, a number of 3x3x30 cm^3 cuboids were used to define the gas-transfer defects. The phantom was treated as a 64^3 matrix and the real and imaginary components of this phantom are shown in **figure 47**.

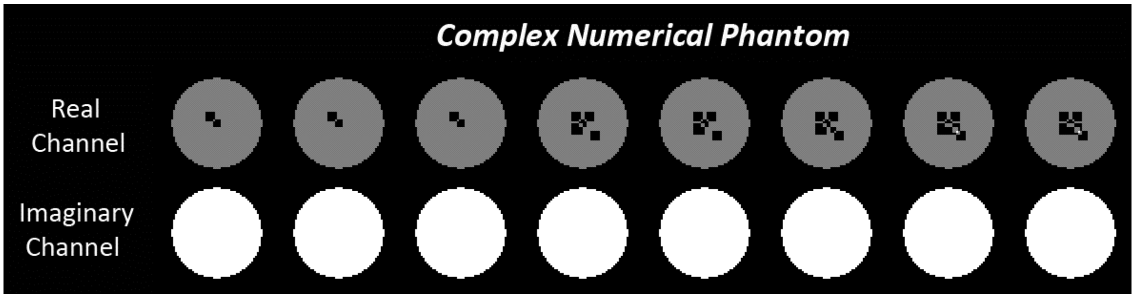

Figure 47: Real and imaginary channels of the 3D numerical phantom showing the defects in the real channel which mimics the defects in the transfer of ^{129}Xe to the RBCs.

The k-space data for this phantom was sampled using a golden-means sampling strategy, with 4289 frames, which has the same 3× under-sampling factor used for the clinical dissolved-phase ^{129}Xe images. This k-space data was then reconstructed onto a 128^3 matrix, using a NUFFT algorithm. **Figure 48** shows a single slice of this phantom with the defects, and the reconstructed image.

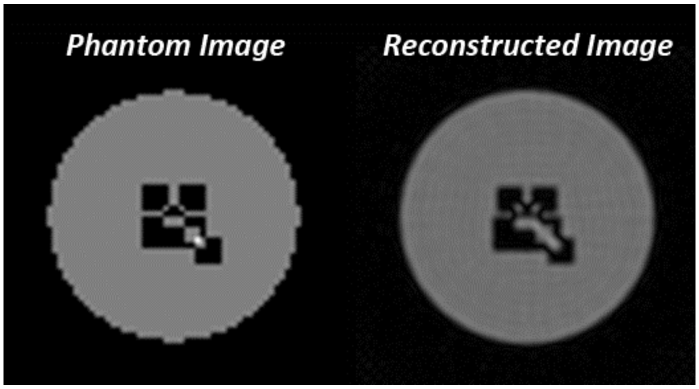

Figure 48: Single slice of the real channel of the numerical phantom and the reconstructed image.

We first sought to test the impact of continued phase accumulation beyond k_0 on the Dixon images. This phase accumulation will depend on a) sampling speed (dwell time), which is a function of the receiver bandwidth (BW) and is given as $dwell = \frac{1}{2BW}$, and b) the RBC-barrier frequency difference (Δf). Hence, with large frequency differences and large dwell times, over the course of sampling a ray of k-space, the RBC-barrier phase accumulation will increase significantly beyond 90°. This phase accumulation is assumed to occur independent of the gradients, and is modeled as a phase vector (φ) as shown in equation 7.1.

$$\varphi(t, \Delta f) = e^{unwrap\left(i2\pi\Delta f t\right)} \tag{7.1}$$

where t is the time vector such that $t = n \times dwell$, where n is the k-space sample point n=1,2,..64. As the phase accumulation will be well beyond 180° for longer dwell times, the phase in the exponent was subject to an unwrapping operation. This phase accumulation was further weighted down by the T_2* of the dissolved-phase. As the matrix size was twice that of a typical dissolved-phase acquisition (64^3 vs. 32^3), the T_2* was chosen to be 4 ms instead of 2 ms. The weighted phase equation can be written as shown below, and this was multiplied with each ray of k-space.

$$\varphi_W(t, \Delta f) = \varphi(t, \Delta f) e^{-t/T_2^*} \tag{7.2}$$

To visualize the impact of dwell time, and hence phase accumulation beyond k_0, the images were reconstructed at multiple dwell times ranging from 8 – 64μs. **Figure 49** shows a single slice of the 3D phantom, reconstructed at these dwell times. By acquiring 64 points along a ray of k-space, with a dwell time of 8μs, the phase difference increases by an additional 63°. Hence, while the real and imaginary data are 90° out of phase at k_0, at the end of k-space, they have a phase difference of 153°. In spite of this phase accumulation, the rapid T_2^* works to attenuate the later points of k-space, and we can still visualize the defects in the image. However, with an increase in dwell time, this phase accumulation worsens, and while we can somewhat visualize the defects at a dwell time of 64μs, the image quality worsens. Hence, for 64 points along a ray of k-space, a dwell time of 8-16μs would be ideal to ensure that the continued phase accumulation has a minimal impact on the ability to identify defects. However, such small dwell times require large receiver bandwidths, which will significantly increase the noise in the images. Hence, the dwell time should be long enough to minimize image noise, and short enough to minimize the accumulation of phase beyond k_0.

The previous tests were done assuming that the RBC and barrier are exactly 90° out of phase at the start of the acquisition, that is, the TE_{90} is accurate. To test the impact of the errors in the TE_{90} on visualizing the defects, with a constant dwell time of 16μs, the images were reconstructed at different phase offsets ranging from 70 – 105°. A phase separation of 70° is indicative of starting the acquisition with the $\mathrm{TE}<\mathrm{TE}_{90}$, whereas a separation is 105° would be an example of $\mathrm{TE}>\mathrm{TE}_{90}$. These phase offsets refer to the phase difference at k_0, and were achieved by phase shifting the k-space k(x,y) as shown

$$k_p(x,y) = k(x,y)e^{\left(i\frac{\pi}{180}\Delta\phi_{off}\right)} \tag{7.3}$$

where $\Delta\phi_{off}$ ranged from -20° to 15°. One slice of the reconstructed images is shown in **figure 49** below.

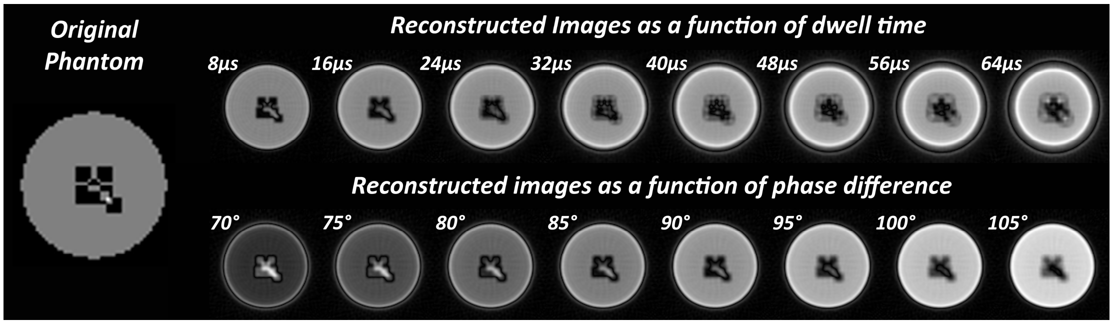

Figure 49: The real portion of the phantom is used to show the impact of continued phase accumulation (above) and the impact of phase separation (below) on the ability to visualize gas-transfer defects using the 1-point Dixon acquisition. Increased dwell times significantly degrade image quality. Echo times that are shorter than TE_{90} will result in lower phase separation between the two resonances, and defects are completely obscured. Defects can still be seen with larger echo times, where the phase separation is greater than 90°, but the signal intensity in the rest of the phantom is contaminated by the signal from the imaginary channel.

Even with the lower phase difference (<90°) at k_0, the general shape of the gas-transfer defect is largely retained. However, a portion of the imaginary channel crosses over into the real channel, increasing the signal within the defects seen in the center of the image. In contrast, the images reconstructed at a higher phase difference (>90°), seem to retain the defects in the image, but show higher signal in the rest of the image, which is indicative of contamination from the data in the imaginary channel.

Based on these simulation results, one can conclude that the impact of the continued phase accumulation beyond k_0 is dampened by the rapid T_2^* of the dissolved-phase. Hence with a moderately fast acquisition, this effect can be minimized. As for TE_{90}, it is imperative that its calculation be accurate. But qualitatively, based on the images in **figure 49**, one can tolerate an error of ±5° in the phase difference at k_0.

7.3. Phantom Experiments

As a proof-of-principle experiment, the 3D extension of the 1-point Dixon technique was implemented on a 2T scanner, using a water-cyclohexane phantom. Cyclohexane was chosen to imitate the 'fat' peak, as it consists of only a single resonance, and more importantly, has a similar chemical shift. The water-cyclohexane phantom was made using a ping-pong ball filled half-way with 5 mM copper sulphate solution and the remaining was topped off with cyclohexane. As shown in the spectrum in **figure 50A**, the frequency difference between water and cyclohexane on a 2T was roughly 251 Hz (~3 ppm). Based on the formula presented in **chapter 2**, this frequency difference should let us calculate the echo time needed for a 90° phase separation (TE_{90}). Assuming no RF based phase accumulation, this theoretical echo-time for the water-cyclohexane phantom was 996 μs. To validate this echo time, water-cyclohexane spectra were acquired at 5 echo times. These spectra were curve fit (as discussed in **chapter 6**) to extract the phase difference between the resonances. This phase difference was plotted as a function of echo time, and linear regression was used to determine the empirical TE_{90}. Interestingly, this empirical TE_{90} was calculated to be 469 μs, which was 527 μs shorter than the theoretical estimation. This is shown in **figure 50B**. This result indicates that the phase accumulation during the RF pulse is not negligible, and hence, the theoretical calculation of TE_{90} is not valid. Thus, the TE_{90} for the phantom experiment, and the subsequent clinical translation (to be discussed in following sections), was calculated empirically.

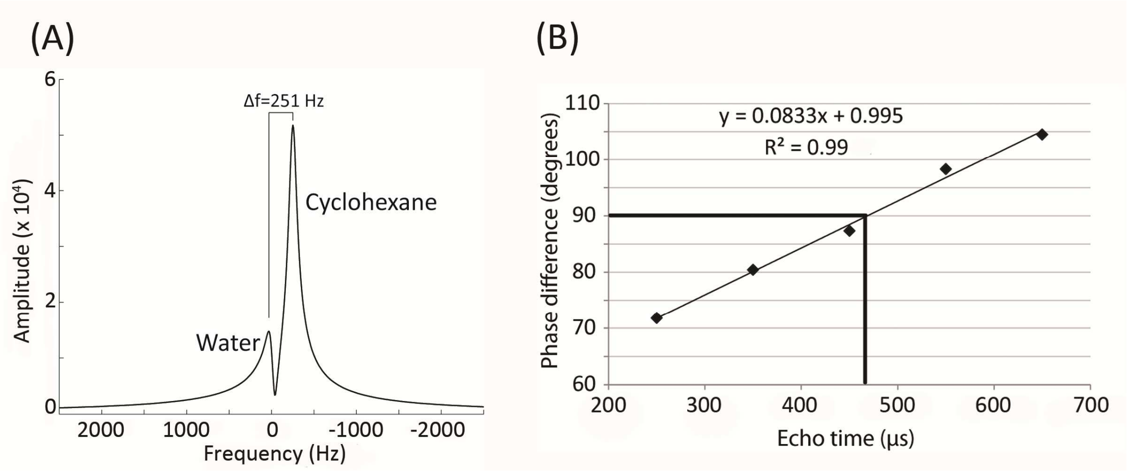

Figure 50: (A) Spectrum from a water-cyclohexane phantom obtained on a 2T system. (B) Empirical calculation of the TE_{90}. Compared to the theoretical value for 250 Hz frequency separation, the empirical TE_{90} was 527 μs shorter.

While the two resonances may be 90° out of phase at the calculated TE_{90}, they may land on the transverse plane at an arbitrary phase with respect to the receiver. To determine this receiver phase offset, an additional reference spectrum was acquired at the TE_{90}, which was subjected to the same curve fitting procedure to extract the phases of the individual resonances. Subsequently, images of the water-cyclohexane phantom were acquired with the echo-time set to 469 μs. The acquisition parameters were: Sinc pulse duration = 1200 μs, matrix = 64×64×64, field of view = 6 cm, number of views = 12901, TE/TR = 0.469/2000 ms, gradient ramp time = 4 μs, receiver bandwidth = 31.25 kHz. The images were reconstructed using a gridding algorithm. Post reconstruction, the images were re-phased to correct for the receiver phase-offset determined from the reference spectrum, which resulted in the real and imaginary portions of the image representing the water and cyclohexane respectively. **Figure 51A** shows the magnitude image, and the real and imaginary images are shown in **figure 51B**.

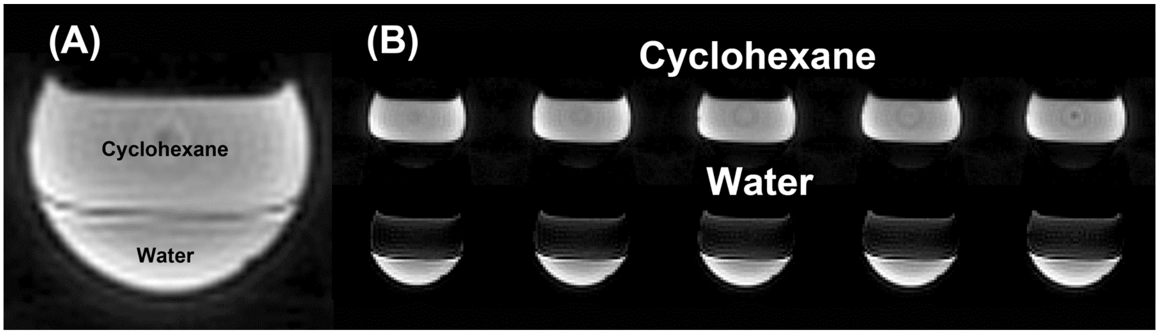

Figure 51: 1-point Dixon images obtained using the water-cyclohexane phantom. (A) Magnitude image showing the water at the bottom and cyclohexane floating on top. (B) The real and imaginary channels show the water and cyclohexane images respectively. The real channel still contains a little cyclohexane signal, which is contributed by the longer cyclohexane T_1 and continued phase accumulation.

As shown in **figure 51**, high quality images of both water and cyclohexane can be generated using the 3D 1-point Dixon acquisition. The residual cyclohexane signal seen in the water image can be explained in part, by virtue of cyclohexane's longer T_2 relaxation time (~3 s). Also, the Dixon condition is truly satisfied only at the center of k-space (k_0). In spite of the faster ramp-times (4 μs) and higher bandwidth used to ensure a faster sampling of k-space, this minimizes, but does not completely eliminate the accumulation of phase during data acquisition. However, in spite of this minor drawback, these results, in conjunction with the results of the simulations, show promise in the clinical viability of the 1-point Dixon acquisition.

7.4. Clinical translation

The simulations and phantom experiments have demonstrated that the 1-point Dixon acquisition is indeed feasible. This section deals with the translation of this approach to the clinic, to create images of ^{129}Xe in the airspaces, barrier and the RBCs, in a single breath hold.

7.4.1. Subject Inclusion and Exclusion Criteria

Studies were approved by the Duke Institutional Review Board and were conducted under IND 109,490. Written, informed consent was obtained from all subjects prior to the scan. Data was acquired in 4 healthy volunteers, and 3 subjects with idiopathic pulmonary fibrosis (IPF). All subjects were at least 18 years of age (healthy volunteers – 3 men, 1 woman, age = 44.0 ± 19.4 years; IPF subjects – 3 men, age = 64.7 ± 8.7 years). The healthy volunteers had less than a 5 pack-year smoking history, had not smoked in the last 5 years, and had no diagnosed pulmonary disorders. Subjects were excluded if they had a history of cardiac arrhythmias, were pregnant or lactating, or had a respiratory illness within 30 days of MRI.

7.4.2. ^{129}Xe Polarization and Delivery

Isotopically enriched ^{129}Xe (85%) was polarized to 7 – 10% by rubidium-vapor spin-exchange optical pumping (141) using a commercially available polarizer (Model 9800, Polarean, Inc., Durham, NC). Xenon was cryogenically accumulated and thawed into a Tedlar bag and polarization was determined using a polarization measurement station (Model 2881, Polarean, Inc.). Prior to gas inhalation, the subjects were instructed to inhale to total lung capacity and exhale to functional residual capacity twice. Subsequently, the contents of the bag were inhaled via a mouthpiece connected to the bag through a 6-mm ID Tygon tube, and the subjects held their breath for the duration of the scans (13 – 15 s). As explained below, to establish the correct echo time for Dixon imaging, subjects first underwent a calibration scan, where they received a mixture of 400 ml of HP ^{129}Xe and 600 ml of ultra-high-purity N_2. For the subsequent gas-transfer image, subjects received a 1-L dose of HP ^{129}Xe. The subject's heart rate and oxygen saturation were monitored using an MR-compatible monitoring system (GE Healthcare, Helsinki Finland).

7.4.3. Image Acquisition and Reconstruction

The 1-point Dixon acquisition requires solving three problems. First, it is necessary to find the echo time, $TE_{90,}$ at which the RBC and barrier resonances are 90° out of phase. Second, the image must be phase-shifted such that the RBC-dominant signal becomes aligned with the in-phase channel of the scanner, and the barrier-dominated image is aligned with the quadrature channel. And finally, once the images have been phase-shifted, they must be further corrected for any phase variation caused by B_0 inhomogeneity. These steps are achieved as follows.

7.4.3.1. Calibration spectra to determine TE_{90}

In principle, the TE_{90} can be simply calculated by allowing the phase difference to accumulate based on the known RBC-barrier frequency difference (Δf), given by $TE_{90} = \frac{1}{4\Delta f}$. Hence, after application of a hypothetical infinitely short pulse, a frequency difference of 340 Hz would yield an expected TE_{90} = 735 µs. However, because the RF pulse used to selectively excite dissolved phase ^{129}Xe is relatively long (1.2 ms), significant phase evolution occurs before the magnetization reaches the transverse plane. Moreover, it has been shown that the TE_{90} varies across individual subjects with fibrosis and inflammation because a variable degree of ^{129}Xe compartmental exchange occurs between the barrier and RBC (48). Hence, for each subject in our study the TE_{90} was empirically determined as outlined in **Figure 52A**. In a single breath, dissolved-phase spectra were acquired at four progressively longer echo times of 275, 375, 475, and 575 µs. (Note: echo time has been defined from the end of the 1.2-ms 3-lobe sinc pulse to acquisition of the first data point.) The other acquisition parameters were: number of points = 512, flip-angle = 22°, TR = 50 ms, NEX = 50. After acquisition of each spectrum, crusher gradients (amplitude = 3.3 G/cm, total duration = 3 ms) were played out on all three gradient axes to de-phase the long-lived off-resonance gas-phase signal. Once dissolved-phase spectra had been acquired, transmit and receive frequencies were changed to the gas-phase resonance (-3832 Hz) and a single gas-phase reference spectrum was acquired at TE = 275 μs.

The data were processed using routines written in MATLAB (The MathWorks, Inc., Natick, MA). The first 25 FIDs at each TE were discarded to avoid the presence of "downstream magnetization" from ^{129}Xe beyond the capillary beds, in the larger vasculature, as well as to reset the magnetization in the barrier and RBCs for later quantification. The remaining 25 FIDs were averaged, exponentially line-broadened by 50 Hz, and Fourier transformed to generate a dissolved-phase spectrum with a small gas-phase reference peak. The complex spectrum was then fit using a non-linear least squares optimization algorithm to a sum of Lorentzian and Dispersive functions to extract the amplitude, frequency, width, and phase of each resonance at each TE (140). The RBC-barrier phase-difference at each TE was fit by linear regression to determine the TE_{90}. Additionally, the spectrum acquired at a TE of 275 μs was used to calculate the area under the curve of each resonance, which was then used to calculate the ratio of the RBC and the barrier signals (RBC:barrier). As described later, this ratio was used in calculations that determine the phase offset used to align the RBC and barrier components of the dissolved-phase image to the real and imaginary channel.

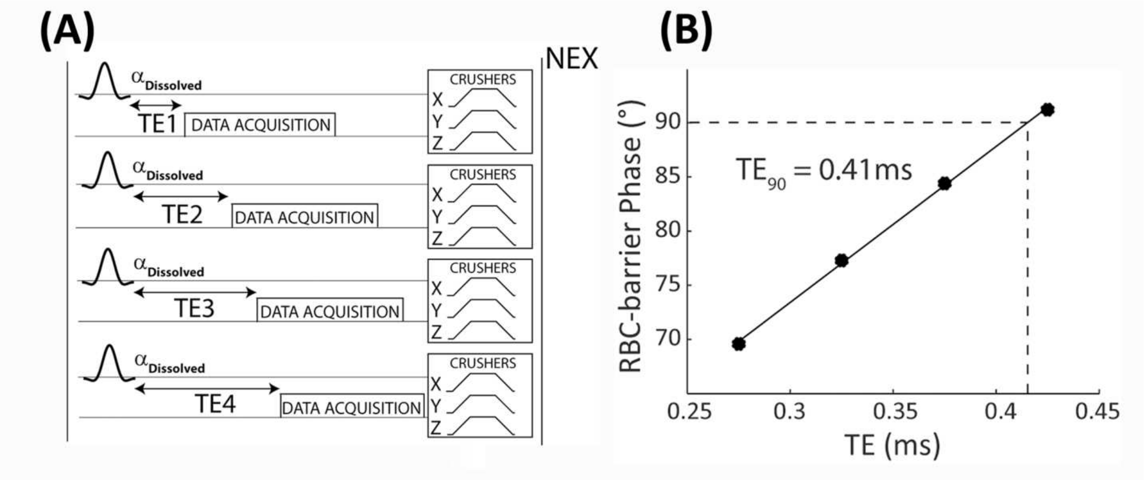

Figure 52: The phase calibration scan shown in (A) acquires dissolved-phase ^{129}Xe spectra at 4 echo times (275, 375, 475, 575 μs) with a NEX of 50. Crusher gradients are played out on all three gradient axes to de-phase any off-resonant gas-phase signal. The last 25 dissolved-phase FIDs are averaged together and fit to a sum of Lorentzian and Dispersion functions to extract the phase difference between the RBC and barrier resonances. These phase differences are plotted as a function of echo time (B) and fit to a line to calculate the TE_{90}.

7.4.3.2. Image acquisition and workflow

Images were acquired on a 1.5-T scanner (GE EXCITE 15M4). Subjects were fitted with a quadrature vest coil tuned to the ^{129}Xe resonance frequency at 17.66 MHz (Clinical MR Solutions, Brookfield, WI). The coil was proton-blocked to enable ^{1}H imaging with the scanner's body coil.

Single-breath gas and dissolved-phase images were acquired during a 15-s breath-hold using 1-L of HP ^{129}Xe and a 3D radial sequence (119). Dixon images were acquired with the echo time set to TE_{90}. Transmit and receive frequencies were alternated between the gas and RBC resonance (+3832 Hz) to acquire each radial ray of k-space, which were distributed pseudo uniformly in both k-space and time using a 3D golden-means sampling strategy (49,142). [Acquisition parameters: 1200-μs sinc pulse, matrix=32×32×32, flip-angles = 0.5/22°, number of rays = 2002 (1001 each resonance), FOV = 40 cm, TE/TR = TE_{90}/7.5 ms, receiver bandwidth = 15.625 kHz]. The data were then split and separately reconstructed onto a 64×64×64 matrix using a NUFFT reconstruction algorithm (99) to generate isotropic, 3D gas and dissolved-phase images.

To help delineate the thoracic cavity a 3D radial ^{1}H image was acquired over the course of a separate 15-s breath-hold. In order to achieve approximately the same lung inflation as during the ^{129}Xe scan, the subject inhaled 1L of air from a polyethylene bag. These images were acquired using: 274-μs hard pulse, TE/TR = 0.199/2.4 ms, matrix = 64×64×64, frames = 5647, 512 dummy pulses, flip-angle = 5°, bandwidth = 15.625 kHz, and FOV = 40 cm.

7.4.4. Image Processing and Analysis

7.4.4.1. Image registration and segmentation

In order to confine the analysis to the thoracic cavity, the ^{1}H images were registered to the ^{129}Xe gas-phase images via a multi-resolution affine transformation using the Image Registration Toolkit (101). The registered ^{1}H images were then segmented using seed-based region growing using 3DSlicer (36) to generate the thoracic cavity mask. The thoracic cavity mask was morphologically closed using a spherical structuring element with a 7-voxel diameter. The mask was further 'filled' to remove any additional holes in the mask, and was then manually segmented to remove the major airways in MATLAB.

7.4.4.2. Determining the receiver phase offset

Although imaging at TE_{90} ensures that RBC and barrier signals are 90° out of phase relative to one another, the two compartments are not necessarily aligned with the real and imaginary channels because the scanner imparts an arbitrary phase shift ϕ_0 to the data. Assuming the images were acquired at exactly TE_{90}, the signal at k_0 can be written as

$$S(t=0) = (S_{RBC} + iS_{Barrier})e^{i\phi_0} \tag{7.4}$$

Applying a phase shift, $\Delta\phi$, that is exactly opposite to ϕ_0 would align the RBC and barrier signals with the real and imaginary channels, but unfortunately ϕ_0 is not known a priori. Applying $\Delta\phi$ yields a signal

$$S(t=0) = (S_{RBC} + iS_{Barrier})e^{i(\phi_0+\Delta\phi)} \tag{7.5}$$

We now use the additional constraint that when the correct phase shift $\Delta\phi$ has been applied, the sum total RBC:barrier within the thoracic cavity obtained from imaging, must be the same as that measured by spectroscopy (140). We designate this ratio as R for brevity, and solve for $\Delta\phi$ using $S_{\mathrm{Re}}(\Delta\phi)/S_{im}(\Delta\phi) = R$. To compute the real to imaginary ratio from the phase-shifted image, we expand the complex signal in Equation 2 into its real (S_{Re}) and imaginary (S_{Im}) components. By defining $S_{RBC}=R\times S_{barrier}$, the resulting ratio of the real and imaginary image data within the thoracic cavity can then be written as a function only of the phase shift $\Delta\phi$ applied, and the ratio R.

$$\frac{S_{\mathrm{Re}}(\Delta\phi)}{S_{\mathrm{Im}}(\Delta\phi)} = \frac{R\cos(\phi_0+\Delta\phi)-\sin(\phi_0+\Delta\phi)}{R\sin(\phi_0+\Delta\phi)+\cos(\phi_0+\Delta\phi)} \tag{7.6}$$

Note that when the correct phase shift $\Delta\phi=-\phi_0$ has been applied, Equation 3 reduces to $S_{Re}/S_{Im}=R$, as required. This phase shift $\Delta\phi$ was determined by plotting S_{Re}/S_{Im} over a range of receiver phase offsets $[0, \pi]$ and fitting it to Equation 3 using a non-linear least squares optimization algorithm. The dissolved image was then phase shifted by $\Delta\phi=-\phi_0$ to isolate the RBC image to the real channel, and the barrier to the imaginary channel of the receiver.

7.4.4.3. Correcting for local phase inhomogeneity

The acquisition described thus far assumes that the only source of phase evolution between RBC and barrier is their frequency difference. However, phase differences can also be imparted by B_0 inhomogeneity, which must be corrected. Fortunately, the inherently co-registered gas-phase ^{129}Xe image is comprised of only a single resonance and therefore, any phase variation in the gas-phase image is largely attributable to B_0 inhomogeneity. Because gas-phase images were acquired at only a single echo time, a phase-map was first generated, and then its mean was subtracted to create a 'differential phase map'. This differential phase map was then applied on a pixel-by-pixel basis to the phased dissolved images for B_0 inhomogeneity correction of the RBC and barrier images.

7.4.4.4. Maps of lung function

In addition to the native ^{129}Xe-barrier and ^{129}Xe-RBC images, several additional maps were found to be helpful in visualizing regional function. First, analogous to the spectroscopic RBC:barrier ratio, the RBC image was divided by the barrier image on a voxel-by-voxel basis to create an RBC:barrier map. Similarly, to gauge subtle differences in the RBC and barrier intensity, the RBC and barrier images were divided by the gas-phase images to yield the barrier:gas and RBC:gas maps (49). To prevent long high-intensity tails in these maps, they were scaled by the 99th percentile of their cumulative distribution function (143) to limit the range between 0 and 1.

Similar to ventilation images, the ^{129}Xe-RBC gas-transfer images were expected to show regional gas-exchange defects in areas of fibrosis, and therefore gas-transfer defect maps were also generated. The ^{129}Xe-RBC images were first thresholded to create an RBC mask. The threshold was chosen from a slice that purely depicted the background signal. The resulting RBC mask was subtracted from the thoracic cavity mask to yield the gas-transfer defect map. The volume of gas transfer defects was divided by the thoracic cavity volume to calculate the gas-transfer defect percentage.

7.4.5. Study Results

Single-breath images of ^{129}Xe in the gas and dissolved-phases were successfully acquired in all the subjects scanned. The dissolved-phase images were then decomposed into the ^{129}Xe-barrier and ^{129}Xe-RBC images. Subject demographics are summarized in **table 9**, along with spectroscopic and imaging-derived RBC:barrier ratios, RBC-barrier frequency differences, and the TE_{90}.

Table 9: Subject demographics, spectroscopic and imaging-derived parameters.

Subject #	Age (years)	RBC:barrier		Δf (Hz)	TE_{90} (μs)
		Spectroscopy	Imaging		
Healthy Volunteers					
1	56	0.49	0.48	349.9	411
2	65	0.53	0.52	328.9	407
3	29	0.46	0.47	323.0	470
4	26	0.64	0.63	330.1	427
IPF Subjects					
1	72	0.16	0.17	311.8	285
2	67	0.16	0.18	303.4	163
3	55	0.14	0.14	307.5	256

As seen by the variability in TE_{90} and lack of correlation to RBC-barrier frequency difference, the phase calibration scan was important to accurately calculate the TE_{90} for each subject. Interestingly, although the RBC-barrier frequency difference was 40 Hz smaller in the IPF group than the healthy group, the TE_{90} was actually shorter in the IPF group than in the healthy group (0.24 ± 0.06 ms for IPF, 0.43 ± 0.03 ms for healthy). As shown in **Figure 52B**, increasing TE resulted in a commensurate linearly increasing phase difference between the RBC and barrier resonances, as expected. For healthy volunteers, the relative phase accumulation with TE (slope) agreed reasonably well with theoretical predictions (132.6 ± 4.7° ms^{-1} vs 119.8 ± 4.2° ms^{-1} expected). The IPF patients, despite exhibiting a smaller RBC-barrier frequency difference, experienced a rate of phase accumulation that was slower than expected (155.5 ± 18.2° ms^{-1} vs 110.7 ± 1.5° ms^{-1} expected). Additionally, the linear regression of differential RBC-barrier phase as a function of TE yielded a negative intercept for all subjects; the intercept was moderately lower in the healthy volunteers (-46.3 ± 5.6°) than in the IPF subjects (-39.5 ± 15.7°).

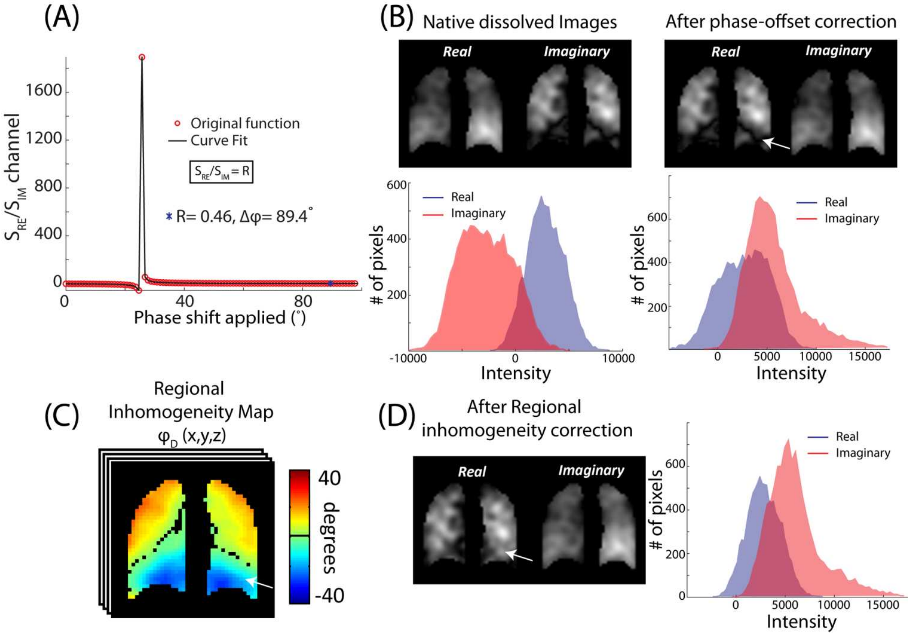

Figure 53: Phase correcting the dissolved-phase images. (A) shows the ratio of the sum of the real and imaginary channels as a function of receiver phase applied. For this subject, a receiver phase offset of -89.4° makes the ratio of real and imaginary channel signals equal to the spectroscopic ratio R=0.46. (B) shows magnitude images of the real and imaginary channel after applying the calculated receiver phase offset. As shown by the white arrow, this subject exhibits a low intensity stripe at the base of the lung in the real channel. This may be partly caused by the abrupt change in the

regional phase as shown by the difference phase map (C). Once the regional inhomogeneity was applied, this apparent defect was removed (D). Additionally, the negative values seen in the histogram after applying the phase offset (B) have been largely minimized after regional inhomogeneity correction (D).

The calculation of phase shifts and their effects on the real and imaginary images are shown in **Figure 53**. The calculation of the overall phase shift is illustrated in **Figure 53A**. For this healthy subject with *R*=0.46, a phase shift of $\Delta\varphi$ = 89.4° (inset) was needed to match the image-derived S_{Re}/S_{Im}=0.46, to the spectroscopically-derived RBC:barrier ratio. After applying only the -89.4° phase shift, the real channel exhibits an apparent 'defect' in the basal portion of the left lung (white arrow in **Figure 53B**). However, this apparent defect can be seen to originate from B_0 inhomogeneity shown in **Figure 53C**, which shows the spatial phase variation seen in the single-resonance gas-phase image. The phase map ranged from about -45° to 45° across the lung, with the highest phase accumulation observed in the basal lung near the diaphragm. After correcting for this B_0 inhomogeneity, the low intensity region previously present in the real channel image at the base of the lung has resolved (**Figure 53D**). Despite the visually apparent change in real and imaginary signal distribution seen in **Figure 53**, phase correction only increased the image-derived RBC:barrier ratio minimally (0.46 to 0.47). In fact, the RBC:barrier ratio after phase-map correction decreased by only -0.99 ± 1.51% in healthy subjects. For the IPF subjects, phase-map correction caused the RBC:barrier ratio to increase slightly (4.59 ± 2.86%).

Figure 54 shows fully phase-corrected Dixon images depicting the ^{129}Xe-barrier and ^{129}Xe-RBC uptake along with the gas-phase ^{129}Xe distribution in a healthy volunteer and subject with IPF. For the healthy volunteer, all three images are largely homogeneous with the signal intensity increasing moderately in the dependent lung. For the IPF subject, while the ventilation and barrier images are similarly homogenous, the signal intensity of the RBC images is generally lower, and the images show widespread signal voids, or gas-transfer defects. Interestingly, these gas-transfer defects in the RBC channel were present even in regions with seemingly normal gas-phase and barrier signal. Although gas-transfer defects were far more prominent in the IPF subject, the healthy volunteer also exhibits some defects in the RBC map, most of which are located in well ventilated regions. The gas-transfer defect percentage was 5.6 ± 0.7% in the healthy volunteers, with these defects were predominantly located in the anterior, non-dependent portion of the lung. By contrast for the IPF subjects, the gas transfer defect percentage was 4-fold higher (22.7 ± 6.3%), and these defects were distributed throughout the lung.

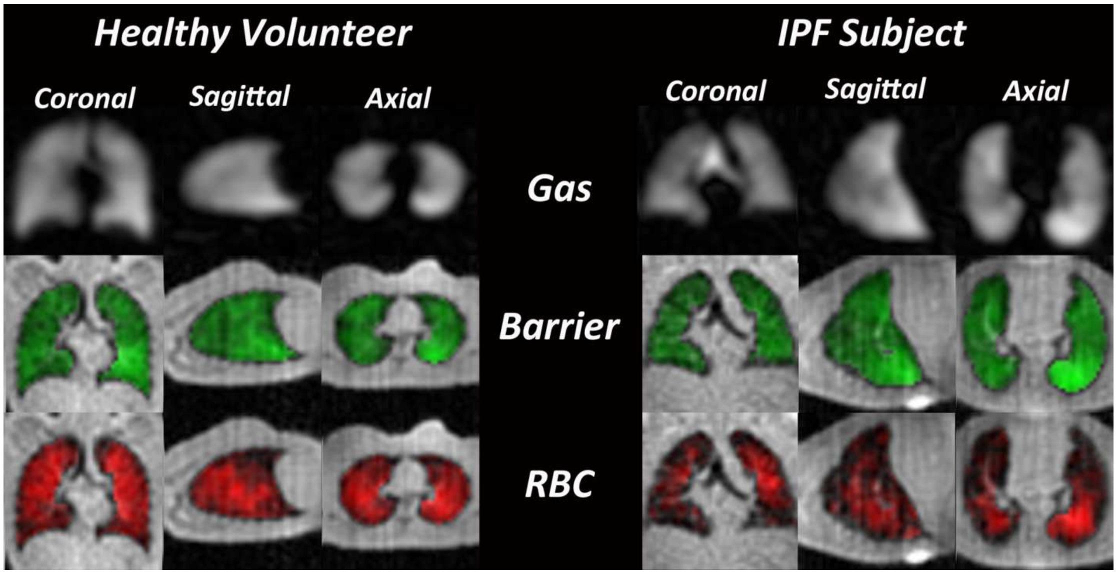

Figure 54: Representative single breath images of ^{129}Xe in the gas-phase (grayscale), barrier tissues (green), and red blood cells (RBC, red). The healthy volunteer showed a homogeneous distribution of ^{129}Xe in all three resonances. The IPF subject showed largely uniform gas-phase and barrier images, but exhibited widespread gas-transfer defects in the RBC image.

It is useful to compare the ^{129}Xe-RBC images, and their associated defect maps (yellow outline) to the representative CT images available in the IPF subjects (**Figure 55**). Qualitatively, regions of fibrosis and opacification visible on CT, while generally remaining ventilated, exhibit prominent ^{129}Xe-RBC gas-transfer defects. In these IPF subjects, gas transfer defects in both the posterior and anterior lung corresponded well to fibrosis seen on CT. Because ^{129}Xe-RBC transfer is strongest in the posterior lung, these defects are most striking. Gas transfer defects in the anterior lung, although also corresponding well to CT images, could also be a result of lower SNR. Also of note, are the ^{129}Xe-RBC transfer defects in regions where the CT scan appears normal.

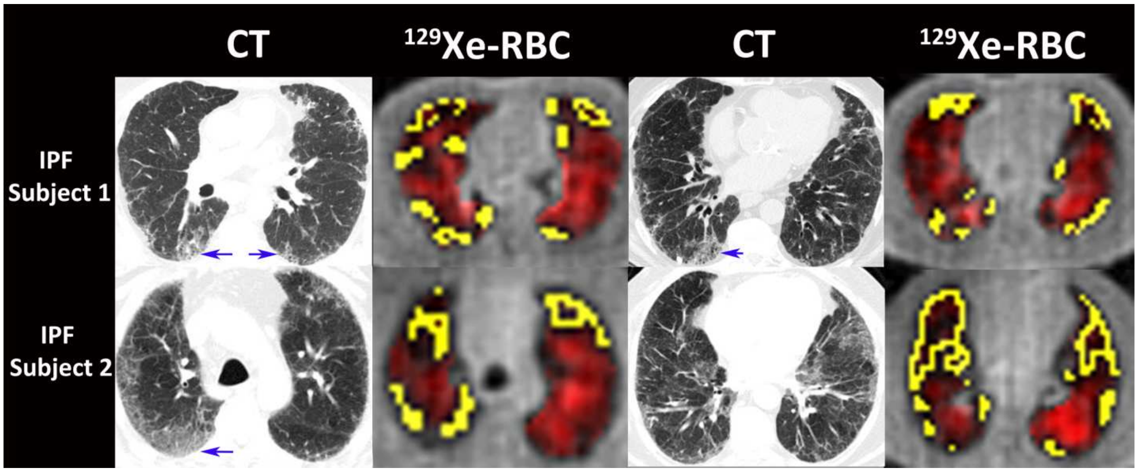

Figure 55: The ^{129}Xe-RBC images show numerous gas-transfer defects (yellow outline) that qualitatively correlate with regions of fibrosis seen on CT (blue arrows). Gas-transfer defects were also found in regions that had no visible fibrosis on CT. These could point to regions of subtle inflammation or early fibrosis that could still respond to therapy.

Additional quantitative insights can be gained by examining the various ratio maps—barrier:gas, RBC:gas, and RBC:barrier shown in **Figure 56**. In the healthy volunteer, both the barrier:gas and RBC:gas maps appear relatively homogeneous, whereas the RBC:barrier map seems to exhibit significantly increased ratios in the mid-lung gravitational plane. In the IPF subject, only the barrier:gas map remains moderately homogeneous. However, the RBC:gas map exhibits significantly reduced overall intensity compared to the healthy volunteer, as well as numerous gas transfer defects. The

RBC:barrier map is also quite striking in the IPF subject, and appears to exhibit just a few focal regions of high gas transfer, while RBC:barrier is low in most of the lung.

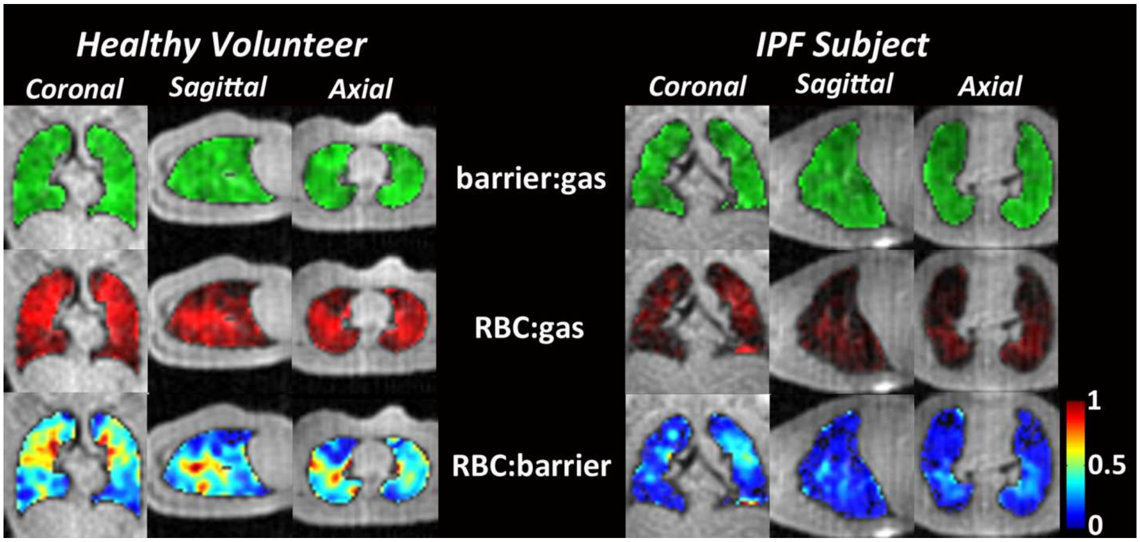

Figure 56: Ratios of the ^{129}Xe-barrier:gas, ^{129}Xe-RBC:gas, and the RBC:barrier images. Unlike the ^{129}Xe-RBC images seen in figure 3, compared to the healthy volunteer, the RBC:gas images, in addition to showing focal defects, has significantly lower signal intensity than the IPF subject. Similarly, the RBC:barrier maps in the IPF subject show dramatically reduced ^{129}Xe uptake by the RBCs.

7.4.6. Inferences about Dixon Imaging

This work demonstrates that it is feasible to produce isotropic 3D images of ^{129}Xe distribution in the airspaces and its transfer to the barrier and RBC compartments using a single-breath, 1-point Dixon technique. This acquisition offers a simple alternative to the IDEAL algorithm to create separate images of ^{129}Xe uptake in the RBC and barrier compartments, through its utilization of only a single echo-time. While this approach requires an additional scan to calibrate the TE_{90} in its current implementation, its advantage over the hierarchical IDEAL algorithm previously employed by Qing *et al.* is that it does not require two additional TEs, and their concomitantly smaller signals (49). A direct comparison of these two approaches in the same patient population should illuminate the relative benefits of each approach for routine clinical gas-exchange MRI.

The success of the 1-point Dixon approach lies in accurately calibrating the echo time required for a 90° RBC-barrier phase separation. It was interesting to note the variability of this TE_{90} relative to the calculated value and across groups. Such variability has been observed in prior studies of Dixon imaging including transgenic mice expressing human hemoglobin (144) and bleomycin-instilled rats (48). For healthy volunteers TE_{90} was almost 300 μs shorter (429 μs) than the theoretical predictions. Moreover, for IPF subjects, the calibrated TE_{90} was 194 μs shorter than for healthy volunteers, even though their RBC-barrier frequency difference was 40 Hz lower. Moreover, the RBC-barrier phase evolution varied linearly with TE, and the fit exhibited a negative intercept (-46.3°, healthy volunteers; -39.5° in IPF subjects). This suggests significant phase evolution occurred during the RF pulse, with the phase of the barrier compartment oddly leading the RBC. All this, along with lower TE_{90} in the IPF subjects may be in part explained by the different nature of susceptibility gradients and the variability in compartmental exchange in lungs affected by interstitial thickening and fibrosis. Ultimately, as discussed by Cleveland *et al*., these observations must be investigated by simulating the Bloch equations to better understand the phase accumulation during the RF pulse (48).

The 1-point Dixon acquisition has typically required additional reference scans to determine the receiver phase offset (phase error) and correct for the effects of field inhomogeneity (139). While, in principle, the receiver phase offset could be determined using the phases of the spectra from the calibration scan, we have found that significant phase receiver phase shifts can occur over time. On our scanner, we have seen receiver phase drift by as much as 100° in 10 minutes. Hence, we developed an approach that was immune to such drift by constraining the RBC:barrier ratio derived from imaging to match the spectroscopic ratio. This is somewhat similar to the 'virtual shimming' method introduced for the single-point Dixon based fat-water separation (145). In addition to determining the receiver phase offset, most multi-point Dixon methods (IDEAL, hierarchical IDEAL) correct for regional phase inhomogeneity by iteratively solving for a phase map (49,146). Here, ^{129}Xe Dixon MRI actually provides some unique advantages because the single-resonance gas-phase image acquired in the same breath can be used to provide a map of regional inhomogeneity. While Qing *et al*. also acquired the gas-phase image in the same breath, the phase image was used only as an initial estimate for the iterative decomposition algorithm (49). Their final field map showed less than 10 Hz difference from the initial estimate, which indicates that the initial phase map is representative of the regional inhomogeneity. Moreover, an additional advantage of the relatively low ^{129}Xe gyromagnetic ratio combined with imaging at 1.5 T and relatively short TE is that phase did not change by more than 90° across the lung and hence did not require phase unwrapping (139). Thus, other than requiring a calibration scan, the strategy proposed here uses the acquired data to correct the receiver phase offset and the regional field-inhomogeneity and provides images of all three ^{129}Xe compartments in the lung in a single breath.

As shown in **Figure 55**, separation of ^{129}Xe transfer to the RBCs depicted defects that qualitatively corresponded to regions of fibrosis seen on CT. Additionally, gas-transfer defects were also noted in regions where the CT appeared normal. These defects could indicate regions of subtle inflammation that cause diffusion limitation. It is conceivable that such regions represent earlier-stage disease that may potentially respond to therapy. Because ^{129}Xe transfer into the capillary bed follows Fick's first law, it depends on the alveolar surface-volume ratio and interstitial thickness, but additionally, ^{129}Xe transfer also depends on the local capillary blood volume (140). While the defects in the ^{129}Xe-RBC image are presumably caused by a thickened barrier in IPF, other conditions such as loss of alveolar surface area associated with chronic obstructive pulmonary disease (COPD), may equally impact the barrier image (49). Hence, RBC:barrier maps provide a potentially useful means to distinguish the two conditions. While our current hypothesis assumes that all signal voids in ^{129}Xe-RBC images are caused by limited diffusion of xenon across the thickened blood-gas barrier, this is difficult to distinguish from regional changes perfusion and thus, capillary blood volume. To this end, ^{129}Xe-RBC images acquired at multiple TRs may allow for regions that are purely diffusion-limited to show a moderate increase in signal at longer TRs. Alternatively, such discrimination could be done by also acquiring a high-resolution Gd-enhanced perfusion image (20).

7.5. Summary

The 1-point Dixon strategy was successfully used to create isotropic 3D images of ^{129}Xe in the airspaces, barrier, and the red blood cells within a single breath-hold. The method we propose is a simpler alternative to the hierarchical IDEAL algorithm (49), and has been shown to effectively depict focal gas transfer defects in IPF patients. While the current hypothesis assumes that the primary reason for reduced ^{129}Xe-RBC signal is diffusion limitation, future experiments will include an additional Gd-perfusion scan to quantify potential changes in regional capillary blood volume. Furthermore, the choice in RF pulse will play an important role in minimizing the off-resonant excitation of the gas-phase resonance, and mainly, minimize the RBC-barrier phase evolution during the RF pulse. Additionally, understanding the root cause of the phase evolution may negate the need to calibrate the TE_{90}, leading to a simpler single scan exam. Additionally, because the Dixon condition is satisfied only at the center of k-space, future studies will employ an iterative means to estimate the barrier and RBC images to correct for the continued phase accumulation during data acquisition (146). Given the good correlation between the ^{129}Xe-RBC and CT images, these preliminary results show that the ^{129}Xe-RBC images offer an ionizing-radiation-free, non-invasive means to visualize diffusive gas-exchange in the lung.

8. Future Directions

The work done over the last few years have shown that the unique resonances of hyperpolarized xenon in the airspaces, barrier tissue and the red blood cells (dissolved-phase) provide a world of information about lung structure and function. My thesis has followed xenon from the airspaces to the blood using diffusion-weighted imaging, single-breath gas and dissolved-phase imaging, and has culminated in creating distinct 3D images of all three resonances of ^{129}Xe in a single breath (**chapter 7**). The immediate future of dissolved-phase ^{129}Xe MRI lies in first obtaining a deeper understanding of the frequencies, widths and exchange processes between the different resonances of xenon. Furthermore, a greater focus should also be on improving the image quality through optimization of the pulse sequence and reconstruction. While an increase in ^{129}Xe polarization should help the cause, this boost in signal can be properly leveraged if the image quality improvements are achieved with a focus in the following areas –

a) ***Improvements to the RF frequency profile and the B_1 field***. The RF pulse shape and the associated B_1 field significantly impact the image quality. As discussed in **chapters 4 and 6**, the RF frequency profile is imperfect. This frequency profile can be warped significantly by the distortion introduced by the mixers in the exciter board, and additionally by the non-linearity of the RF amplifier. This distortion imparts different flip-angles to the RBC and barrier resonances. While this differential excitation of the RBC and barrier will not affect our results, these measurements may change if there are subtle frequency shifts, or when measured at different sites. To overcome this drawback, it is essential to look at alternate RF pulse shapes (Gaussian, Hyperbolic Secant) that may be less susceptible to the vagaries of the amplifier, and ensure uniform and selective excitation of the dissolved-phase. Alternatively, the RF pulses can be 'pre-warped' by determining the gain profile of the amplifier (97), which will ensure that clean RF pulses are delivered to the coil regardless of the distortion in transmit chain. In addition to the warped shape, the work done by He *et al*. has reiterated that the B_1 field generated by the vest coil is inhomogeneous (143). While this inhomogeneity can be corrected using a Bias field correction algorithm, this method uses the signal intensity distribution to determine the bias field, which may in fact reflect the underlying physiological gradients in ventilation and gas-exchange (**chapter 5**). While this Bias field correction may be a good first step, it is important to understand the independent contributions to the signal intensity distribution made by physiology, and inhomogeneous B_1 fields.

b) ***Optimized non-Cartesian reconstruction and noise mitigation***. The need to complete the acquisition of HP gas images within a 16-second breath hold has been satisfied by obtaining fewer samples of k-space. To this end, the radial sequence has been advantageous, as it is robust against this k-space under-sampling. However, the broader acceptance of the radial sequence requires overcoming several technical problems. *Firstly*, the rapid acquisition requires the fast switching of gradients which induces Eddy current artifacts, and additionally, it was recently noted that the ramping of gradients induces noise spikes in the FIDs by coupling switching noise from the gradient amplifiers into the large ^{129}Xe vest coil. The source of these noise spikes need to be investigated and their mitigation will significantly improve image quality. *Secondly*, as the number of k-space samples is progressively reduced below the Nyquist limit, subtle streaking artifacts are introduced in the image, and the robustness of the radial sequence to undersampling begins to fade. Recently, the concepts of compressed sensing (CS) have crossed over from information theory to aid in reconstructing MR data (147). CS takes advantage of the sparsity of the MR data, typically in the Wavelet domain, and provided the data is incoherently sampled, images can be reconstructed with significantly fewer samples than predicted by the Nyquist theorem. More recently, these concepts have been adopted by the HP community to create ventilation images, and were extended even further to simultaneously image ventilation and the thoracic cavity (148). As an extension to this approach, if the RBC and barrier images were considered to be images of the same region of interest, but of different contrast, CS reconstruction can also be extended using Bayesian methods to exploit this 'redundancy' of information and reconstruct images with lower error and higher quality (149). Further, as shown in (150), one can also exploit the high mutual information between the RBC and barrier to reconstruct images with significantly fewer samples. With optimized RF pulses, mitigated gradient noise, CS reconstruction, and improved polarization, the next few years should see a significant improvement in ^{129}Xe image quality.

While the utility of ^{129}Xe-RBC and ^{129}Xe-barrier images has initially been tested in subjects with idiopathic pulmonary fibrosis (IPF) and have shown to be sensitive to their characteristic diffusion-limitation, they can be applied to any pulmonary disease that may have impaired gas-exchange. This broader dissemination of ^{129}Xe MRI will help establish regional metrics that are sensitive to early changes in pulmonary function. Broadly, achieving this goal and establishing the sensitivity of ^{129}Xe MRI in longitudinal therapeutic studies would require that future work be focused in the following areas – **1)** *Obtaining information about capillary perfusion* **2)** *Understand the specificity of ^{129}Xe MRI by scanning multiple disease groups (COPD, Autoimmune conditions, Sickle cell disease, Pulmonary hypertension).*

8.1. The need for perfusion imaging

To first order, the origin and replenishment of the dissolved-phase xenon magnetization has been assumed to be primarily impacted by the diffusion of xenon across the pulmonary barrier. However, we have not rigorously tested the influence of capillary perfusion. As mentioned in **chapter 7**, future studies should acquire the ^{129}Xe-RBC image in conjunction with a perfusion image, to tease out the contributions of diffusion-limitation and the absence of regional perfusion. These perfusion images can be acquired using well established sequences that use an external bolus of a Gd-based contrast agent. Recently, Bauman *et al*. have obtained 3D isotropic dynamic contrast enhanced perfusion images high spatial and temporal resolution using a UTE sequence in conjunction with compressed sensing reconstruction (20). This method takes advantage of the T_1 shortening induced by the contrast agent to dynamically quantify the pulmonary blood flow, blood volume, and the mean transit time. With a perfusion image, we should be poised to study all the aspects of lung function – ventilation, perfusion, and diffusive gas-exchange.

In lieu of a perfusion image that uses an external contrast agent, the dissolved-phase of ^{129}Xe can also be used to probe regional perfusion. If the ^{129}Xe-RBC images are acquired at incrementally longer TRs, regions that are purely diffusion limited will have more time to replenish the RBC signal, and at longer TRs, should see an increase in their signal intensity. By contrast, regions that completely lack capillary perfusion, even at the longest TRs, will experience no increase in signal intensity. While Gd-based perfusion sequences probe the larger vasculature, this approach is sensitive to the presence of perfusion at the capillary level. This can be made feasible with subtle modifications to the existing pulse sequence to enable multi-TR acquisition, and with significant under-sampling (~10-fold) of k-space. As shown by Bauman *et al.*, the streaking artifacts that will be induced by the under-sampling of k-space can be overcome using compressed sensing reconstruction (20). In fact, there is a precedent for this in the hyperpolarized literature, as the SPARSE reconstruction algorithm has been used with HP helium, to reconstruct 3D ventilation images with an 8-fold fewer samples (151). With the availability of open source packages for compressed sensing reconstruction and working with Wavelet transforms, these approaches are within reach, and the dissolved-phase of xenon can be used to identify regions of diffusion limitation, and perfusion deficit.

8.2. Looking beyond IPF

As seen in **chapters 6 and 7**, the amplitude, frequency, and width of the dissolved-phase of ^{129}Xe has the sensitivity to pick up subtle changes in pulmonary function. However, it is important to look beyond IPF and study different disease groups to help identify the specificity of the current spectroscopy and imaging biomarkers. An immediate application can be seen in subjects with chronic obstructive pulmonary disease (COPD). As COPD hosts a range of disease phenotypes that impact the airways and the alveolar surface area (**chapter 3**), this disease group could benefit from every ^{129}Xe imaging method available. Ventilation and ADC imaging have been the mainstay in the

HP community to study and phenotype COPD (31,78). Ventilation imaging with HP ^{3}He has recently been extended to image the dynamic changes in ventilation during a breath hold (152). This has assisted in identifying collateral pathways of ventilation which are prevalent in COPD and with improvements in the polarization HP ^{129}Xe can also be used in the study of collateral ventilation. In addition to ventilation based advances, the RBC and barrier resonances can be used to study COPD. Unlike IPF, where the major impact was seen in the RBC images and the barrier images were largely unaffected, in subjects with emphysema, regions that have reduced surface area will have an increased ADC, which should correlate with reduced barrier and RBC signal intensity.

8.2.1. Autoimmune Diseases

Autoimmune diseases are initiated by genetic or environmental factors and target the reactivity of the immune system (153). While most of the diseases such as Type I diabetes or Graves' disease affect a particular organ system, some autoimmune diseases also affects the lung, such as Rheumatoid arthritis, which also causes the fibrosis of the interstitial tissue of the lungs (154). Recently, we had the opportunity to scan a subject who was diagnosed with an autoimmune condition – Dermatomyositis. This is an inflammatory disease of unknown origin that largely affects the striated muscles in the body, but may potentially give rise to interstitial lung disease (155). This subject had a clean CT scan, and a ventilation scan that rivaled that of a healthy volunteer (**figure 57A** below), but the gas-exchange as shown by the RBC:barrier ratio in **figure 57B**, was significantly diminished (0.15, 27% of normal). While this number is indicative of the inflammation associated with ILD, the barrier:gas in this subject was not elevated (0.007, 97% of normal). This warrants further investigation into the factors that impact the barrier:gas ratio. By scanning multiple subjects with autoimmune conditions longitudinally, xenon MRI has the potential to be an early predictor of the onset of ILD. Interestingly, it was also noticed that this subject was anemic, which may reduce the hematocrit. As it has been demonstrated that the widths of the barrier resonances are governed by the hematocrit (133), as a related project, future studies could use the width of the barrier resonance to non-invasively determine hematocrit and study their effect on the spectroscopic ratios.

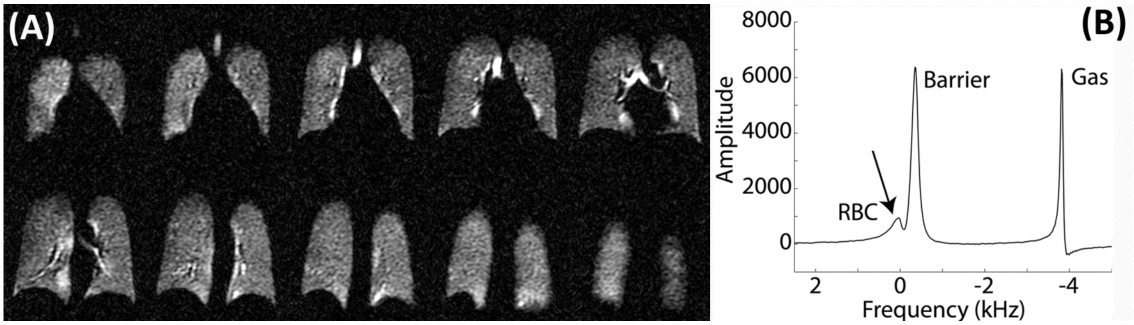

Figure 57: (A) Multi-slice GRE ventilation image from the subject with Dermatocyositis showing no ventilation defects. (B) Gas-transfer spectrum showing a significantly diminished (arrow) RBC signal.

8.2.2. Pulmonary vascular disease

Pulmonary vascular diseases are caused by the occlusions in the arterioles or venules of the pulmonary vasculature. Among these diseases, pulmonary arterial hypertension (PAH) is a rare yet deadly disease that roughly affects 15-50 people per million and is primarily characterized by a stark increase in the pulmonary artery pressure (156). This increase in pressure is brought on by the decrease in the cross sectional area of the pulmonary arteries. A change in this pressure is used to assess response to therapy, and is measured invasively, using a catheter inserted into the right heart. To make matters worse, there are no viable therapies that can cure PAH, and the current treatments are merely palliative (156). Much like IPF, the current clinical trials do not use strong end points to test treatment effectiveness. In addition to the arterial side, pulmonary vascular disease can also affect the venous side. Pulmonary veno-occlusive disease (PVOD) is a pathological disease that causes the pulmonary vein to be occluded by fibrotic tissue (157). It is a rare disorder of unknown origin, and affects only 0.1 or 0.2 per million people. While DL_{CO}, CT scans and ventilation-perfusion scans have been used to identify this disease, PVOD is often misdiagnosed as pulmonary hypertension, and the definitive diagnostic test is an invasive open lung biopsy (157). Given its sensitivity to subtle changes at the capillary level, ^{129}Xe MRI can offer a non-invasive alternative to diagnose and potentially differentiate PAH and PVOD.

Recently, we used ^{129}Xe gas-transfer spectroscopy and imaging to scan a subject who was suspected to have ILD. This subject worked at a tire plant for 30 years, and his symptoms included exercise induced shortness of breath and lowered oxygen saturation, a clean CT scan, and prior to the xenon scan, had no clear diagnosis. ^{129}Xe gas-transfer spectroscopy showed reduced gas-transfer and delayed oxygenation at the capillary level (**table 10)**. While the numbers shown were consistent with IPF, the ^{129}Xe gas-transfer spectra acquired at end exhalation resembled a healthy volunteer with all the spectroscopic metrics showing an increase at exhalation (**figure 58**). Thus, this subject had impaired gas-transfer, but normal lung compliance. Furthermore, the Dixon images acquired in this subject (**figure 59**) showed largely normal ventilation, and few regions of lowered barrier signal. The RBC signal was lower on the whole, and in poorly ventilated regions showed subtle gas-transfer defects. Based on these results, the subject was referred for a VATS lung biopsy. This reported multiple vascular lesions, and extensive vascular thickening, which led to the diagnosis of pulmonary arterial hypertension, with associated ILD. Dedicated studies of PAH using xenon may help identify biomarkers of the disease which may eliminate the need for an invasive biopsy.

We also had an opportunity to scan a subject with unexplained hypoxemia, and this subject had one of the lowest RBC:barrier ratios (0.07, 12.7% of normal), and as shown in **table 10**, the RBC:gas was 0.0013 (33% of normal) and the barrier:gas was significantly higher than normal at 0.019 (264% of normal). However, the most striking finding for this subject was the significantly lowered widths of the barrier and RBC resonances. Subsequently, this subject received a dual lung transplant, and a pathology report of the native lungs had features indicative of pulmonary veno-occlusive disease. These results warrant further study of pulmonary veno-occlusive disease and pulmonary hypertension using ^{129}Xe gas-transfer MRI.

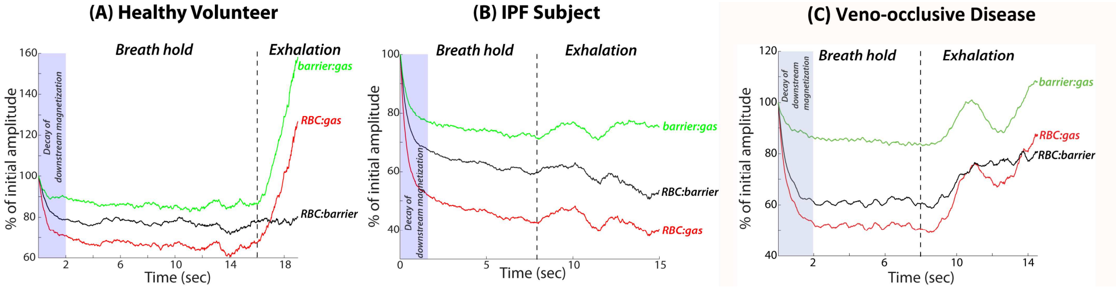

Figure 58: ^{129}Xe gas-transfer spectra acquired during a breath hold and at end exhalation, in a healthy volunteer (A) and an IPF subject (B). The barrier:gas and RBC:gas metrics in a healthy volunteer showed a massive increase during exhalation. These metrics in the IPF subject however, showed no increase upon exhalation. (C) Subject with PAH that shows increase in the RBC and barrier signal at exhalation, which would indicate normal lung compliance.

Table 10: Gas-transfer metrics for pulmonary vascular disease subjects

	Ratios			RBC Frequency (Hz)	Width (Hz)		Inference
	RBC:barrier	RBC:gas	barrier:gas		RBC	Barrier	
PAH	0.23	0.0023	0.01	-305.5	134.2	131.0	Ratios indicate reduced gas-transfer, and the lower RBC frequency suggests delayed capillary oxygenation. Lowered barrier width may indicate a reduced hematocrit.
PVOD	0.07	0.0013	0.019	-302.0	78.3	107.1	RBC:barrier is the lowest seen in our study. Lower RBC frequency points to delayed capillary oxygenation. Width of the RBC resonance is approximately a factor of 2 lower than that in healthy volunteers.

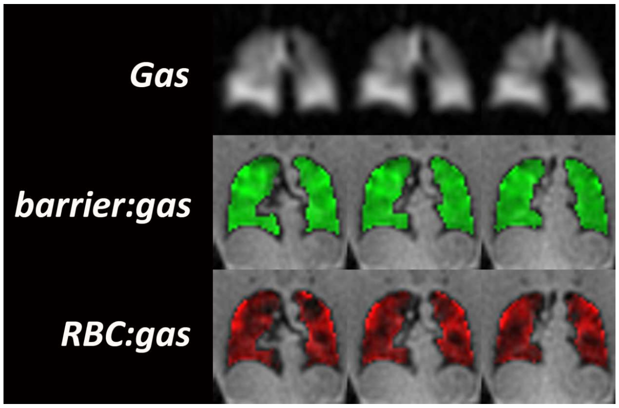

Figure 59: Dixon images acquired in a subject with pulmonary arterial hypertension. The barrier images show subtly reduced signal in the apices of the lung, potentially indicative of emphysema, and the RBC show spotty defects.

The thesis has shown the feasibility of using HP ^{129}Xe MRI to create images of pulmonary gas-exchange. In addition to diffusion-weighted imaging using the gas-phase of ^{129}Xe, the dissolved-phase of xenon fundamentally probes the diffusive gas-exchange in the lung. The examples shown in this thesis and more so in this chapter, suggest that xenon spectroscopy and imaging has the capability to be extended to study a plethora of pulmonary diseases. Bolstered by the imminent advances in polarization technology that will provide liter quantities of xenon with high polarization (40 – 50%), one can envision the use of an integrated MRI exam that can probe ventilation, alveolar microstructure using the gas-phase of ^{129}Xe, perfusion and tissue-density using ^{1}H UTE sequences, and most importantly, using the dissolved-phase of ^{129}Xe to image gas-exchange. This arsenal of imaging and spectroscopy tools can be further expanded to study the fundamental processes of the lung dynamically, and these tools and future advances will help provide a non-invasive and ionizing radiation free approach to furthering the care of patients with pulmonary disease.

Appendix

The Global Initiative for Chronic Obstructive Lung Disease (GOLD) was created in 1998 to help in the management and diagnosis of Chronic Obstructive Pulmonary Disease (COPD) (4). Based on their recommendations, COPD is stratified using spirometric indices (FEV_1/FVC and FEV_1) into four different stages. These are shown in the table below.

Table 11: GOLD classification of COPD

Classification	**Spirometric reference values**
Stage I: Mild	$FEV_1/FVC<0.7$ $FEV_1>80\%$ of predicted
Stage II: Moderate	$FEV_1/FVC<0.7$ $50\%\leq FEV_1<80\%$ of predicted
Stage III: Severe	$FEV_1<FVC<0.7$ $30\%\leq FEV_1<50\%$ of predicted
Stage IV: Very Severe	$FEV_1/FVC<0.7$ $FEV_1<30\%$ of predicted

References

1. Fauci AS, Touchette NA, Folkers GK. Emerging infectious diseases: a 10-year perspective from the National Institute of Allergy and Infectious Diseases. Emerg Infect Dis 2005;11(4):519-525.

2. Morbidity & Mortality: 2009 Chart Book on Cardiovascular, Lung and Blood Diseases: National Institute of Health; National Heart, Lung and Blood Institute; 2009.

3. Masoli M, Fabian D, Holt S, Beasley R, Program G. The global burden of asthma: executive summary of the GINA Dissemination Committee Report. Allergy 2004;59(5):469-478.

4. Rabe KF, Hurd S, Anzueto A, Barnes PJ, Buist SA, Calverley P, Fukuchi Y, Jenkins C, Rodriguez-Roisin R, van Weel C, Zielinski J. Global strategy for the diagnosis, management, and prevention of chronic obstructive pulmonary disease - GOLD executive summary. Am J Respir Crit Care Med 2007;176(6):532-555.

5. Murray CJL, Lopez AD. Alternative projections of mortality and disability by cause 1990-2020: Global burden of disease study. Lancet 1997;349(9064):1498-1504.

6. Cazzola M, MacNee W, Martinez FJ, Rabe KF, Franciosi LG, Barnes PJ, Brusasco V, Burge PS, Calverley PMA, Celli BR, Jones PW, Mahler DA, Make B, Miravitlles M, Page CP, Palange P, Parr D, Pistolesi M, Rennard SI, Molken M, Stockley R, Sullivan SD, Wedzicha JA, Wouters EF. Outcomes for COPD pharmacological trials: from lung function to biomarkers. Eur Resp J 2008;31(2):416-468.

7. Ashutosh K, Haldipur C, Boucher ML. Clinical and personality profiles and survival in patients with COPD. Chest 1997;111(1):95-98.

8. Park KJ, Bergin CJ, Clausen JL. Quantitation of emphysema with three-dimensional CT densitometry: Comparison with two-dimensional analysis, visual emphysema scores, and pulmonary function test results. Radiology 1999;211(2):541-547.

9. Thurlbeck WM, Muller NL. Emphysema - definition, imaging and quantification. Am J Roentgenol 1994;163(5):1017-1025.

10. Lee YK, Oh YM, Lee JH, Kim EK, Kim N, Seo JB, Do Lee S. Quantitative assessment of emphysema, air trapping, and airway thickening on computed tomography (vol 186, pg 277, 2008). Lung 2008;186(4):277-277.

11. Hansell DM, Kerr IH. The Role Of High-Resolution Computed-Tomography In The Diagnosis Of Interstitial Lung-Disease. Thorax 1991;46(2):77-84.

12. Smith-Bindman R, Lipson J, Marcus R, Kim KP, Mahesh M, Gould R, de Gonzalez AB, Miglioretti DL. Radiation Dose Associated With Common Computed Tomography Examinations and the Associated Lifetime Attributable Risk of Cancer. Archives of Internal Medicine 2009;169(22):2078-2086.

13. Hoffman EA, Tajik JK, Kugelmass SD. Matching Pulmonary Structure And Perfusion Via Combined Dynamic Multislice CT And Thin-Slice High-Resolution CT. Comput Med Imaging Graph 1995;19(1):101-112.

14. Thieme SF, Hoegl S, Nikolaou K, Fisahn J, Irlbeck M, Maxien D, Reiser MF, Becker CR, Johnson TR. Pulmonary ventilation and perfusion imaging with dual-energy CT. European radiology 2010;20(12):2882-2889.

15. Musch G, Layfield JDH, Harris RS, Melo MFV, Winkler T, Callahan RJ, Fischman AJ, Venegas JG. Topographical distribution of pulmonary perfusion and ventilation, assessed by PET in supine and prone humans. J Appl Physiol 2002;93(5):1841-1851.

16. Petersson J, Rohdin M, Sanchez-Crespo A, Nyren S, Jacobsson H, Larsson SA, Lindahl SGE, Linnarsson D, Neradilek B, Polissar NL, Glenny RW, Mure M. Posture primarily affects lung tissue distribution with minor effect on blood flow and ventilation. Respir Physiol Neuro 2007;156(3):293-303.

17. Rhodes CG, Hughes JMB. Pulmonary Studies Using Positron Emission Tomography. European Respiratory Journal 1995;8(6):1001-1017.

18. Johnson KM, Fain SB, Schiebler ML, Nagle S. Optimized 3D ultrashort echo time pulmonary MRI. Magnetic Resonance in Medicine 2013;70(5):1241-1250.

19. Sa RC, Cronin MV, Henderson AC, Holverda S, Theilmann RJ, Arai TJ, Dubowitz DJ, Hopkins SR, Buxton RB, Prisk GK. Vertical distribution of specific ventilation

in normal supine humans measured by oxygen-enhanced proton MRI. J Appl Physiol 2010;109(6):1950-1959.

20. Bauman G, Johnson KM, Bell LC, Velikina JV, Samsonov AA, Nagle SK, Fain SB. Three-dimensional pulmonary perfusion MRI with radial ultrashort echo time and spatial–temporal constrained reconstruction. Magn Reson Med 2014;doi: 10.1002/mrm.25158.

21. Hopkins SR, Wielputz MO, Kauczor HU. Imaging lung perfusion. J Appl Physiol 2012;113(2):328-339.

22. Hopkins SR, Henderson AC, Levin DL, Yamada K, Arai T, Buxton RB, Prisk GK. Vertical gradients in regional lung density and perfusion in the supine human lung: the Slinky effect. J Appl Physiol 2007;103(1):240-248.

23. Henderson AC, Prisk GK, Levin DL, Hopkins SR, Buxton RB. Characterizing pulmonary blood flow distribution measured using arterial spin labeling. Nmr in Biomedicine 2009;22(10):1025-1035.

24. van Beek EJR, Wild JM, Kauczor HU, Schreiber W, Mugler JP, de Lange EE. Functional MRI of the lung using hyperpolarized 3-helium gas. J Magn Reson Imaging 2004;20(4):540-554.

25. Mugler JP, Driehuys B, Brookeman JR, Cates GD, Berr SS, Bryant RG, Daniel TM, deLange EE, Downs JH, Erickson CJ, Happer W, Hinton DP, Kassel NF, Maier T, Phillips CD, Saam BT, Sauer KL, Wagshul ME. MR imaging and spectroscopy using hyperpolarized Xe-129 gas: Preliminary human results. Magn Reson Med 1997;37(6):809-815.

26. Salerno M, Altes TA, Brookeman JR, de Lange EE, Mugler JP. Dynamic spiral MRI of pulmonary gas flow using hyperpolarized 3He: Preliminary studies in healthy and diseased lungs. Magnetic Resonance in Medicine 2001;46(4):667-677.

27. Horn FC, Deppe MH, Marshall H, Parra-Robles J, Wild JM. Quantification of regional fractional ventilation in human subjects by measurement of hyperpolarized 3He washout with 2D and 3D MRI. Journal of Applied Physiology 2014;116(2):129-139.

28. Kadlecek S, Hamedani H, Xu Y, Emami K, Xin Y, Ishii M, Rizi R. Regional alveolar partial pressure of oxygen measurement with parallel accelerated hyperpolarized gas MRI. Academic Radiology 2013;20(10):1224-1233.

29. Salerno M, de Lange EE, Altes TA, Truwit JD, Brookeman JR, Mugler JP. Emphysema: Hyperpolarized helium 3 diffusion MR imaging of the lungs compared with spirometric indexes - Initial experience. Radiology 2002;222(1):252-260.

30. Yu JS, Law M, Kadlecek S, Emami K, Ishii M, Stephen M, Woodburn JM, Vahdat V, Rizi RR. Simultaneous measurement of pulmonary partial pressure of oxygen and apparent diffusion coefficient by hyperpolarized He-3 MRI. Magn Reson Med 2009;61(5):1015-1021.

31. Mathew L, Kirby M, Etemad-Rezai R, Wheatley A, McCormack DG, Parraga G. Hyperpolarized ^{3}He magnetic resonance imaging: Preliminary evaluation of phenotyping potential in chronic obstructive pulmonary disease. European Journal of Radiology 2011;79(1):140-146.

32. Wang C, Mugler JP, De Lange EE, Shim Y, Altes TA. Healthy nonsmokers exposed regularly to secondhand smoke have evidence of lung injury detected by hyperpolarized-3 diffusion MRI. 2010; Am J Respir Crit Care Med 181;2010:A5521

33. Evans A, McCormack D, Ouriadov A, Etemad-Rezai R, Santyr G, Parraga G. Anatomical distribution of He-3 apparent diffusion coefficients in severe chronic obstructive pulmonary disease. J Magn Reson Imaging 2007;26(6):1537-1547.

34. Fain SB, Altes TA, Panth SR, Evans MD, Waters B, Mugler JP, Korosec FR, Grist TM, Silverman M, Salerno M, Owers-Bradley J. Detection of age-dependent changes in healthy adult lungs with diffusion-weighted He-3 MRI. Acad Radiol 2005;12(11):1385-1393.

35. Shea DA, Morgan. The Helium-3 Shortage: Supply, Demand, and Options for Congress. CRS Report for Congress 2010.

36. Virgincar RS, Cleveland ZI, Kaushik SS, Freeman MS, Nouls J, Cofer G, Martinez-Jimenez S, He M, Kraft M, Wolber J, McAdams HP, Driehuys B. Quantitative Analysis Of Hyperpolarized ^{129}Xe Ventilation Imaging In Healthy Volunteers And Subjects With Chronic Obstructive Pulmonary Disease. NMR in Biomedicine 2012(26):424-435.

37. Kaushik SS, Cleveland ZI, Cofer GP, Metz G, Beaver D, Nouls J, Kraft M, Auffermann W, Wolber J, McAdams HP, Driehuys B. Diffusion-Weighted

Hyperpolarized Xe-129 MRI in Healthy Volunteers and Subjects With Chronic Obstructive Pulmonary Disease. Magn Reson Med 2011;65(4):1155-1165.

38. American Thoracic S, European Respiratory S. American Thoracic Society/European Respiratory Society international multidisciplinary consensus classification of the idiopathic interstitial pneumonias. American Journal of Respiratory and Critical Care Medicine 2002;165(2):277-304.

39. Crystal RG, Fulmer JD, Roberts WC, Moss ML, Line BR, Reynolds HY. Idiopathic Pulmonary Fibrosis - Clinical, Histologic, Radiographic, Physiologic, Scintigraphic, Cytologic, And Biochemical Aspects. Ann Intern Med 1976;85(6):769-788.

40. Raghu G, Collard HR, Egan JJ, Martinez FJ, Behr J, Brown KK, Colby TV, Cordier J-F, Flaherty KR, Lasky JA, Lynch DA, Ryu JH, Swigris JJ, Wells AU, Ancochea J, Bouros D, Carvalho C, Costabel U, Ebina M, Hansell DM, Johkoh T, Kim DS, King TE, Kondoh Y, Myers J, Müller NL, Nicholson AG, Richeldi L, Selman M, Dudden RF, Griss BS, Protzko SL, Schünemann HJ. An Official ATS/ERS/JRS/ALAT Statement: Idiopathic Pulmonary Fibrosis: Evidence-based Guidelines for Diagnosis and Management. American Journal of Respiratory and Critical Care Medicine 2011;183(6):788-824.

41. King TE, Bradford WZ, Castro-Bernardini S, Fagan EA, Glaspole I, Glassberg MK, Gorina E, Hopkins PM, Kardatzke D, Lancaster L, Lederer DJ, Nathan SD, Pereira CA, Sahn SA, Sussman R, Swigris JJ, Noble PW. A Phase 3 Trial of Pirfenidone in Patients with Idiopathic Pulmonary Fibrosis. New England Journal of Medicine 2014;370(22):2083-2092.

42. Antoniou KM, Margaritopoulos GA, Siafakas NM. Pharmacological treatment of idiopathic pulmonary fibrosis: from the past to the future. European Respiratory Review 2013;22(129):281-291.

43. Cleveland ZI, Cofer GP, Metz G, Beaver D, Nouls JC, Kaushik SS, Kraft M, Wolber J, Kelly KT, McAdams HP, Driehuys B. Hyperpolarized 129Xe MR Imaging of Alveolar Gas Uptake in Humans. PLoS ONE 2010;5(8):8.

44. Mugler JP, Altes TA, Ruset IC, Miller GW, Mata JF, Qing K, Tsentalovich I, Hersman FW, Ruppert K. Image-based measurement of T2* for dissolved-phase Xe129 in the human lung. Proceedings of the International Society for Magnetic Resonance in Medicine Melbourne, Australia 2012.

45. Dregely I, Ruset IC, Mata JF, Ketel J, Ketel S, Distelbrink J, Altes TA, Mugler JP, Miller GW, Hersman FW, Ruppert K. Multiple-Exchange-Time Xenon Polarization Transfer Contrast (MXTC) MRI: Initial Results in Animals and Healthy Volunteers. Magn Reson Med 2012;67(4):943-953.

46. Mugler JP, Altes TA, Ruset IC, Dregely IM, Mata JF, Miller GW, Ketel S, Ketel J, Hersman FW, Ruppert K. Simultaneous magnetic resonance imaging of ventilation distribution and gas uptake in the human lung using hyperpolarized xenon-129. Proc Natl Acad Sci U S A 2010;107(50):21707-21712.

47. Driehuys B, Cofer GP, Pollaro J, Mackel JB, Hedlund LW, Johnson GA. Imaging alveolar-capillary gas transfer using hyperpolarized Xe-129 MRI. Proc Natl Acad Sci U S A 2006;103(48):18278-18283.

48. Cleveland ZI, Virgincar RS, Qi Y, Robertson SH, Degan S, Driehuys B. 3D MRI of impaired hyperpolarized 129Xe uptake in a rat model of pulmonary fibrosis. NMR Biomed 2014;doi: 10.1002/nbm.3127.

49. Qing K, Ruppert K, Jiang Y, Mata JF, Miller GW, Shim YM, Wang C, Ruset IC, Hersman FW, Altes TA, Mugler JP. Regional mapping of gas uptake by blood and tissue in the human lung using hyperpolarized xenon-129 MRI. Journal of Magnetic Resonance Imaging 2014;39(2):346-359.

50. West JB. Respiratory physiology: the essentials: Lippincott Williams & Wilkins; 2012.

51. Fichele S, Woodhouse N, Swift AJ, Said Z, Paley MNJ, Kasuboski L, Mills GH, van Beek EJR, Wild JM. MRI of helium-3 gas in healthy lungs: Posture related variations of alveolar size. J Magn Reson Imaging 2004;20(2):331-335.

52. Prisk GK, Yamada K, Henderson AC, Arai TJ, Levin DL, Buxton RB, Hopkins SR. Pulmonary perfusion in the prone and supine postures in the normal human lung. J Appl Physiol 2007;103(3):883-894.

53. Jensen RL, Crapo RO. Diffusing capacity: how to get it right. Respiratory care 2003;48(8):777-782.

54. Wanger J, Irvin C. Comparability of pulmonary function results from 13 laboratories in a metropolitan area. Respiratory care 1991;36(12):1375-1382.

55. Goodson BM. Using injectable carriers of laser-polarized noble gases for enhancing NMR and MRI. Concepts Magn Resonance 1999;11(4):203-223.

56. Zhao L, Albert MS. Biomedical imaging using hyperpolarized noble gas MRI: Pulse sequence considerations. Nucl Instrum Methods Phys Res Sect A-Accel Spectrom Dect Assoc Equip 1998;402(2-3):454-460.

57. Jameson CJ, Jameson AK, Hwang JK. Nuclear-Spin Relaxation By Intermolecular Magnetic Dipole Coupling In The Gas-Phase - Xe-129 In Oxygen. J Chem Phys 1988;89(7):4074-4081.

58. Chen XJ, Moller HE, Chawla MS, Cofer GP, Driehuys B, Hedlund LW, Johnson GA. Spatially resolved measurements of hyperpolarized gas properties in the lung in vivo. Part I: Diffusion coefficient. Magn Reson Med 1999;42(4):721-728.

59. Zhao L, Mulkern R, Tseng CH, Williamson D, Patz S, Kraft R, Walsworth RL, Jolesz FA, Albert MS. Gradient-echo imaging considerations for hyperpolarized Xe-129 MR. J Magn Reson Ser B 1996;113(2):179-183.

60. Yablonskiy DA, Sukstanskii AL, Leawoods JC, Gierada DS, Bretthorst GL, Lefrak SS, Cooper JD, Conradi MS. Quantitative in vivo assessment of lung microstructure at the alveolar level with hyperpolarized He-3 diffusion MRI. Proc Natl Acad Sci U S A 2002;99(5):3111-3116.

61. Bernstein MA, King KF, Zhou XJ. Handbook of MRI Pulse Sequences: Elsevier; 2004.

62. Scheffler K, Hennig J. Reduced circular field-of-view imaging. Magn Reson Med 1998;40(3):474-480.

63. Wong STS, Roos MS. A Strategy For Sampling On A Sphere Applied To 3D Selective RF Pulse Design. Magn Reson Med 1994;32(6):778-784.

64. Glover GH, Pauly JM, Bradshaw KM. B-11 imaging with a 3-dimensional reconstruction method. J Magn Reson Imaging 1992;2(1):47-52.

65. Beatty PJ, Nishimura DG, Pauly JM. Rapid gridding reconstruction with a minimal oversampling ratio. IEEE Trans Med Imaging 2005;24(6):799-808.

66. Pipe JG, Menon P. Sampling density compensation in MRI: Rationale and an iterative numerical solution. Magn Reson Med 1999;41(1):179-186.

67. Crank J. The Mathematics of Diffusion. New York: Oxford University Press Inc.; 1975.

68. Norquay G, Leung G, Stewart NJ, Tozer GM, Wolber J, Wild JM. Relaxation and exchange dynamics of hyperpolarized 129Xe in human blood. Magn Reson Med 2014;doi: 10.1002/mrm.25417.

69. Dixon WT. Simple Proton Spectroscopic Imaging. Radiology 1984;153(1):189-194.

70. Yu HZ, Reeder SB, McKenzie CA, Brau ACS, Shimakawa A, Brittain JH, Pelc NJ. Single acquisition water-fat separation: Feasibility study for dynamic imaging. Magn Reson Med 2006;55(2):413-422.

71. Coombs BD, Szumowski J, Coshow W. Two-point dixon technique for water-fat signal decomposition with B-o inhomogeneity correction. Magn Reson Med 1997;38(6):884-889.

72. Celli BR, Macnee W. Standards for the diagnosis and treatment of patients with COPD: A summary of the ATS/ERS position paper. Eur Resp J 2004;23(1):932-946.

73. Makita H, Nasuhara Y, Nagai K, Ito Y, Hasegawa M, Betsuyaku T, Onodera Y, Hizawa N, Nishimura M. Characterisation of phenotypes based on severity of emphysema in chronic obstructive pulmonary disease. Thorax 2007;62(11):932-937.

74. Smith-Bindman R, Lipson J, Marcus R, Kim KP, Mahesh M, Gould R, de Gonzalez AB, Miglioretti DL. Radiation dose associated with common computed tomography examinations and the associated lifetime attributable risk of cancer. Arch Intern Med 2009;169(22):2078-2086.

75. Chen XJ, Hedlund LW, Moller HE, Chawla MS, Maronpot RR, Johnson GA. Detection of emphysema in rat lungs by using magnetic resonance measurements of He-3 diffusion. Proc Natl Acad Sci U S A 2000;97(21):11478-11481.

76. Fain SB, Panth SR, Evans MD, Wentland AL, Holmes JH, Korosec FR, O'Brien MJ, Fountaine H, Grist TM. Early emphysematous changes in asymptomatic smokers: Detection with He-3 MR imaging. Radiology 2006;239(3):875-883.

77. Stavngaard T, Sogaard LV, Batz M, Schreiber LM, Dirksen A. Progression of emphysema evaluated by MRI using hyperpolarized He-3 (Hp He-3)

measurements in patients with alpha-1-antitrypsin (A1AT) deficiency compared with CT and lung function tests. Acta Radiol 2009;50(9):1019-1026.

78. Kirby M, Mathew L, Wheatley A, Santyr GE, McCormack DG, Parraga G. Chronic Obstructive Pulmonary Disease: Longitudinal Hyperpolarized He-3 MR Imaging. Radiology 2010;256(1):280-289.

79. Yablonskiy DA, Sukstanskii AL, Woods JC, Gierada DS, Quirk JD, Hogg JC, Cooper JD, Conradi MS. Quantification of lung microstructure with hyperpolarized He-3 diffusion MRI. J Appl Physiol 2009;107(4):1258-1265.

80. Diaz S, Casselbrant I, Piitulainen E, Magnusson P, Peterson B, Wollmer P, Leander P, Ekberg O, Akeson P. Validity of apparent diffusion coefficient hyperpolarized He-3-MRI using MSCT and pulmonary function tests as references. Eur J Radiol 2009;71(2):257-263.

81. Patz S, Hersman FW, Muradian I, Hrovat MI, Ruset IC, Ketel S, Jacobson F, Topulos GP, Hatabu H, Butler JP. Hyperpolarized Xe-129 MRI: A viable functional lung imaging modality? Eur J Radiol 2007;64(3):335-344.

82. Mugler JP, Mata JF, Wang HTJ, Tobias WA, Cates GD, Christopher JM, Missel JL, Reish AG, Ruppert K, Brookeman JR, Hagspiel KD. The apparent diffusion coefficient of 129-Xe in the lung: Preliminary human results. Proceedings of the International Society for Magnetic Resonance in Medicine. Kyoto, Japan 2004. p 769.

83. Sindile A, Muradian I, Hrovat MI, Johnson DC, Hersman FW, Patz S. Human pulmonary diffusion weighted imaging at 0.2T with hyperpolarized 129Xe. Proceedings of the International Society for Magnetic Resonance in Medicine. Berlin, Germany 2007. p 1290.

84. Mata JF, Altes TA, Cai J, Ruppert K, Mitzner W, Hagspiel KD, Patel B, Salerno M, Brookeman JR, de Lange EE, Tobias WA, Wang HTJ, Cates GD, Mugler JP. Evaluation of emphysema severity and progression in a rabbit model: comparison of hyperpolarized He-3 and Xe-129 diffusion MRI with lung morphometry. J Appl Physiol 2007;102(3):1273-1280.

85. Gonzalez RC, Woods RE. Digital Image Processing: Pearson Education; 2004.

86. Trengove RD, Dunlop PJ. Diffusion-Coefficients and Thermal-Diffusion Factors for 5 Binary-Systems of Nitrogen and a Noble-Gas. Physica A 1982;115(3):339-352.

87. Stern EJ, Frank MS. CT of the lung in patients with pulmonary-emphysema - Diagnosis, quantification, and correlation with pathological and physiological findings. Am J Roentgenol 1994;162(4):791-798.

88. Tuder RM, Yoshida T, Fijalkowka I, Biswal S, Petrache I. Role of lung maintenance program in the heterogeneity of lung destruction in emphysema. Proc Am Thorac Soc 2006;3(8):673-679.

89. Ruset IC, Ketel S, Hersman FW. Optical pumping system design for large production of hyperpolarized Xe-129. Phys Rev Lett 2006;96(5):053002-053001 - 053002-053004.

90. Diaz S, Casselbrant I, Piitulainen E, Pettersson G, Magnusson P, Peterson B, Wollmer P, Leander P, Ekberg O, Akeson P. Hyperpolarized He-3 apparent diffusion coefficient MRI of the lung: Reproducibility and volume dependency in healthy volunteers and patients with emphysema. J Magn Reson Imaging 2008;27(4):763-770.

91. Kaneko K, Milicemi.J, Dolovich MB, Dawson A, Bates DV. Regional distribution of ventilation and perfusion as a function of body position. J Appl Physiol 1966;21(3):767-777.

92. Albert RK, Hubmayr RD. The prone position eliminates compression of the lungs by the heart. Am J Respir Crit Care Med 2000;161(5):1660-1665.

93. Amis TC, Jones HA, Hughes JMB. Effect of posture on inter-regional distribution of pulmonary ventilation in man. Respir Physiol 1984;56(2):145-167.

94. Halaweish AF, Thedens DR, Sieren JP, Hoffman EA, Van Beek EJR. Volume-controlled hyperpolarized ^{3}He ADC measurements accross multiple lung volumes in human subjects. 2010; Am. J. Respir. Crit. Care Med., May 2010; 181;.

95. Ruppert K, Brookeman JR, Hagspiel KD, Mugler JP. Probing lung physiology with xenon polarization transfer contrast (XTC). Magn Reson Med 2000;44(3):349-357.

96. Cleveland ZI, Cofer GP, Metz G, Beaver D, Nouls J, Kaushik SS, Kraft M, Wolber J, Kelly KT, McAdams HP, Driehuys B. Hyperpolarized Xe-129 MR imaging of alveolar gas uptake in humans. Plos One 2010;5(8).

97. Chan F, Pauly J, Macovski A. Effects of RF amplifier distortion on selective excitation and their correction by prewarping. Magn Reson Med 1992;23(2):224-238.

98. Cleveland ZI, Moller HE, Hedlund LW, Driehuys B. Continuously Infusing Hyperpolarized Xe-129 into Flowing Aqueous Solutions Using Hydrophobic Gas Exchange Membranes. J Phys Chem B 2009;113(37):12489-12499.

99. Song JY, Liu YH, Gewalt SL, Cofer G, Johnson GA, Liu QH. Least-square NUFFT methods applied to 2-D and 3-D radially encoded MR image reconstruction. IEEE Trans Biomed Eng 2009;56(4):1134-1142.

100. Jolliet P, Bulpa P, Chevrolet JC. Effects of the prone position on gas exchange and hemodynamics in severe acute respiratory distress syndrome. Crit Care Med 1998;26(12):1977-1985.

101. Studholme C, Hill DLG, Hawkes DJ. An overlap invariant entropy measure of 3D medical image alignment. Pattern Recognit 1999;32(1):71-86.

102. Verschakelen JA, Vanfraeyenhoven L, Laureys G, Demedts M, Baert AL. Differences in CT density between dependent and nondependent portions of the lung - Influence of lung-volume. Am J Roentgenol 1993;161(4):713-717.

103. Wellman TJ, Winkler T, Costa ELV, Musch G, Harris RS, Venegas JG, Melo MFV. Effect of regional lung inflation on ventilation heterogeneity at different length scales during mechanical ventilation of normal sheep lungs. J Appl Physiol 2012;113(6):947-957.

104. Hoffman EA. Effect of body orientation on regional lung expansion: A computed tomography approach. J Appl Physiol 1985;59(2):468-480.

105. Tawhai MH, Nash MP, Lin CL, Hoffman EA. Supine and prone differences in regional lung density and pleural pressure gradients in the human lung with constant shape. J Appl Physiol 2009;107(3):912-920.

106. Patz S, Muradyan I, Hrovat MI, Dabaghyan M, Washko GR, Hatabu H, Butler JP. Diffusion of hyperpolarized Xe-129 in the lung: a simplified model of Xe-129 septal uptake and experimental results. New J Phys 2011;13.

107. Johnson RL, Spicer WS, Bishop JM, Forster RE. Pulmonary Capillary Blood Volume, Flow And Diffusing Capacity During Exercise. J Appl Physiol 1960;15(5):893-902.

108. West JB, Dollery CT, Naimark A. Distribution of blood flow in isolated lung: relation to vascular and alveolar pressures. J Appl Physiol 1964;19(4):893-898.

109. West JB, Dollery CT. Distribution of blood flow and ventilation-perfusion ratio in the lung, measured with radioactive CO_2. J Appl Physiol 1960;15(3):405-410.

110. Glenny RW. Determinants of regional ventilation and blood flow in the lung. Intensive Care Med 2009;35(11):1833-1842.

111. Grassino AE, Forkert L, Anthonisen NR. Configuration of chest wall during increased gravitational stress in erect humans. Respir Physiol 1978;33(3):271-278.

112. Baryishay E, Hyatt RE, Rodarte JR. Effect of heart-weight on distribution of lung surface pressures in vertical dogs. J Appl Physiol 1986;61(2):712-718.

113. Wellman TJ, Winkler T, Costa ELV, Musch G, Harris RS, Venegas JG, Melo MFV. Effect of regional lung inflation on ventilation heterogeneity at different length scales during mechanical ventilation of normal sheep lungs. J Appl Physiol 2012;113(6):947-957.

114. Hoffman EA. Effect of body orientation on regional lung expansion: A computed tomography approach. J Appl Physiol 1985;59(2):468-480.

115. Weibel ER. What makes a good lung? The morphometric basis of lung function. Swiss Med Wkly 2009;139(27-28):375-386.

116. Crapo JD, Crapo RO. Comparison Of Total Lung Diffusion Capacity And The Membrane Component Of Diffusion Capacity As Determined By Physiologic And Morphometric Techniques. Respir Physiol 1983;51(2):183-194.

117. Hsia CCW. Recruitment of lung diffusing capacity - Update of concept and application. Chest 2002;122(5):1774-1783.

118. Driehuys B, Cofer GP, Pollaro J, Mackel JB, Hedlund LW, Johnson GA. Imaging alveolar-capillary gas transfer using hyperpolarized Xe-129 MRI. Proc Natl Acad Sci U S A 2006;103(48):18278-18283.

119. Kaushik SS, Freeman MS, Cleveland ZI, Davies J, Stiles J, Virgincar RS, Robertson SH, He M, Kelly KT, Foster WM, McAdams HP, Driehuys B. Probing the regional distribution of pulmonary gas exchange through single-breath gas- and dissolved-phase 129Xe MR imaging. Journal of Applied Physiology 2013;115(6):850-860.

120. Rafii R, Juarez MM, Albertson TE, Chan AL. A review of current and novel therapies for idiopathic pulmonary fibrosis. Journal of Thoracic Disease 2013;5(1):48-73.

121. Selman Ms, King JTE, Pardo A. Idiopathic Pulmonary Fibrosis: Prevailing and Evolving Hypotheses about Its Pathogenesis and Implications for Therapy. Ann Intern Med 2001;134(2):136-151.

122. Richeldi L, du Bois RM, Raghu G, Azuma A, Brown KK, Costabel U, Cottin V, Flaherty KR, Hansell DM, Inoue Y, Kim DS, Kolb M, Nicholson AG, Noble PW, Selman M, Taniguchi H, Brun M, Le Maulf F, Girard M, Stowasser S, Schlenker-Herceg R, Disse B, Collard HR. Efficacy and Safety of Nintedanib in Idiopathic Pulmonary Fibrosis. New England Journal of Medicine 2014;370(22):2071-2082.

123. Agustí AG, Roca J, Gea J, Wagner PD, Xaubet A, Rodriguez-Roisin R. Mechanisms of gas-exchange impairment in idiopathic pulmonary fibrosis. The American review of respiratory disease 1991;143(2):219-225.

124. Cotes JE, Chinn DJ, Miller MR. Lung function: physiology, measurement and application in medicine: John Wiley & Sons; 2009.

125. Keeler J. Understanding NMR spectroscopy: John Wiley & Sons; 2013.

126. Chang YV, Quirk JD, Ruset IC, Atkinson JJ, Hersman FW, Woods JC. Quantification of human lung structure and physiology using hyperpolarized 129Xe. Magnetic Resonance in Medicine 2014;71(1):339-344.

127. West JB. Diffusion. In: Coryell PA, editor. Respiratory Physiology - the essentials. 5 ed. Baltimore, MD: Williams & Wilkins; 1995.

128. Miller J, Johnson Jr R. Effect of lung inflation on pulmonary diffusing capacity at rest and exercise. Journal of Clinical Investigation 1966;45(4):493.

129. Smith TC, Rankin J. Pulmonary diffusing capacity and the capillary bed during Valsalva and Muller maneuvers. Journal of Applied Physiology 1969;27(6):826-833.

130. Fink C, Ley S, Risse F, Eichinger M, Zaporozhan J, Buhmann R, Puderbach M, Plathow C, Kauczor H-U. Effect of Inspiratory and Expiratory Breathhold on Pulmonary Perfusion: Assessment by Pulmonary Perfusion Magnetic Resonance Imaging. Investigative Radiology 2005;40(2):72-79.

131. Fuld MK, Halaweish AF, Haynes SE, Divekar AA, Guo J, Hoffman EA. Pulmonary Perfused Blood Volume with Dual-Energy CT as Surrogate for Pulmonary Perfusion Assessed with Dynamic Multidetector CT. Radiology 2013;267(3):747-756.

132. Wolber J, Cherubini A, Leach MO, Bifone A. Hyperpolarized 129Xe NMR as a probe for blood oxygenation. Magnetic Resonance in Medicine 2000;43(4):491-496.

133. Wolber J, Cherubini A, Santoro D, Payne GS, Leach MO, Bifone A. Linewidths of Hyperpolarized 129Xe NMR Spectra in Human Blood at 1.5T. Proceedings of the International Society for Magnetic Resonance in Medicine Volume 8. Denver, Colorado 2000. p 970.

134. Swanson SD, Rosen MS, Coulter KP, Welsh RC, Chupp TE. Distribution and dynamics of laser-polarized Xe-129 magnetization in vivo. Magnetic Resonance in Medicine 1999;42(6):1137-1145.

135. Leung G, Norquay G, Schulte RF, Wild JM. Radiofrequency pulse design for the selective excitation of dissolved 129Xe. Magnetic Resonance in Medicine 2014;doi: 10.1002/mrm.25089.

136. Weil JV, Jamieson G, Brown DW, Grover RF. The red cell mass-arterial oxygen relationship in normal man: Application to patients with chronic obstructive airway disease. The Journal of Clinical Investigation 1968;47(7):1627-1639.

137. Thompson B, Verbanck S, Schuermans D, Van Malderen S, Vincken W. The effect of conductive ventilation heterogeneity on. J Appl Physiol 2008;104:1094-1100.

138. Piiper J, Sikand R. Determination of D_{CO} by the single breath method in inhomogeneous lungs: Theory. Respiration Physiology 1966;1(1):75-87.

139. Ma JF. Dixon techniques for water and fat imaging. J Magn Reson Imaging 2008;28(3):543-558.

140. Kaushik SS, Freeman MS, Yoon SW, Liljeroth MG, Stiles JV, Roos JE, Foster WM, Rackley CR, McAdams HP, Driehuys B. Measuring Diffusion-Limitation with a Perfusion-Limited Gas-Hyperpolarized 129Xe Gas-Transfer Spectroscopy in Patients with Idiopathic Pulmonary Fibrosis. J Appl Physiol 2014;117:577-585.

141. Driehuys B, Cates GD, Miron E, Sauer K, Walter DK, Happer W. High-volume production of laser-polarized Xe-129. Appl Phys Lett 1996;69(12):1668-1670.

142. Chan RW, Ramsay EA, Cunningham CH, Plewes DB. Temporal stability of adaptive 3D radial MRI using multidimensional golden means. Magnetic Resonance in Medicine 2009;61(2):354-363.

143. He M, Kaushik SS, Robertson SH, Freeman MS, Virgincar RS, McAdams HP, Driehuys B. Extending Semiautomatic Ventilation Defect Analysis for Hyperpolarized 129Xe Ventilation MRI. Academic Radiology 2014;21(12):1530-1541.

144. Freeman MS, Cleveland ZI, Qi Y, Driehuys B. Enabling hyperpolarized 129Xe MR spectroscopy and imaging of pulmonary gas transfer to the red blood cells in transgenic mice expressing human hemoglobin. Magnetic Resonance in Medicine 2013;70(5):1192-1199.

145. Xiang Q-S. Improved Single Point Water-Fat Imaging with Virtual Shimming. Proceedings of the International Society of Magnetic Resonance in Medicine. Glasgow, Scotland 2001.

146. Brodsky EK, Holmes JH, Yu HZ, Reeder SB. Generalized k-space decomposition with chemical shift correction for non-cartesian water-fat Imaging. Magn Reson Med 2008;59(5):1151-1164.

147. Lustig M, Donoho D, Pauly JM. Sparse MRI: The application of compressed sensing for rapid MR imaging. Magnetic Resonance in Medicine 2007;58(6):1182-1195.

148. Qing K, Altes TA, Tustison NJ, Feng X, Chen X, Mata JF, Miller GW, de Lange EE, Tobias WA, Cates GD, Brookeman JR, Mugler JP. Rapid acquisition of helium-3 and proton three-dimensional image sets of the human lung in a single breath-hold using compressed sensing. Magnetic Resonance in Medicine 2014;doi: 10.1002/mrm.25499.

149. Bilgic B, Goyal VK, Adalsteinsson E. Multi-contrast reconstruction with Bayesian compressed sensing. Magn Reson Med 2011;66(6):1601-1615.

150. Wong E. Joint Reconstruction of Under-Sampled Multiple Contrast Images using Mutual Information. Proceedings of the International Society for Magnetic Resonance in Medicine. Melbourne, Australia 2012.

151. Ajraoui S, Lee KJ, Deppe MH, Parnell SR, Parra-Robles J, Wild JM. Compressed sensing in hyperpolarized 3He lung MRI. Magnetic Resonance in Medicine 2010;63(4):1059-1069.

152. Marshall H, Deppe MH, Parra-Robles J, Hillis S, Billings CG, Rajaram S, Swift A, Miller SR, Watson JH, Wolber J. Direct visualisation of collateral ventilation in COPD with hyperpolarised gas MRI. Thorax 2012:thoraxjnl-2011-200864.

153. Marrack P, Kappler J, Kotzin BL. Autoimmune disease: why and where it occurs. Nature medicine 2001;7(8):899-905.

154. McInnes IB, Schett G. The Pathogenesis of Rheumatoid Arthritis. New England Journal of Medicine 2011;365(23):2205-2219.

155. Fathi M, Dastmalchi M, Rasmussen E, Lundberg I, Tornling G. Interstitial lung disease, a common manifestation of newly diagnosed polymyositis and dermatomyositis. Annals of the rheumatic diseases 2004;63(3):297-301.

156. Sutendra G, Michelakis ED. Pulmonary arterial hypertension: challenges in translational research and a vision for change. Science translational medicine 2013;5(208):208sr205-208sr205.

157. Mandel J, Mark EJ, Hales CA. Pulmonary veno-occlusive disease. American Journal of Respiratory and Critical Care Medicine 2000;162(5):1964-1973.

Biography

S. Sivaram Kaushik (Shiv) was born on April 23, 1985 in Chennai, India, and grew up in Bangalore where his father S. Suryanarayanan owned an Advertising agency and his mother Lakshmi Suryanarayanan worked in an Insurance company. Shiv finished his high school education in 2003, from the prestigious National Public School Indiranagar, which is considered one of the best CBSE schools in the country. Soon after, he began his undergraduate education in B.M.S. College of Engineering in Bangalore, where he completed the requirements for a Bachelor of Engineering degree in Medical Electronics, and graduated First Class with Distinction. Subsequently, he received an Academic Merit Scholarship to pursue a Master's degree in Biomedical Engineering at Duke University. After completing his Master's degree in December of 2008, he worked for a year as a Research Associate for Bastiaan Driehuys at the Center for In Vivo Microscopy. Shiv soon began his Ph.D. in the Biomedical Engineering department at Duke University in 2010, where his research is focused on imaging pulmonary gas-exchange using hyperpolarized ^{129}Xe magnetic resonance imaging.